UiO : Department of Geosciences
University of Oslo

Seismic Wave Propagation Across Single Fractures

An Experimental and Numerical Study

Scott Adam Smith

Master's Thesis, Spring 2021

Abstract

Fluid flow through low permeability rocks is largely controlled by fractures. As a result, the remote detection and characterisation of fractures is critical for projects involving storage or extraction of fluids. A better understanding of how different fracture characteristics affect fracture specific stiffness and in turn, seismic wave propagation (velocity and attenuation), could aid the interpretation of fractures in seismic data. In this thesis, I investigate the effect of fracture aperture, angle, roughness and infill material on wave propagation by 1) interpreting ultrasonic data from isotropic compression tests conducted by Skurtveit et al. (2020) on core samples with and without fractures; and 2) running 2D numerical models, calibrated against the experimental results, in COMSOL Multiphysics. Additionally, I relate the ultrasonic data to flow test results from Skurtveit et al. (2020) to investigate how seismic measurements can be related to fracture permeability.

Experimental results show that P-waves propagating across thinner fractures with more contact points arrive faster, with larger amplitudes and higher central frequencies. Closure of fractures under increasing stress can be identified in the results by increasing P-wave velocity, whereas changes in first-arrival amplitude and frequency are ambiguous. The experimental results also highlight that increases in P-wave velocity can be related to decreases in fracture aperture and permeability. Modelling results show that 1) increasing fracture aperture leads to linear increases in arrival time delay and non-linear decreases in arrival amplitude, 2) increasing the roughness of fracture boundaries decreased arrival amplitudes by 10%, and 3) fracture infill material affects estimates of P-wave velocity and fracture specific stiffness depending upon the stiffness of the material. Furthermore, the distribution of mineral precipitates within the fracture, e.g. as linings or mineral bridges, is also shown to affect the arrival time, amplitude and frequency content of transmitted P-waves. Knowledge from this project could be applied to aid the remote characterisation of fractures and lead to safer and more efficient subsurface operations.

Acknowledgements

First, I would like to thank my supervisors Elin Skurtveit, Joonsang Park and Guillaume Sauvin at the Norwegian Geotechnical Institute for their guidance and support. I was very fortunate to have an multidisciplinary team of experienced supervisors.

This thesis was written as part of the COTEC (CO_2 containment and monitoring techniques) project led by Alvar Braathen at the Univeristy of Oslo. I have enjoyed being part of this group and I am looking forward to seeing future results of the project.

I am grateful for the financial support from the Department of Geosciences that was used for the academic license of COMSOL Multiphysics.

Finally, thank you Camilla.

Contents

List of Figures

List of Tables

CHAPTER 1

Introduction

1.1 Background and Motivation

Fractures have a large influence on fluid flow through low permeability rocks. Thus, the detection and characterisation of faults and fractures is critical for safe waste (e.g. CO_2) storage, geothermal energy, hydrocarbon extraction, and other projects involving the storage or extraction of fluids. Risks associated with leakage along faults can be minimised by identifying potential fluid migration pathways early on and monitoring the site during operation with time-lapse geophysical methods. To achieve this, it is necessary to not only detect fractures, but also to be able to able to relate their geophysical response to their mechanical and hydraulic parameters.

Fractured rock can be highly heterogeneous, with hydraulic conductivity values varying greatly over short distances (Hsieh, 2018). In order to accurately characterise flow through fractured rock, one must develop a model of the site that includes key faults and fractures that facilitate flow (NASEM, 2020, p.46). In situ measurements from boreholes provide valuable direct measurements but are also costly, spatially limited and may not be an option where vertical fluid migration is to be avoided (Laubach et al., 2019). Measurements of fractures in outcrops can give important structural and mineralogical information but are challenging to extrapolate to the subsurface (Bense et al., 2013). Geophysical methods can overcome this issue, providing spatially continuous information of the subsurface including imaging of faults and fractures that can be correlated with measurements from boreholes and outcrops (Day-Lewis et al., 2017). However, geophysical methods do not provide direct information on hydrogeological properties, and thus their effective use relies on a clear relationship between the geophysical and hydrogeological properties (Binley et al., 2015).

Pyrak-Nolte and Morris (2000) identified fracture specific stiffness as the critical parameter linking the seismic response of a fracture to its permeability (Fig. 1.1). The stiffness and permeability of fractures are dependent upon their geometry (e.g. aperture, contact area and roughness) and infilling material (e.g. air, water and dense minerals). Since fracture specific stiffness affects seismic velocities and attenuation, seismic measurements across fractures can in principle be related to fracture permeability (Fig. 1.1).

Though fluid flow through a site is typically dominated by few, large aperture

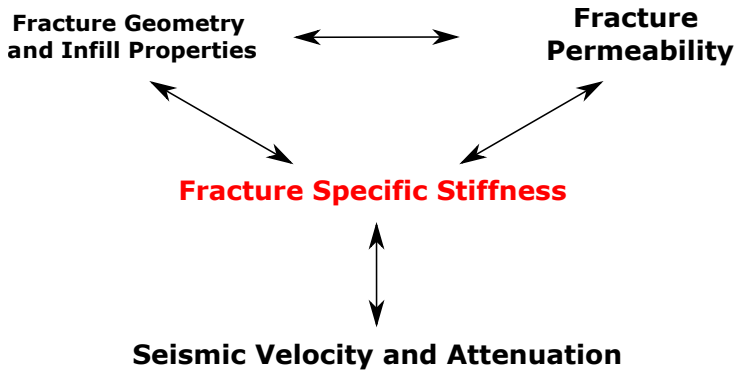

Figure 1.1: Schematic depicting the relationships between fracture geometry and infill properties, fracture permeability, specific stiffness and seismic velocity and attenuation. Fracture geometry includes parameters such as aperture, roughness and contact area. Figure redrawn from similar in Pyrak-Nolte and Morris (2000).

fractures (Gudmundsson, 2011, p.480), smaller fractures can not be disregarded completely. Small fractures are still important as they can contribute to fluid storage and may contribute significantly to fluid flow at greater depths as they are less compliant than large fractures (Pyrak-Nolte and Morris, 2000; Vinciguerra et al., 2005). Additionally, detailed investigations of fractures in core samples can provide information on fracture geometry and infill material, as well as how the fractures respond to stress, all of which are useful for fracture characterisation (NASEM, 2020, p.54). Furthermore, measurements of small scale fractures can contribute to understanding trends and provide a framework for upscaling results and interpreting field data (NRC, 1996, p.511).

While recent studies have improved our understanding of how fracture aperture is related to fracture specific stiffness and seismic measurements (Wu et al., 2014; Pan et al., 2017; Yang et al., 2019), the effect of other parameters such as roughness and infill material are still not well understood (Laubach et al., 2019; Yang et al., 2020; NASEM, 2020, p.55). In particular, these parameters can have large influences on fracture permeability (e.g. Gudmundsson, 2011, p.473). In this study, I will use experimental and numerical methods to investigate how different fracture characteristics, including roughness and infill material, affect seismic wave propagation across single fractures at the core sample scale.

1.2 Geological Setting and Core Samples

The experimental section of this study focuses on naturally fractured core samples from the CO2W55 exploration well, which was drilled into the footwall of the Little Grand Wash (LGW) Fault, Utah, USA (Kampman et al., 2013; Fig. 1.2). The LGW Fault and surrounding area host an active natural CO_2 leakage system in which CO_2 fluxes are observed at the surface at springs/geysers, travertine deposits and joint zones (Jung et al., 2014). Today, the most active source of CO_2 is Crystal Geyser, an abandoned drill hole from the 1930s which periodically erupts CO_2-rich cold water (Han et al., 2013; Fig. 1.2). Numerous recent studies have aimed to understand the geological and geophysical footprint of CO_2 transport along the fault (e.g. Shipton et al., 2004; Dockrill and Shipton, 2010; Ogata et al., 2014; Midtkandal et al., 2018; Oye et al., 2021). Knowledge from this natural leakage site can be applied to improve the risk assessment and monitoring of sites selected for CO_2 storage.

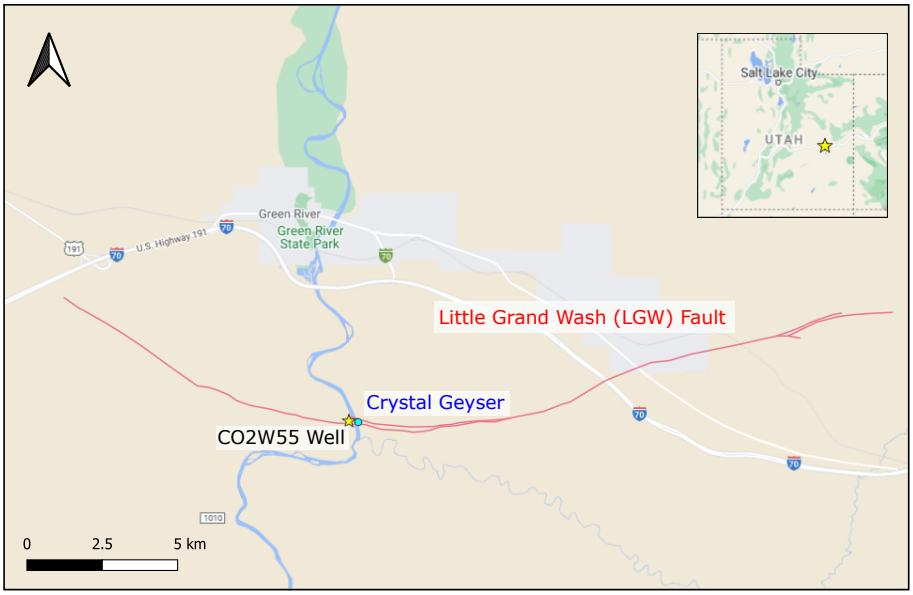

Figure 1.2: Map of the Little Grand Wash (LGW) Fault (red), CO2W55 Well (gold star), Crystal Geyser (cyan circle) and the surrounding area. Blue lines indicate rivers. Fault trace from Doelling (2001) and Doelling et al. (2015). Basemap from Google (2021).

The LGW Fault is a primarily dip-slip normal fault cutting through siltstones, shales and sandstones, with a 30 km long arcuate surface expression (Dockrill and Shipton, 2010; Fig. 1.2). The fault and associated fractures trend east to west and dip on average 70° to the south (Dockrill and Shipton, 2010). Paleo flow of CO_2-rich fluids along fractures is evidenced by travertine deposits, calcite cemented veins and bleaching (i.e. dissolution of iron oxides) of sandstone and siltstone layers close to the fracture walls (Shipton et al., 2004). These observations indicate near vertical fluid flow, including through stratigraphic units that would have traditionally been seen as sealing units (Ogata et al., 2014). This highlights the importance of detecting faults and fractures in reducing the

risk of waste storage projects, since they can act as vertical conduits for fluid migration. Ancient travertine deposits of different ages along the LGW Fault indicate that the pathway of CO_2 leakage has changed over time, possibly due to sealing of fractures by mineral precipitation (Jung et al., 2014).

Fractures in the study area show a wide variation of infill materials, most commonly CO_2-rich brine, calcite and gypsum, but also minor cements of pyrite, barite and ankerite as well as clay-rich gouge material in the fault zone (Eichhubl et al., 2009; Garden et al., 2001; Shipton et al., 2004; Skurtveit et al., 2017). Furthermore, some fractures are partially cemented and show varying distributions of infill material. While some fracture surfaces are lined with mineral precipitates, others include mineral 'bridges', in which cement fills the entire fracture aperture but is discontinuous along the fracture (Eichhubl et al., 2009; Frery et al., 2017).

The CO2W55 scientific exploration well was drilled in 2012 into the footwall of the Little Grand Wash Fault (Fig. 1.2) with the primary objective of recovering core samples of reservoir and sealing units exposed to CO_2 and CO_2-rich fluids (Kampman et al., 2013). During the drilling, CO_2 gas and CO_2-rich brine were first encountered in the basal 35 - 150 m of the Entrada Sandstone (Kampman et al., 2013). Kampman et al. (2013) comment that bleaching due to CO_2 was most intense around open fractures, indicating that these fractures facilitated flow of CO_2-rich fluid. Core samples were successfully retrieved between 10 and 282 m b.s. All fractures measured in the core samples were natural, sub-vertical tensile fractures with an average joint roughness coefficient (JRC) of 8 - 9 (Skurtveit et al., 2017). Unfortunately the fluid flow into the well was too high to conduct borehole logging and the well was cemented and abandoned (Kampman et al., 2013).

In this thesis, I will focus on two pairs of fractured and intact reference samples from the CO2W55 well (Skurtveit et al., 2020; Table 1.1). The core samples are cylindrical in shape and had pre-test diameters of approximately 25.5 mm and heights of approximately 52.1 mm (Fig. 1.3). Sample LGW1 is a red, silty sandstone with a thin vertical fracture (Fig. 1.3 - left). Sample LGW2 is the intact reference sample of LGW1. Sample LGW7 is a bleached, slightly coarser sandstone with a thicker vertical fracture showing substantial mineral precipitation including gypsum and pyrite (Fig. 1.3 - right). The reference sample of LGW7, LGW8, is also bleached.

Table 1.1: Overview of the core samples from well CO2W55 used in this study (Skurtveit et al., 2020).

Sample ID	Depth (m)	Sample description	Matrix Porosity (%)	Initial Density (kg/m^3)
LGW1	24.77	Thin vertical mode I fracture in red silty sandstone		2500
LGW2	24.71	Red reference sandstone	$5.8 - 6.0$	2500
LGW7	45.75	Thick vertical mode I fracture in bleached sandstone		2400
LGW8	45.81	Bleached reference sandstone	7.6 - 7.8	2450

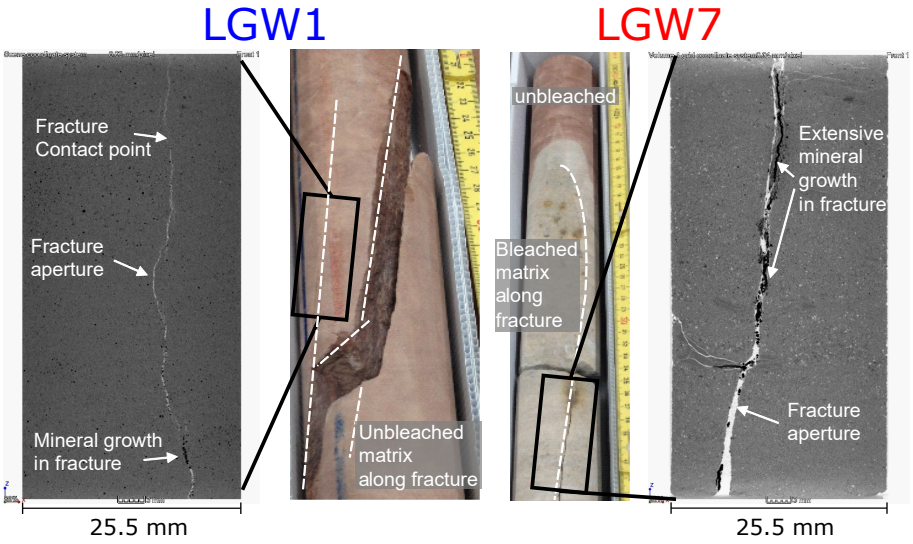

Figure 1.3: Photos and CT scans of the (left) thin fracture sample LGW1 and (right) thick fracture sample LGW7 used in this study. Figure reproduced from Skurtveit et al. (2017).

Previous Results from Skurtveit et al. (2020)

Flow and stiffness tests were conducted on the four samples at the Norwegian Geotechnical Institute (NGI), from 2016 to 2017. The relationship between static fracture stiffness and flow has been investigated (Figs. 1.4 and 1.5; Skurtveit et al., 2020). The thin fracture sample LGW1 shows a higher stiffness and lower permeability due to its smaller aperture and higher contact ratio (Table 1.2). The thick fracture sample LGW7 shows a lower stiffness and higher permeability due to its larger aperture and lower contact ratio (Table 1.2). The fractured samples show effective permeabilities 3 - 5 orders of magnitude higher than the intact reference samples, indicating that fluid flow is primarily through the fractures (Fig. 1.5). Variations in permeability with isotropic stress indicate fracture closure between 1 and 5 MPa for LGW7 and 1 and 3 MPa for LGW1 (Fig. 1.5).

The ultrasonic data used in the experimental section of this study was collected during these tests, but were not included in the interpretation published by Skurtveit et al. (2020).

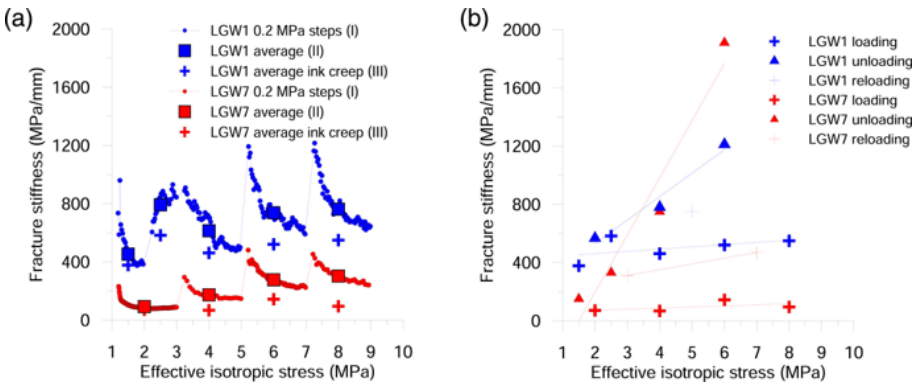

Figure 1.4: (a) Static fracture stiffness as a function of effective isotropic stress condition calculated using three different approaches, (I) 0.2 MPa pressure steps, (II) average for loading interval, and (III) average including creep deformation. (b) Static fracture stiffness including creep deformation for loading, unloading, and reloading. Figure reproduced from Skurtveit et al. (2020).

Table 1.2: Fracture characteristics estimated from CT volume reconstruction before and after the tests (Skurtveit et al., 2020). CT scans were taken under no confining pressure.

Sample ID	Mean mech. aperture (mm)	Contact area (%)	Roughness	Dense mineral ratio/all sample (%)
LGW1 pre-test	0.10	36	Smooth	20
LGW1 post-test	0.09	59	Smooth	23
LGW7 pre-test	0.53	14	Rough	99
LGW7 post-test	0.44	44	Rough	98

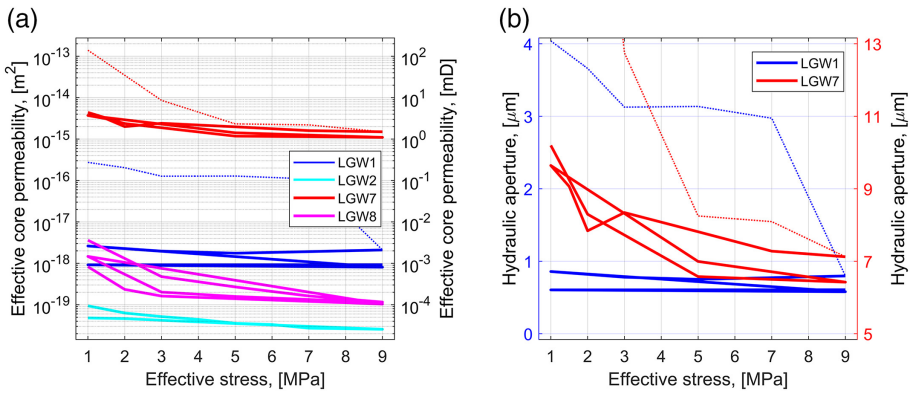

Figure 1.5: (a) Effective core sample permeability and (b) Hydraulic aperture calculated assuming zero contact ratio under increasing stress. The maximum value for LGW1 in the first loading cycle (above y-axis limit) is 32.3 μm. Dotted thin lines highlight data from the first loading cycle. Figure reproduced from Skurtveit et al. (2020).

1.3 Aims and Objectives

The overall aim of this thesis is to contribute to a better understanding of how the geometry (aperture, roughness, contact area) and infill material of single fractures affects seismic measurements (velocity and attenuation). Additionally, I will discuss to what extent changes in the ultrasonic data collected during the compression tests can be related to fracture closure and sample permeability determined by the flow tests (Fig. 1.5).

Originally, the aim of this thesis was to relate the laboratory measurements to field measurements with a focus on scaling of results and integration of other datasets. Unfortunately, this was not possible due to COVID-19, and so it was decided instead to support the experimental section with a numerical investigation into fracture characteristics and wave propagation.

Throughout the project, my objectives are to:

- Determine the effect of fractures on seismic velocity and attenuation by interpreting existing ultrasonic data from isotropic compression tests on samples with and without fractures.
- Interpret closure of the fractures under increasing stress from the ultrasonic data and investigate if these results can be related to results of the flow tests.
- Run numerical models calibrated against the experimental results to investigate the effect of fracture aperture, roughness, angle and infill material on estimates of fracture stiffness from seismic wave propagation.

CHAPTER 2

Theoretical Background

2.1 Fracture Characteristics

Fractures are mechanical discontinuities that separate a rock mass into two or more parts. They are quasi-planar, and typically have lower tensile and shear strengths than the surrounding rock matrix (Pyrak-Nolte, 2019). There are many different parameters that can be used to characterize fractures (e.g. Hakami, 1995; NASEM, 2020 p.20-25). In this study, I focus on the parameters of aperture, roughness, infill material, infill material distribution and contact area (Fig 2.1).

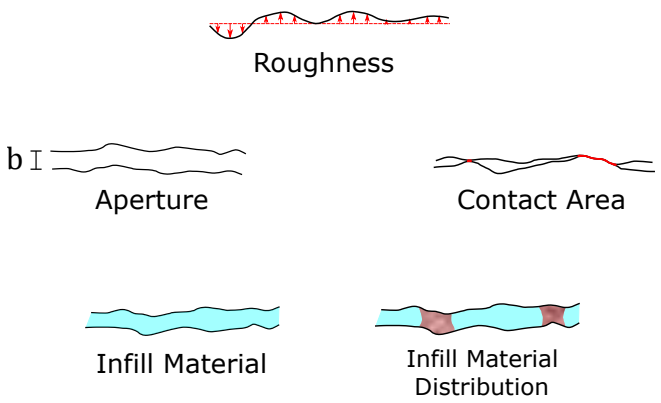

Figure 2.1: Schematic depicting key fracture parameters considered in this study.

Fracture **aperture** can be defined as the **mechanical aperture** or **hydraulic aperture**. The mechanical aperture is the width between the two fracture surfaces and accounts for the void volume. The hydraulic aperture is the interconnected aperture that contributes to the permeability of the fracture (See also section 2.4). This is an important distinction to make, since fracture surfaces are never perfectly smooth and so the hydraulic aperture is always smaller than the mechanical aperture. For example, the hydraulic aperture estimates of the fractures in samples LGW1 and LGW7 are one to two orders

of magnitude smaller than the average mechanical apertures (Table 1.2 and Fig. 1.5; Skurtveit et al., 2020).

Roughness is a measure of how rough or irregular a fracture surface is. It is a complex parameter that can be described using simple or complicated techniques (Thomas, 1998). Generally, roughness reflects how frequently and by how much the height of asperities deviate from a "centre line". The centre line runs parallel to the profile and intersects it such that the sums of the areas between the centre line and the profile either side of the line are equal (Tse and Cruden, 1979). One way to measure the average deviation is the root mean square (RMS), defined as:

$$RMS = \left[\frac{1}{M} \int_{x=0}^{x=M} y^2 dx \right]^{1/2} \tag{2.1}$$

where M is the number of discrete measurements of the fracture height, y is the absolute height of the fracture profile measured from the centre line and dx is the incremental distance between adjacent height readings.

Using the RMS as a starting point, Myers (1962) suggested three other parameters to quantitatively characterise roughness. One of these is Z_2, the RMS of the first spatial derivative of the profile, given by the equation:

$$Z_2 = \frac{1}{L} \int_{x=0}^{x=L} \left(\frac{dy}{dx} \right)^2 \tag{2.2}$$

where

$$xi = \text{ the ith segment of } L$$
$$L = \Sigma(xi) \text{ positive} + \Sigma(xi) \text{ negative}$$

In practice, a common approach to quantify roughness is to use the concept of the joint roughness coefficient (JRC), defined by Barton and Choubey (1977). Barton and Choubey (1977) determined the JRC empirically from shear tests conducted on naturally fractured samples and published a set of 10 typical roughness profiles with JRC values of 0 to 20. JRC is particularly useful since it can be estimated through simple mechanical tests and fractures can be visually compared with the reported roughness profiles.

Through analysis of the 10 standard profiles published by Barton and Choubey (1977), Tse and Cruden (1979) discovered that there is a strong correlation between the JRC and Z_2 values. For a given Z_2 value, JRC can be estimated within 1% uncertainty by:

$$JRC = 32.2 + 32.47 \log Z_2 \tag{2.3}$$

Contact area ratio is the ratio of the area of contacts between the fracture faces and the total surface area. Contact area ratio is highly stress dependent and fractures with higher contact area ratios are typically stiffer (Brown and

Scholz, 1985; Cook, 1992). The distribution of contact points along a fracture also influences its stiffness, with smaller contact points dispersed along a fracture forming stiffer interfaces than large or clustered contact points (Hopkins et al., 1987).

Infill material, the material between the fracture surfaces, is an important characteristic that affects the mechanical, hydraulic and geophysical properties of fractures. Fractures can be filled with material broken off from the fracture walls by mechanical erosion (gouge), or by cements formed by mineralisation as minerals precipitate out of a fluid flowing along the fracture (e.g. Laubach et al., 2019). Fractures may be completely filled to form veins, or partially filled to create areas with mineral bridges and open channels (e.g. NRC, 1996, p.84-86; Gudmundsson, 2011, p.332). For the purpose of this study, gases and fluids are also considered as infill materials.

2.2 Fracture Specific Stiffness

Fracture specific stiffness is a property that describes the resistance of a fracture to close and deform under increasing stress. It is the inverse of fracture compliance and is defined mathematically as the ratio of the incremental stress change $\Delta\sigma$ to the incremental change in fracture aperture Δb:

$$K = \frac{\Delta\sigma}{\Delta b} \tag{2.4}$$

Fracture specific stiffness can be estimated using **static** or **dynamic** methods. Static fracture specific stiffness, K_{static}, is determined experimentally from compression tests and equation 2.4 (e.g. Fig. 1.4; Skurtveit et al., 2020). Dynamic fracture specific stiffness, $K_{dynamic}$, is determined from seismic wave measurements taken across the fracture, by:

$$K_{dynamic} = \frac{\omega Z}{2\sqrt{\frac{1}{T^2} - 1}}, \tag{2.5}$$

where ω is the wave angular frequency, Z is the seismic impedance of the rock matrix and T is the transmission coefficient (Pyrak-Nolte et al., 1990). The transmission coefficient, T, for a given frequency can be estimated from the ratio of the Fourier spectrum of the signal from a fractured sample to the Fourier spectrum of the signal from the intact reference sample (Pyrak-Nolte, 2019; See also equation 2.11.

Furthermore, fractures have a fracture **normal** stiffness, K_N, and a fracture **tangential** stiffness, K_T, which reflect the resistance of a fracture to close under normal and tangential stresses, respectively (Fig. 2.2; Schoenberg, 1980). The normal and tangential specific stiffnesses of a fracture can be different and the ratio of K_N/K_T depends upon fracture geometry and infill material (e.g. Sayers et al., 2009; Choi et al., 2014; Loriaux et al., 2021). In this thesis the focus is on the normal stiffness, but it is important to be aware of the tangential stiffness since seismic measurements taken at oblique angles, such as in the laboratory experiments, depend upon both K_N and K_T.

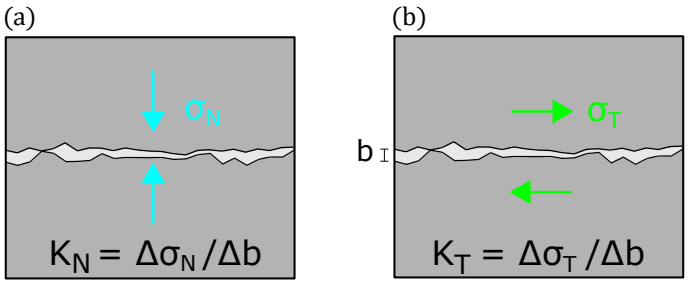

Figure 2.2: Fractures have a specific stiffness value for stresses in the a) normal and b) tangential directions. Estimates of fracture specific stiffness from wave propagation at non normal angles depends on both K_N and K_T. The ratio K_N/K_T may not be equal to 1.

For an open, fluid-filled fracture with no contact points, the normal specific stiffness is related to the fracture aperture, b, and bulk compressibility of the fluid, k_{fluid}, by (Wu et al., 2005):

$$K_N = \frac{k_{fluid}}{b} \tag{2.6}$$

Fracture specific stiffness is a useful parameter since it gives a quantitative characterisation of the fracture, without needing to perform a detailed analysis of the aperture, contact area ratio and roughness (Goodman et al., 1968). Estimates of stiffness from seismic measurements, $K_{dynamic}$, are typically larger than estimates from compression tests, K_{static} (Pyrak-Nolte, 2019; Zhou et al., 2020; Kewel, 2020).

Estimates of fracture specific stiffness depend upon the state of the fracture, which varies with changes in local stress conditions or fluid pressure. For example, increasing the normal stress on a fracture reduces the aperture and increases the contact area ratio, which in turn increases the fracture stiffness. Fracture stiffness increases non-linearly with increasing normal stress as more asperities come into contact and resist closure (Brown and Scholz, 1985). Conversely, an increase in fluid pressure within the fracture could increase the aperture and reduce the contact area ratio, increasing the compliance of the fracture.

Note that in this thesis, for the sake of being concise the term "Dynamic Normal Fracture Specific Stiffness", describing the estimate of fracture specific stiffness from seismic wave propagation normal to the fracture, may be shortened. Where wave propagation is non normal, or if referring to static estimates from Skurtveit et al. (2020), the appropriate terms will be explicitly mentioned to avoid confusion.

2.3 Seismic Wave Propagation across Single Fractures

Velocity and Attenuation

Seismic wave propagation through a material can be characterised by two properties: velocity and attenuation. Here I review theory most relevant to P-waves propagating across fractures. For a general introduction to seismic waves the reader is referred to textbooks such as Stein and Wysession (2009) and Shearer (2019).

The simplest method to estimate P- or S-wave **velocity** is to use the pulse-transmission (a.k.a. time-of-flight) method (e.g Birch, 1960). In this method, the time taken for a wave to travel across a known distance is recorded, and velocity is estimated using:

$$\text{velocity} = \frac{\text{source-receiver distance}}{\text{travel time}} \tag{2.7}$$

The velocity at which seismic waves travel through a material depend upon that material's elastic constants (λ, μ) and density (ρ). In short, P- and S-waves travel faster through stiffer rocks. Since fractures typically have lower stiffnesses than the surrounding rock matrix, they reduce seismic velocities. Though, where fractures are filled with minerals that are denser and stiffer than the rock matrix, they can cause higher seismic velocities (e.g. Rempe et al., 2018).

Attenuation describes the energy lost by a seismic wave as it propagates. Attenuation can be seen in arriving waves as reduced amplitudes and or a change in the frequency content, for example a reduction of high frequency content. There are four main causes of attenuation: 1) geometrical spreading of the wavefront; 2) energy loss due to internal friction, known as intrinsic attenuation; 3) scattering of the wavefront by small-scale heterogeneities and; 4) reflection and transmission of waves at discontinuities, such as fractures (Shearer, 2019, p.160). In this study, the focus is on the reflection and transmission of the waves at the fractures.

Modelling of Fractures

The three simplest ways to model the effect of fractures on seismic velocity and attenuation are shown in Fig. 2.3 (Pyrak-Nolte et al., 2017). The first approach is to model the rock matrix as an effective medium with lower average elastic moduli as a result of the fracture(s) (Fig. 2.3b; e.g. Liu et al., 2000). This approach may be satisfactory where fractures are much smaller than the source signal wavelength. However, effective medium hydrogeological models of fractured aquifers generally perform poorly as they fail to capture the large variability in hydraulic parameters (Neuman, 2005). Alternatively, the second and third approaches consider the discrete effect of fractures on seismic waves and can be used to create discrete fracture models. The second approach is to represent the fracture as a thin layer with an aperture b and lower elastic moduli than the rock matrix (Fig. 2.3b; e.g. Li et al., 2013; Lissa et al., 2019). This is known as a Thin Layer Interface Model (TLIM). The third approach is to represent the fracture as a displacement discontinuity with a fracture

specific stiffness K (Fig. 2.3b; e.g. Schoenberg, 1980; Pyrak-Nolte et al., 1990; De Basabe et al., 2016). A displacement discontinuity is also known as a non-welded contact or linear slip interface.

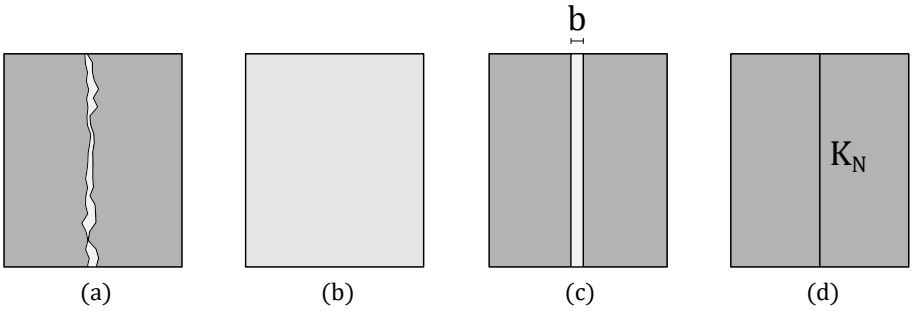

Figure 2.3: (a) Complex fracture geometry. The fracture can be represented as (b) an effective medium with reduced elastic moduli, (c) a thin-layer interface model in which the thin layer has reduced elastic moduli, or (d) a displacement discontinuity. Lighter colours represent lower elastic moduli. Figure redrawn from Pyrak-Nolte et al. (2017).

The key difference between the TLIM and displacement discontinuity model is how displacements are treated across the fracture (Fig. 2.4). In the displacement discontinuity model, fractures can be represented as 2D edges with zero width that cause discrete changes in displacements. In the TLIM, fractures are represented as domains with two edges across which displacements are continuous. The displacement discontinuity model is more efficient for numerical simulations since no mesh refinement is needed around the fractures (De Basabe et al., 2016; Wu et al., 2005). However, since the fracture geometrical parameters and infill properties are reduced to a single parameter (fracture specific stiffness), they cannot be varied directly. To investigate how fracture geometrical parameters and infill properties affect wave propagation, one must use the TLIM (e.g. Lissa et al., 2019).

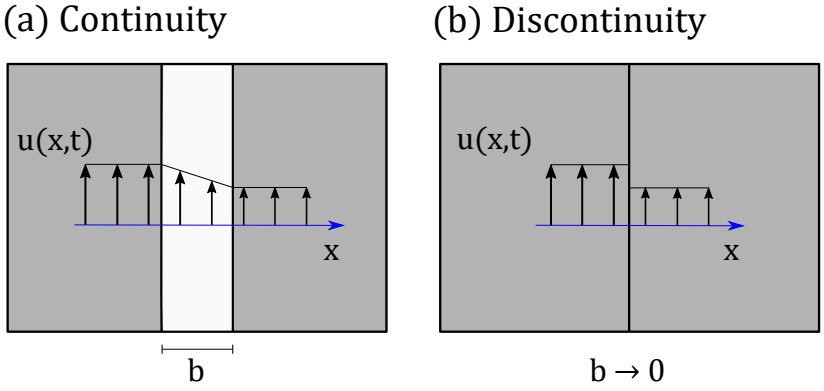

Figure 2.4: Schematic view of displacements across two sides of a fracture due to an incident P-wave for a a) continuity and b) discontinuity model. Figure redrawn from Li et al. (2013).

Reflection and Transmission

As a wave propagates across a fracture, energy is divided between the transmitted and reflected waves (Fig. 2.5). Reflection and transmission coefficients quantify the amplitude ratio between the incident and outgoing waves.

P-wave propagation across a thin layer satisfies Snell's law, that:

$$\frac{c_{rock}}{\sin\alpha_1} = \frac{c_{fracture}}{\sin\alpha_2} = \frac{c_{rock}}{\sin\alpha_1} \tag{2.8}$$

where c_{rock} and $c_{fracture}$ are the P-wave velocities of the rock matrix and fracture respectively, and α_1 and α_2 are angles as indicated in Fig. 2.5. A result of this is that P-waves enter and leave the fracture at the same angle, but the raypath is offset during propagation through the fracture.

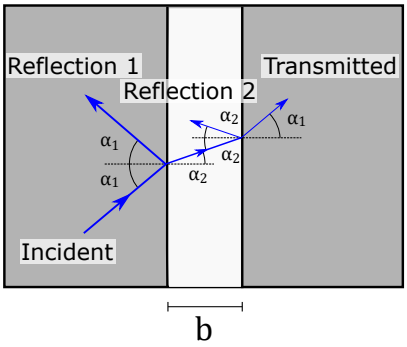

Figure 2.5: Schematic for P-wave propagation across a thin layer interface model, not considering mode conversions at boundaries. Note that in a TLIM, multiple reflections are generated at the fracture boundaries. Figures redrawn from similar in Li et al. (2014).

According to the displacement discontinuity model, fractures behave as low-pass filters with a cut-off frequency of ω_c (Pyrak-Nolte et al., 2017):

$$\omega_c = \frac{2K}{Z} \tag{2.9}$$

where K is the fracture specific stiffness (equation. 2.4 or 2.5) and Z is the seismic impedance of the rock matrix (velocity*density). The transmission coefficient, T, for a P-wave with a central frequency of ω crossing a fracture in an isotropic medium is (Pyrak-Nolte et al., 1990):

$$|T(\omega)| = \frac{1}{\sqrt{1 + (\frac{\omega}{\omega_c})^2}}, \tag{2.10}$$

Fractures with higher specific stiffnesses have higher cut-off frequencies (smaller $\frac{\omega}{\omega_c}$) and thus higher transmission coefficients. On the other hand, less stiff fractures have lower cut-off frequencies (higher $\frac{\omega}{\omega_c}$) and thus lower transmission

coefficients. Additionally, incident waves with higher central frequencies ω, (higher $\frac{\omega}{\omega_c}$), transmit less energy across a fracture.

In laboratory experiments, the amplitudes of waves exactly before and after a discontinuity cannot be directly measured. As a practical alternative, the transmission coefficient of wave incident on a single fracture is commonly defined as (e.g. Möllhoff et al., 2010, Nagata et al., 2014, Pyrak-Nolte, 2019):

$$T = \frac{A_{fractured}}{A_{intact}} \tag{2.11}$$

Where $A_{fractured}$ and A_{intact} are the amplitudes of the waves recorded at the receiver for a fractured and intact sample, respectively. Amplitudes may be estimated in the time or frequency domain. This approach suggests that if a wave was perfectly transmitted (T = 1) across a fracture, the recorded amplitude would be the same as that of the intact sample. Note that this is the same definition of transmission coefficient used in equation 2.5 to estimate dynamic fracture specific stiffness.

The amplitude of the arrival for the intact sample includes the effect of attenuation by geometrical spreading, internal friction and scattering. For the fractured sample, the arrival amplitude is also affected by the fracture. Attenuation for both samples due to geometrical spreading is equal as long as the source-receiver configuration is identical. Furthermore, attenuation due to internal friction and scattering could be assumed to be similar if the samples are of the same lithology. Thus, by looking at the ratio of the two signals, the causes of attenuation due to the source-receiver configuration and rock matrix are cancelled out to reveal the effect of the fracture (e.g. Barbosa et al., 2019).

In practice, this definition of transmission coefficient (equation 2.11) is not without issues. First, there may be minor differences in the sample porosity and mineralogy that affect attenuation by internal friction and scattering. Secondly, some energy may be *transmitted* across the fracture but not arrive at the receiver due to scattering or the limited view of the fracture due to the source-receiver configuration (Acosta-Colon et al., 2009). Finally, factors of the experimental process such as the loading rate and permeability tests between loading steps may affect the arrival amplitudes. If there are differences in the experimental process of the intact and fractured samples, it may be challenging to compare first arrival amplitudes across tests.

2.4 Fluid Flow through Fractures

Flow through fractures is most simply conceptualised as flow between two smooth, parallel plates (Fig. 2.6). The fracture transmissivity, T, and permeability, k, can be approximated by the cubic law (Snow, 1969; Witherspoon et al., 1980):

$$T = \frac{b_H^3}{12}, \qquad k = \frac{b_H^2}{12} \tag{2.12}$$

where b_H is the hydraulic aperture. Darcy's law can be modified to calculate the volumetric flow rate, Q, through a single fracture as:

$$Q = \frac{b_H^3 w}{12\mu} \frac{h_1 - h_2}{L} \tag{2.13}$$

where w is the fracture width (**not** the aperture), μ is the fluid viscosity, and the difference in hydraulic head $(h_1 - h_2)$ over the fracture length L is the hydraulic gradient. As the relationship between fracture flow and aperture is cubic, larger aperture fractures are able to transport significantly larger quantities of fluid.

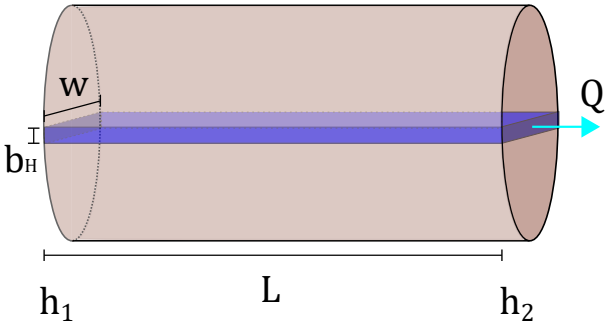

Figure 2.6: Flow through a fracture can be modelled as flow between two parallel plates. The difference in hydraulic head $(h_1 - h_2)$ at either side of the sample drives flow through the fracture at a volumetric flow rate Q.

Though the cubic law may be appropriate for fractures with reasonably smooth walls, many natural fractures have complex, rough surfaces and contact points which affect flow (Gudmundsson, 2011, p.473). For rough or partially filled fracture sets, flow channelling may occur in which most of the flow occurs along preferential paths.

The precipitation of minerals inside a fracture can significantly decrease its permeability. However, partially filled fractures may still contribute to flow parallel for two reasons. First, the flow through the fracture may be highly channelized. In this case, partial filling of the fracture may not affect the main channel through which fluid is flowing. Second, mineral veins or gouge material may form bridges between fracture faces which can increase the fracture stiffness and resist fracture closure, allowing channels to remain open at great depths (e.g. Banks et al., 1996; Laubach et al., 2004; Lang et al., 2016).

PART I

Laboratory Experiments

CHAPTER 3

Experimental Method

3.1 Experimental Setup

Flow and stiffness tests were conducted on the four samples at the Norwegian Geotechnical Institute (NGI), from 2016 to 2017. The experimental method is described in detail in Skurtveit et al. (2020) and Skurtveit et al. (2018). Further details on the equipment and standard testing procedures are given in Berre (2011). Here I include a short summary with focus on the velocity measurements.

Two strain sensors (linear variable differential transformers, or LVDT sensors) were used to measure the strain in the radial direction (Fig. 3.1). One set of sensors measured parallel to the fracture and the other measured perpendicular. Piezoelectric transducers were used to send and receive P- and S- waves. The received waves were recorded on a digital oscilloscope. The acoustic velocity sensors were placed such that the radial P-wave velocity was measured approximately parallel ($\sim$20°) to the fracture, and radial S-wave velocity measurements were approximately perpendicular ($\sim$70°) (Fig. 3.1). Additional strain and velocity sensors measured strain, P- and S- wave velocities in the axial direction, though the exact placement of the axial sensors was not documented. Sensors were placed in the same positions relative to each other for the intact reference samples.

Samples were placed in a triaxial cell and isotropic pressure was applied through oil pressure in the main chamber. Isotropic stress conditions of 1 - 9 MPa during the tests were chosen to reflect the shallow depth (25 and 46 m) of the samples (Fig. 3.2). To begin, an effective confining pressure of 1 MPa was applied as the samples were mounted. The samples were then saturated with 35 g/L NaCl brine, similar to in situ conditions of the CO2W55 well (Kampman et al., 2013). The effective isotropic pressure was then increased in steps of 1 - 2 MPa up to a maximum of 9 MPa. Constant head flow tests were conducted during pauses in loading. Samples were then unloaded down to 1 MPa, and for three of the samples the loading cycle was repeated to investigate hysteresis effects (Fig. 3.2). Note from Fig. 3.2 that the total test duration and duration of individual steps in the loading cycle varied between tests. Ultrasonic measurements were taken semi-regularly, with an average of at least one measurement for every 0.2 MPa stress increase. Ultrasonic measurements were not taken at the same time as the flow tests. All samples showed hysteresis effects. For this study I decided

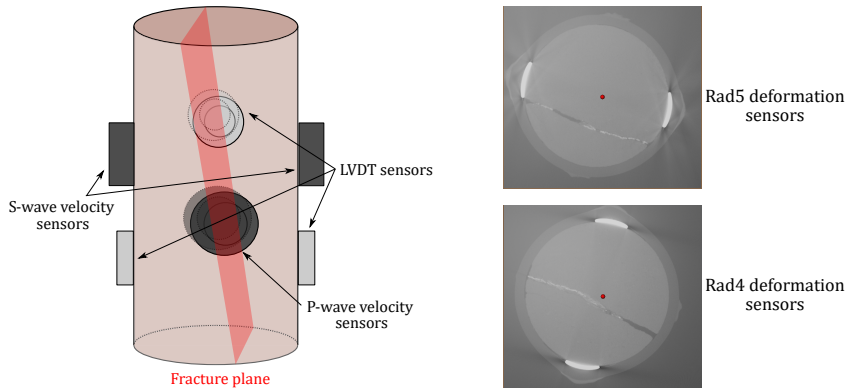

Figure 3.1: Sensor placements during testing. a) 3D schematic based on CT images. b) 2D CT images showing the positions of deformation sensors relative to the fracture. Note that these figures omit the sensors in the axial direction.

to look at only the ultrasonic measurements from the first loading part (1 - 9 MPa) of each test.

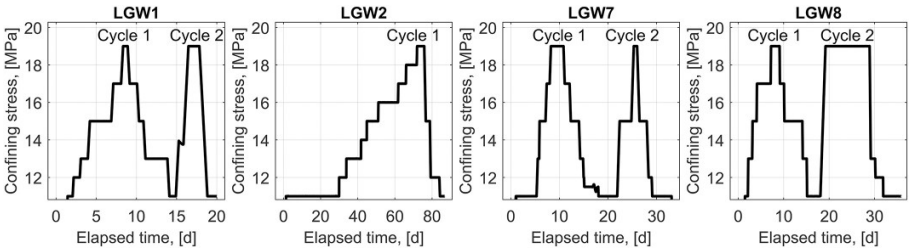

Figure 3.2: Total confining stress versus time for the different tests. Note the variations in loading rate within and across the first loading cycles of each test. The backpressure was 10 MPa. Figure reproduced from Skurtveit et al. (2020)

3.2 Ultrasonic Data Analysis

To pick the P- and S-wave arrival times, I used NGI's in-house software Time Picker (Fig. 3.3; e.g, Abbas, 2015; Tran, 2015; Nooraiepour et al., 2017). The script displays individual traces where arrival times can be picked, as well as an overview of all traces. I started by selecting first arrivals of the traces where the arrival is most clear, which was typically data collected under higher stresses. These picks acted as control picks. Then, I used the autopick function to automatically select first arrivals of the remaining traces and reviewed them manually. Finally, I exported the arrival times.

For some noisier traces, I tried applying bandpass filters to reduce noise and highlight the first arrival. For example, Fig. 3.4a shows a raw trace of an axial S-wave for sample LGW7 under 9MPa isotropic stress, and the trace after applying a 0.125 – 0.4 MHz Butterworth bandpass filter of order 4. The low

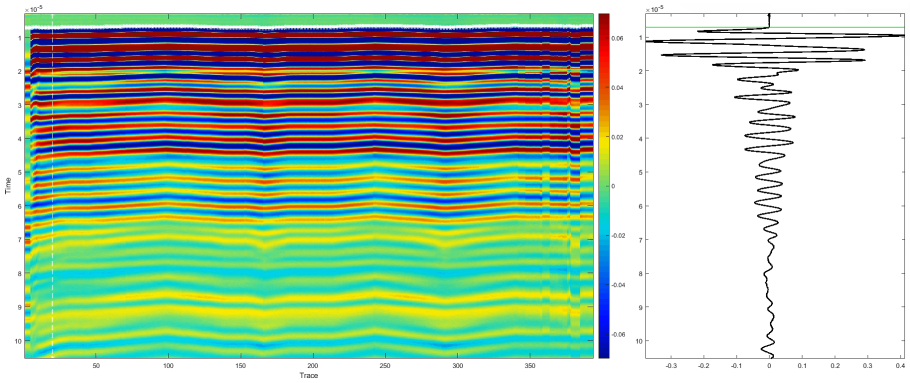

Figure 3.3: Screenshot from the Time Picker script showing how first arrivals are picked. (Left) Overview of all traces for the given sample, source type and direction. White crosses mark the automatic arrival picks. (Right) Selected trace with the pick marked as a green line.

and high frequency noise of the original trace has been reduced and the arrivals have become clearer (Fig. 3.4). It is important to note that filtering out certain frequencies can distort the signal so that arrivals appear earlier or later. To account for this, I picked the arrival times in the original traces and used the filtered traces as guides.

The P-axial and S-radial traces recorded for the thick fracture sample LGW7 were too noisy, even after filtering, to be included in this study. So, axial P-wave velocities were estimated from P-wave arrivals in the S-axial traces, and radial S-wave velocities were estimated from S-wave arrivals in the P-radial traces.

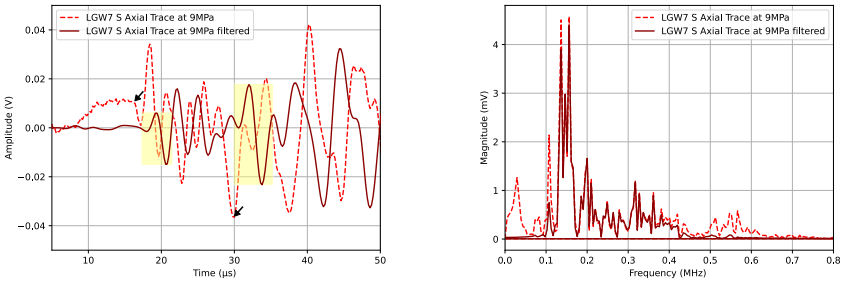

(a) (b)

Figure 3.4: a) Example S-wave trace for sample LGW7 (Thick fracture) and the trace after applying a Butterworth bandpass filter of order 4. The yellow boxes highlight the arrivals in the filtered trace, and the arrows indicate the picked P- and S-wave arrivals in the original trace. b) Spectral content of the traces in a) (entire record length = 1024μs).

There is no general agreement in the literature on where in the waveform to pick an S-wave arrival. According to Blewett et al. (1999), one major disadvantage of the time-of-flight method is that group velocity dispersion within the sample

causes different frequency components of the signal to arrive at different times, distorting the transmitted signal. This ambiguity in the arrival leads to there being four possible parts of the waveform that could be interpreted as the arrival (Fig. 3.5; Arulnathan et al., 1998). For this study, I decided to consistently pick the trough (point B) as the S-wave arrival, since this point was generally clearer than point A.

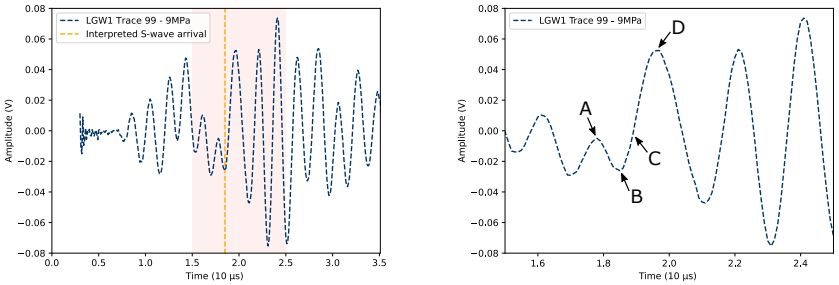

(a) (b)

Figure 3.5: (a) LGW1 Trace 99 at 9 MPa, a trace where the S-wave arrival was reasonably clear. (b) Zoomed-in section of (a), and points A-D indicating possible interpretations of the S-wave arrival. Figure (b) redrawn from similar in Arulnathan et al. (1998).

Next, I calculated velocities from arrival times using an adapted form of equation 2.7:

$$V = \frac{x}{T - T_0} \tag{3.1}$$

Where V is either the P- or S- wave velocity, x is either the height or diameter of the sample as measured by the strain sensors, T is the picked arrival time for the P- or S- wave, and T_0 is the travel time of the experimental setup without a sample (known as the zero or head-to-head reading). T_0 was measured for different source types and directions at one stress level and then assumed to be constant. The values for T_0 for different source types and directions are given in Table 3.1. After calculating velocities, I plotted them against isotropic stress.

Table 3.1: Zero readings T_0 for different source types and directions.

P-radial	S-radial	P-axial	S-axial
$0.68\mu s$	$1.06\mu s$	$4.69\mu s$	$6.05\mu s$

I also created plots of fracture deformation against stress, where fracture deformation d_f, or, the change in mechanical aperture Δb_m, is estimated by equation 3.2:

$$d_f = \Delta b_m = d_{Rad4} - d_{Rad5} \tag{3.2}$$

where d_{Rad5} is the diameter of the sample parallel to the fracture, representing the rock matrix deformation, and d_{Rad4} is the diameter of the sample perpendicular to the fracture, representing the combined deformation of the fracture and the rock matrix (Fig. 3.1b; Skurtveit et al., 2020).

To isolate P-wave first arrivals from later arrivals and reflections, I applied a half-cosine taper with a 4μs window to each trace, following Pyrak-Nolte et al. (1990) (e.g. Fig 3.6). I tried different taper lengths to ensure that the frequency content of the received pulse was not significantly distorted. To make the results comparable, I applied the same taper to all P-wave signals in the lab and modelling sections. After applying tapers, I measured the peak-to-peak amplitudes of the P-wave first arrivals and plotted them against stress.

To analyse the frequency content of the first arrivals, I applied a fast Fourier transform (FFT) to calculate the spectral amplitude distributions (e.g. Fig. 3.6b). To increase the frequency resolution of the FFT, I padded the signal vector with zeros. I then plotted the central frequency of the first arrival against stress, together with the peak-to-peak amplitude data.

I estimated the transmission coefficient of the thick fracture (LGW7) as the ratio of the Fourier spectrum of the signal from LGW7 to the Fourier spectrum of the signal from reference sample LGW8 (equation 2.11). From this, I then estimated the apparent dynamic fracture stiffness of sample LGW7 using equation 2.5. I used a dominant frequency, f, of 0.27 MHz from the FFT of the LGW7 trace at 1MPa (see Fig. 4.3b in the results) and a constant density of 2,400 kg/m3 (Table 1.1). At each stress point I took the velocity of the intact sample LGW8 as the phase velocity (see Fig. 4.1a in the results). The dynamic fracture stiffness is apparent since P-wave propagation in the laboratory experiments was not perpendicular to the fracture plane (Figs. 2.2 and 3.1).

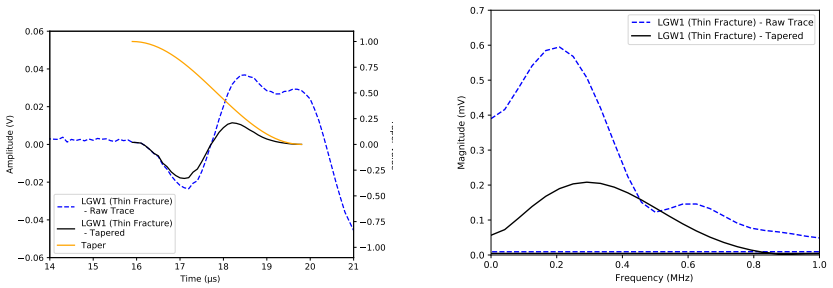

(a) (b)

Figure 3.6: Example of taper applied to a LGW1 P-wave first arrival. a) Original trace, half-cosine taper with a 4μs window and tapered version of the trace. b) Spectral content of the original trace (4μs window) and tapered version.

Velocity Measurement Uncertainty

To estimate the uncertainty in velocity measurements, I followed the analysis presented in Nooraiepour et al. (2017), which is similar to the method used by Hornby (1998) and Yin (1993). Equation 3.1, used to calculate the velocities, can be expanded in terms of partial derivatives to estimate the maximum absolute error in the velocity measurements as:

$$\Delta V = \Delta x \Big| \frac{1}{T - T_0} \Big| + 2x \Big| \frac{\Delta T}{(T - T_0)^2} \Big| \tag{3.3}$$

where Δx is the absolute error in the sample height or diameter, and ΔT is the time resolution for ΔT and ΔT_0 (Nooraiepour et al., 2017). The precision of the LVDT sensors used to measure sample height and diameter is reported to be 0.1 - 0.25% (RDP Electronics, 2021). To estimate the error Δx I used an average sample diameter and height of 25.5 mm and 52.1 mm, respectively. The precision of first arrival picks in the Time Picker software is 0.1 - 0.025 μs for P-waves and 0.2 - 0.025 μs for S-waves (Nooraiepour et al., 2017). However, the limiting factor is the sampling interval used for digitising the waveform, which was 0.1 μs for samples LGW1, LGW2 and LGW8, and 0.2 μs for sample LGW7 (Thick Fracture). The second term in equation. 3.3, related to the uncertainty in time picks, contributes approximately 95% of the total calculated error. Since the sampling interval of traces for sample LGW7 was twice that of the other samples, the estimated errors for that sample are almost twice as large.

For each source type and direction, I estimated the minimum and maximum errors using minimum and maximum values of T, the measured arrival time. Tables 3.2 and 3.3 show the relative errors for each source type and direction for typical velocities (Figs. 4.1 and 4.2 in results), using sampling rates ΔT of 0.1 μs and 0.2 μs, respectively. Measurements of P-wave arrivals in the radial direction have the largest absolute and relative error, since they have the smallest $T - T_0$. Absolute errors are between $\pm$110 and 190 m/s for samples LGW1, LGW2 and LGW8, and between $\pm$220 and 370 m/s for LGW7. Conversely, measurements of S-wave arrivals in the axial direction have the smallest absolute and relative error, since they have the largest $T - T_0$. Absolute errors are between $\pm$15 and 20 m/s for samples LGW1, LGW2 and LGW8, and between $\pm$30 and 60 m/s for LGW7.

Table 3.2: Minimum and maximum relative errors in velocity measurements at typical velocities for samples LGW1, LGW2 and LGW8 ($\Delta T = 0.1\mu s$).

Source type, direction	Typical Velocity (m/s)	Min relative error ± (%)	Max relative error ± (%)
P, radial	4200	3.0	4.5
P, axial	4600	1.5	2.0
S, radial	1600	1.5	2.0
S, axial	2200	1.0	1.0

Table 3.3: Minimum and maximum relative errors in velocity measurements at typical velocities for sample LGW7 ($\Delta T = 0.2\mu s$).

Source type, direction	Typical Velocity (m/s)	Min relative error ± (%)	Max relative error ± (%)
P, radial	4000	5.5	9.0
P, axial	4200	3.0	4.0
S, radial	1800	2.5	3.0
S, axial	2100	1.5	3.0

CHAPTER 4

Experimental Results

4.1 Velocity Measurements

All samples showed increasing velocities in both axial and radial directions under increasing isotropic stress from 1 to 9 MPa (Figs. 4.1 and 4.2). It is important to state that the error bars included in the plots, calculated using equation 3.3, represent only the uncertainty due to resolution limits of the experimental equipment, and do not take into account uncertainty in the first arrival picks themselves, for reasons such as those given in the discussion (section 5.1). The total uncertainty is likely larger than calculated, particularly for S-waves.

In the radial direction, the fractured samples show initially slower velocities, which then converge to values comparable with the reference samples (Fig. 4.1). The P-wave velocity of the thick fracture sample LGW7 increases from 3600 to 4300 m/s, whereas the thin fracture sample LGW1 velocity increases from 3900 to 4250 m/s. Compared to the thin fracture sample, the thick fracture sample shows larger differences in absolute value and gradient with respect to stress relative to its intact counterpart.

In the axial direction, P-wave velocities (Fig. 4.1b) were measured to be on average 10 - 15% faster than those measured in the radial direction (Fig. 4.1a). The P-wave velocity of the thick fracture sample LGW7 increases from 4000 to 4450 m/s, whereas the thin fracture sample LGW1 velocity increases from 4250 to 4650 m/s. The fractured samples show consistently slower velocities relative to their intact counterparts, even at higher stresses. The thick fracture sample again shows a larger difference relative to its intact counterpart than the thin fracture sample.

In both radial and axial directions, S-wave velocities increase near-linearly with stress, and estimates between sample pairs follow each other closely (Fig. 4.2). In the radial direction, the S-wave velocities of samples LGW7 and LGW8 increase from around 1750 to 1850 m/s. The S-wave velocities of samples LGW1 and LGW2 are slower, increasing from 1350 to almost 1500 m/s. In the axial direction, S-wave velocity estimates of samples LGW7 and LGW8 are 10% faster, consistent with the increases in P-wave velocities measured for all four samples (Figs. 4.1 and 4.2). The S-wave velocities of these samples increases from around 1950 to 2150 m/s. The S-wave velocity estimates of the samples LGW1 and LGW2, however, are approximately 60% faster in the axial direction, ranging from 2200 to 2450 m/s.

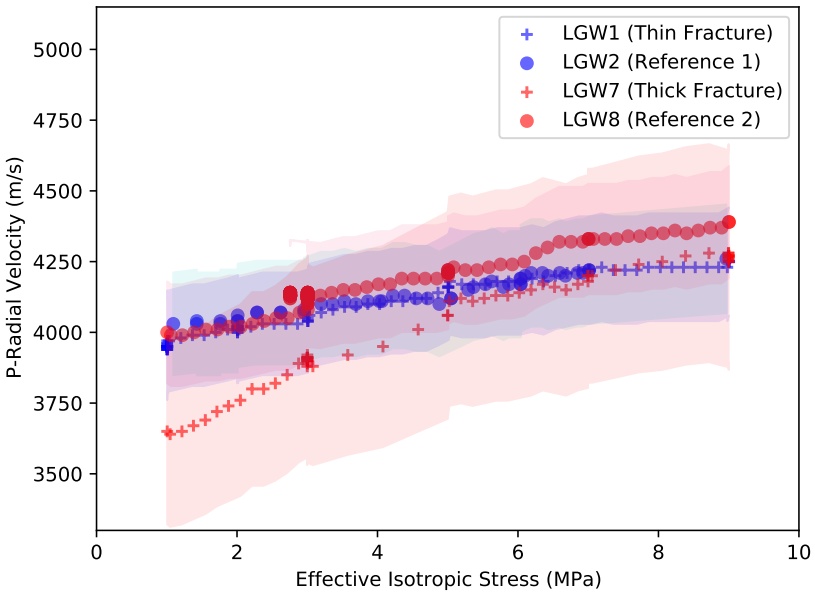

(a)

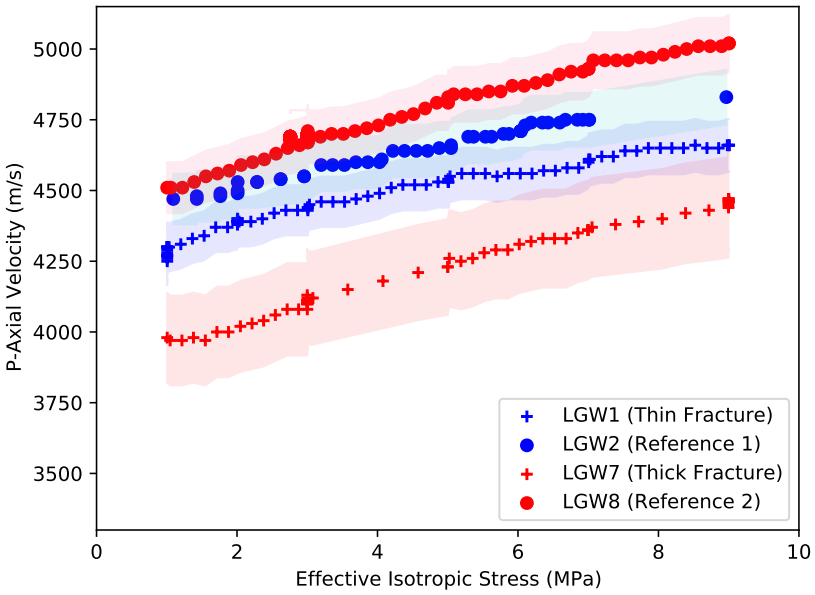

(b)

Figure 4.1: P-wave velocities measured in the a) **radial** and b) **axial** direction with increasing stress. Shaded areas indicate the maximum error ranges calculated from resolution limits of the experimental setup (Tables 3.2 and 3.3).

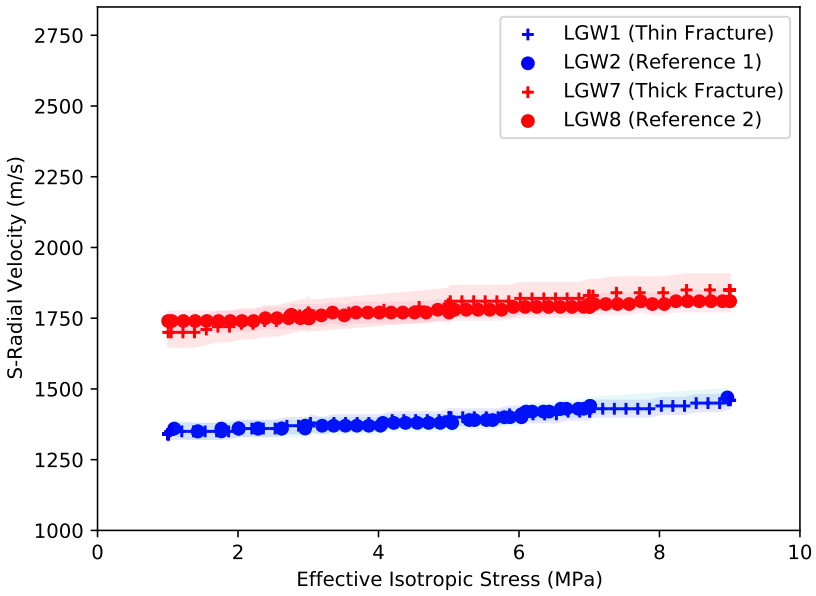

(a)

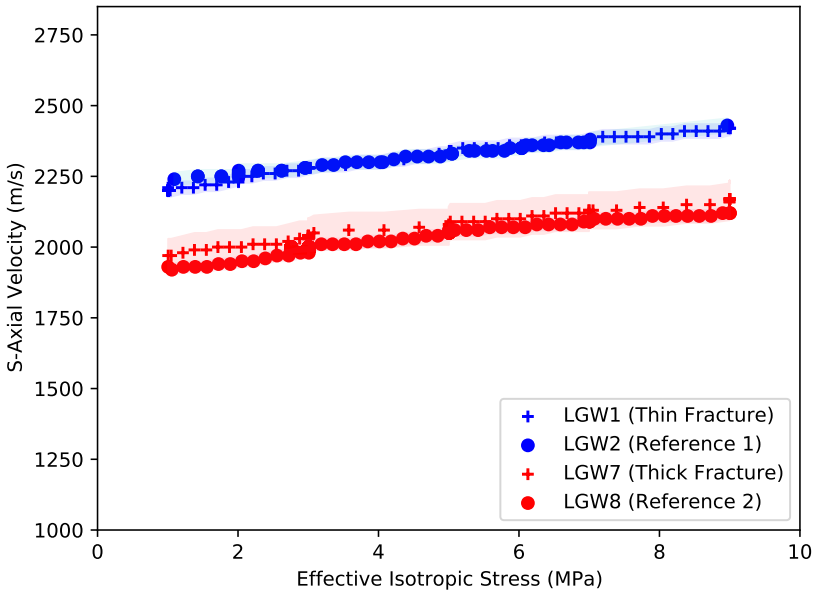

(b)

Figure 4.2: S-wave velocities measured in the a) **radial** and b) **axial** direction with increasing stress. Shaded areas indicate the maximum error ranges calculated from resolution limits of the experimental setup (Tables 3.2 and 3.3).

4.2 Amplitude and Frequency Analysis

Radial Direction

At 1 MPa, the peak-to-peak amplitude of the thin fracture sample LGW1 is 10% larger than that of its reference sample LGW2, whereas the peak-to-peak amplitude of the thick fracture sample LGW7 is almost five times smaller than that of its reference sample LGW8 (Fig. 4.3a and Table 4.1). The Fourier spectrum shows that, at 1MPa, the central arrival frequency for samples LGW1, LGW2 and LGW8 is around 0.32 MHz, whereas for sample LGW7 it is 0.27 MHz (Fig. 4.3b).

Generally, all samples show increasing peak-to-peak amplitudes and central frequencies with increasing stress (Figs. 4.4 and 4.5). Though, it seems that these measurements are dependent upon the loading cycle (Fig. 3.2), as individual loading steps can be identified in these plots. This is considered further in the discussion (section 5.2).

Figures including selected P-radial first arrivals and their Fourier transforms for the four samples under varying stresses are included in Appendix A for reference (Figs. A.1 to A.4).

Table 4.1: Summary of arrival times, peak-to-peak amplitudes and spectral maximums for P-wave arrivals in the **radial** direction under 1 MPa stress. See also Fig. 4.3. *Increase due to secondary consolidation.

Sample	Arrival Time + $T_0(\mu s)$	Peak-to-peak Amplitude (mV)	Spectral Maximum (mV)
LGW1 (Thin fracture)	7.0	315 - 340*	1.94
LGW2	6.9	285	1.74
LGW7 (Thick fracture)	7.7	140	0.54
LGW8	7.1	680	4.23

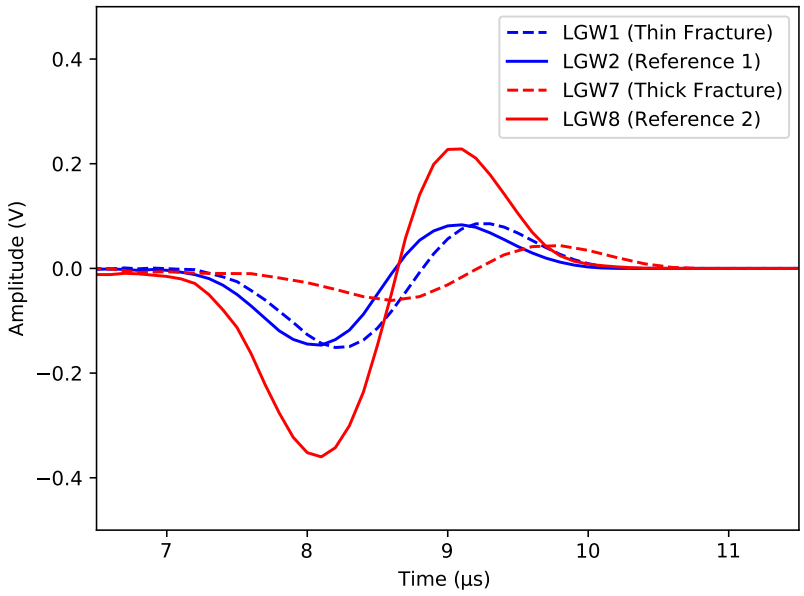

(a)

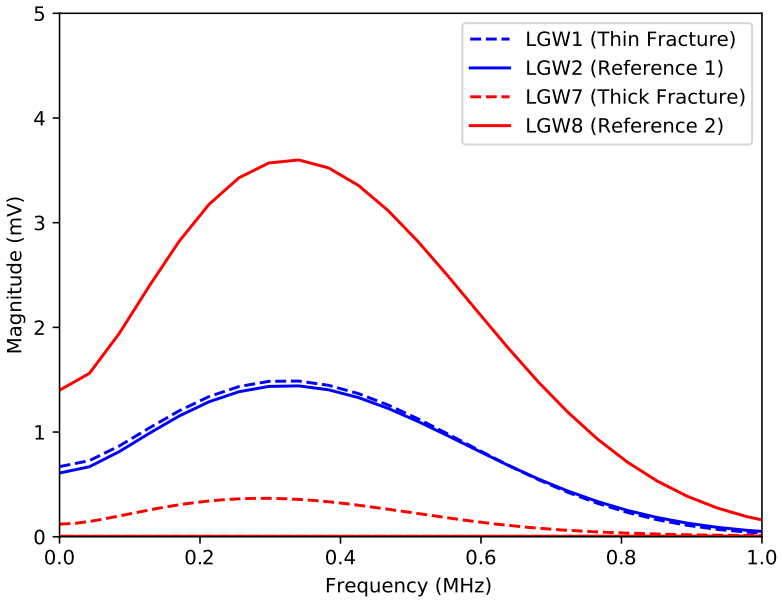

(b)

Figure 4.3: a) Tapered P-wave arrivals measured at 1MPa in the **radial** direction for the four samples and b) FFT of the traces in a). The P-wave for the thick fracture sample LGW7 arrives later with a smaller amplitude and lower central frequency.

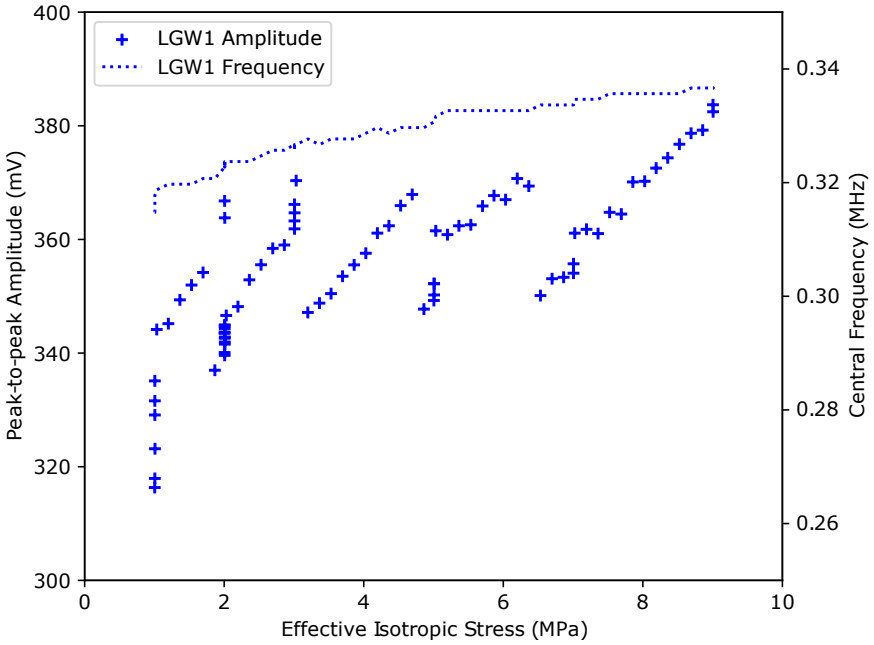

(a)

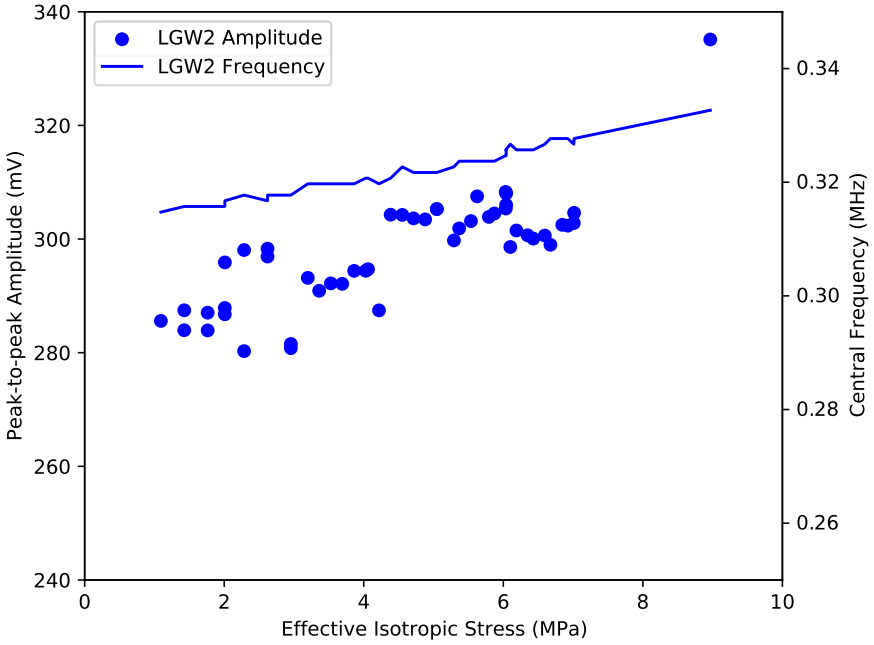

(b)

Figure 4.4: Peak-to-peak amplitude and central frequency of the first P-wave arrival measured in the **radial** direction under 1 - 9 MPa stress, for (a) LGW1 (Thin Fracture) and (b) LGW2 (Reference 1). Note the difference in y-axis limits.

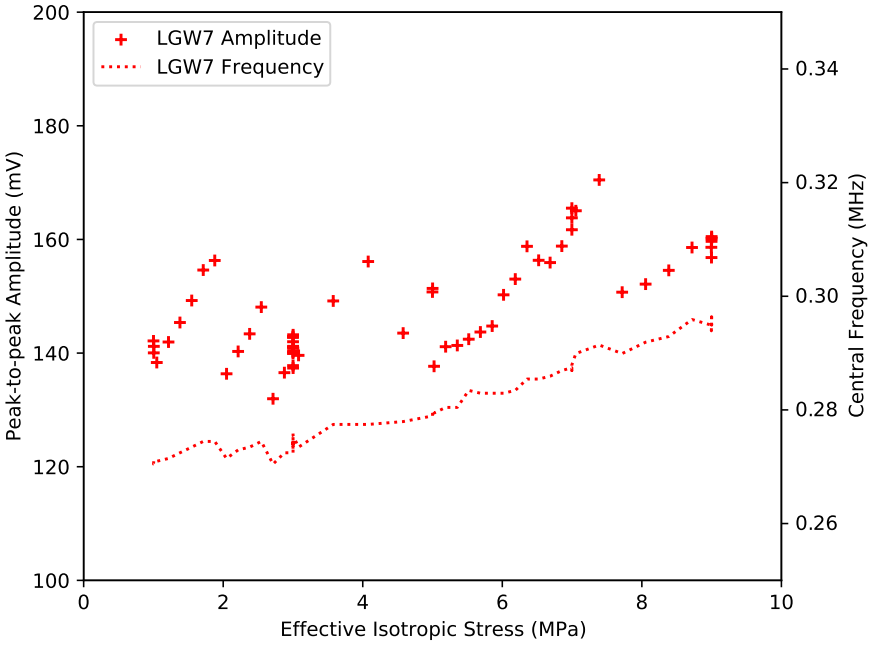

(a)

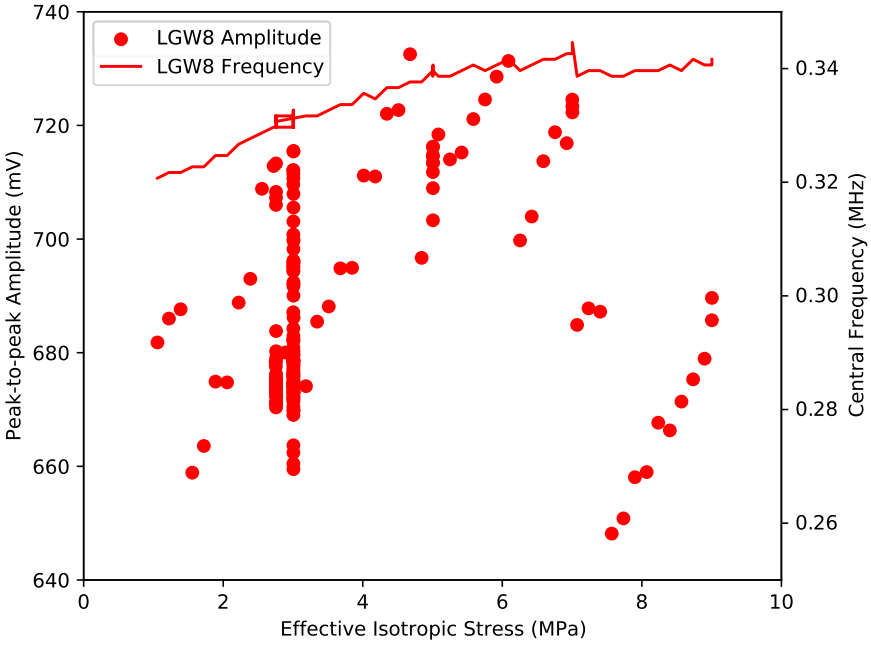

(b)

Figure 4.5: Peak-to-peak amplitude and central frequency of the first P-wave arrival measured in the **radial** direction under 1 - 9 MPa stress, for (a) LGW7 (Thick Fracture) and (b) LGW8 (Reference 2). Note the difference in y-axis limits.

Axial Direction

Compared to P-wave arrivals measured in the radial direction, those in the axial direction arrive later and with smaller amplitudes (Table 4.2 and Fig. 4.6). This could be expected since the waves propagated over a larger distance (52.1 mm as opposed to 25.5 mm in the radial direction).

Though the **radial** P-wave arrivals of LGW1 and LGW2 had similar arrival times and amplitudes, the **axial** P-wave of LGW1 shows a later arrival with a smaller amplitude relative to LGW2 (Table 4.2 and Fig. 4.6).

Unfortunately, the P-axial data for LGW7 was too noisy to use, so a comparison with reference LGW8 is not possible. The data for LGW8 also shows significant noise before the first arrival (Fig. 4.6 - before 16.5 μs). Though, the data is still usable and it can be noted that LGW8 again has the largest peak-to-peak amplitude, here 1.5 times larger than the other reference sample LGW2 (Table 4.2 and Fig. 4.6).

Table 4.2: Summary of arrival times, peak-to-peak amplitudes and spectral maximums for P-wave arrivals in the **axial** direction under 1 MPa stress. See also Fig. 4.6.

Sample	Arrival Time + $T_0(\mu s)$	Peak-to-peak Amplitude (mV)	Spectral Maximum (mV)
LGW1 (Thin fracture)	16.9	15	0.12
LGW2	16.4	60	0.42
LGW8	16.3	90	0.68

The peak-to-peak amplitudes of first P-wave arrivals measured in the axial direction increased near linearly with increasing stress (Figs. 4.7 and 4.8). The peak-to-peak amplitudes of P-axial waves are smaller in magnitude than the P-radial waves, and so have a lower signal-to-noise ratio. This leads to a higher uncertainty in the amplitude and central frequency values.

Figures including selected P-axial first arrivals and their Fourier transforms for samples LGW1, LGW2 and LGW8 under varying stresses are included in Appendix A for reference (Figs. A.5 to A.7).

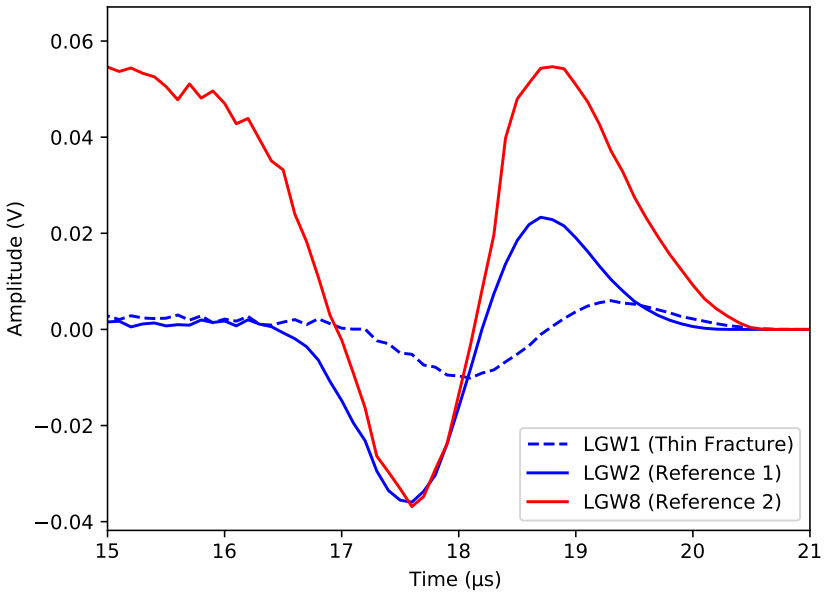

(a)

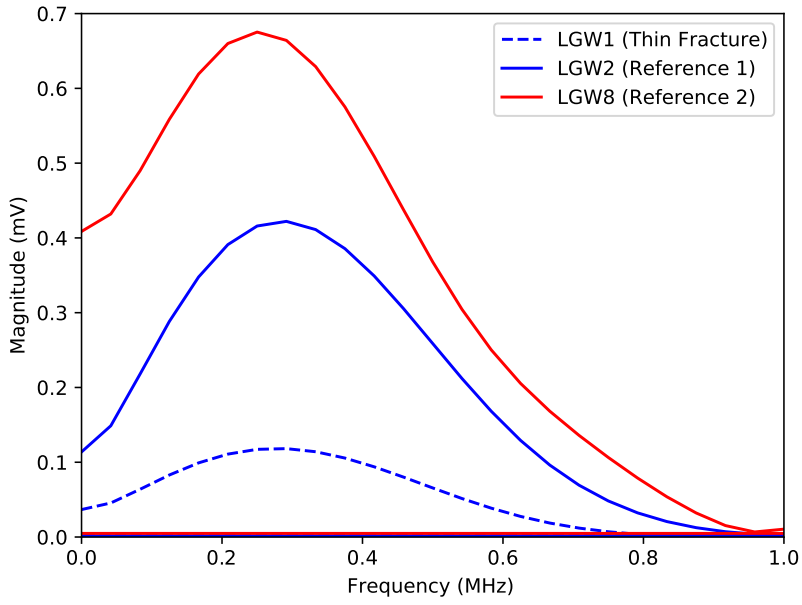

(b)

Figure 4.6: a) Tapered P-wave arrivals measured at 1MPa in the **axial** direction for three of the four samples and b) FFT of the traces in a). The P-axial data for LGW7 (Thick Fracture) was too noisy.

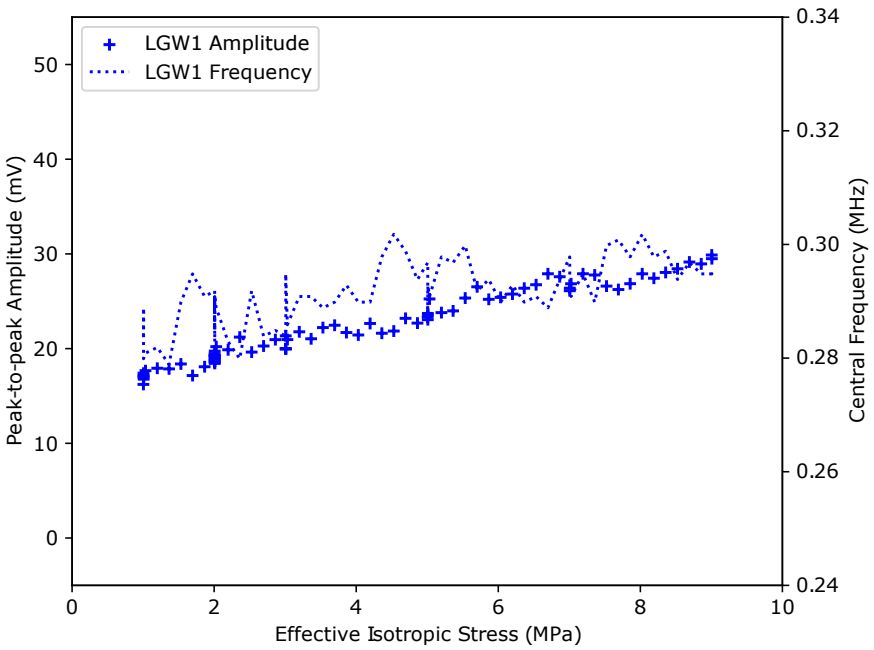

(a)

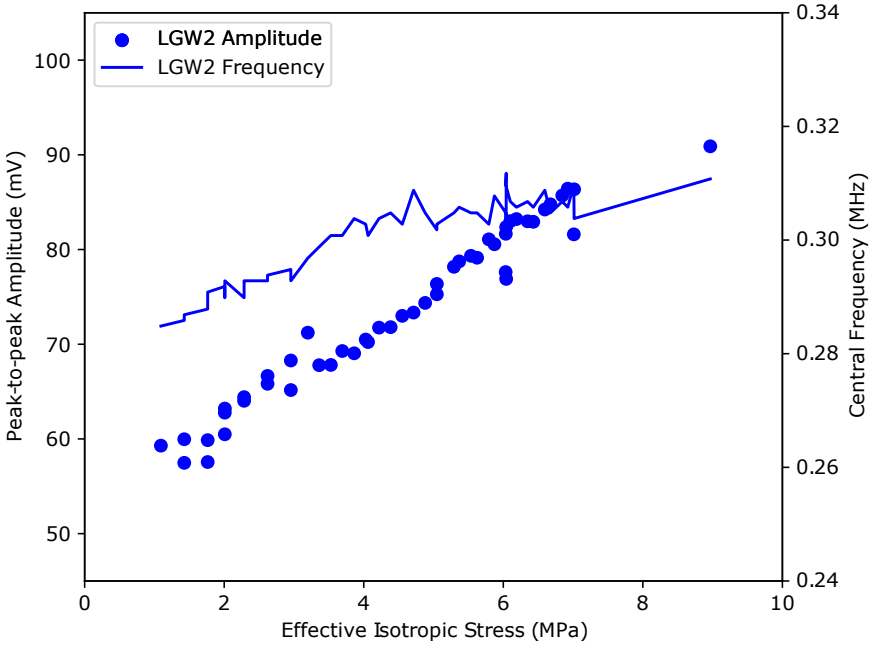

(b)

Figure 4.7: Peak-to-peak amplitude and central frequency of the first P-wave arrival measured in the **axial** direction under 1 - 9 MPa stress, for (a) LGW1 (Thin Fracture) and (b) LGW2 (Reference 1). Note the difference in y-axis limits.

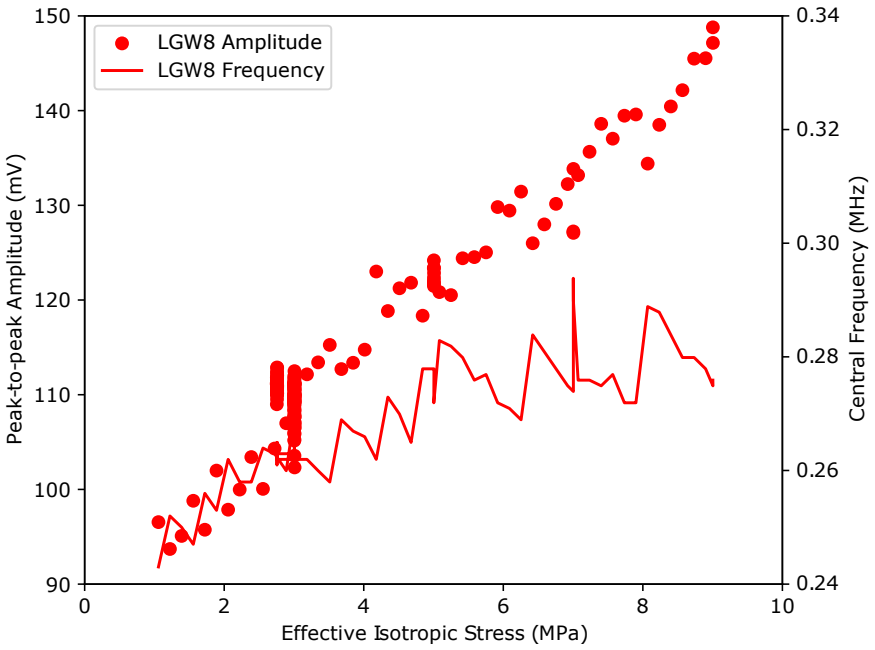

(a)

Figure 4.8: Peak-to-peak amplitude and central frequency of the first P-wave arrival measured in the **axial** direction under 1 - 9 MPa stress for LGW8 (Reference 2).

4.3 Fracture Deformation and Stiffness

I estimated fracture deformation for the two fractured samples using equation. 3.2. Fracture deformation for the thin fracture sample LGW1 increased linearly from 0.017 to 0.03 mm between 1 and 9 MPa (Fig. 4.9). More fracture deformation was observed for the thick fracture sample LGW7, which increased non-linearly from 0.10 to 0.18mm during loading.

Based on equation 2.5, the dynamic specific stiffness of the LGW7 fracture is estimated to vary between 1000 and 1400 MPa/mm (Fig. 4.10). The calculated dynamic fracture stiffness increases with stress, and is on the same order of magnitude of the static fracture stiffness estimates by Skurtveit et al. (2020). Though, it is important to note that equation 2.5 is only strictly valid for wave propagation normal to the fracture plane, which was not the case in this study (section 3.1). The dynamic stiffness of the LGW1 fracture could not be estimated from the P-radial data in the same way, since the peak-to-peak amplitudes of the fractured sample are actually higher than the intact reference ($T > 1$ according to equation 2.11) (Fig. 4.3).

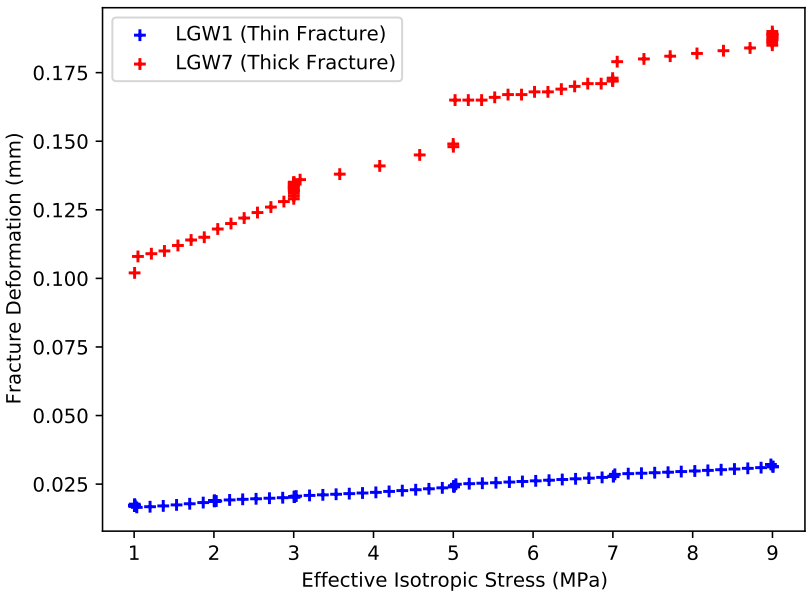

Figure 4.9: Fracture deformation of samples LGW1 and LGW7, calculated using 2.5, against effective isotropic stress.

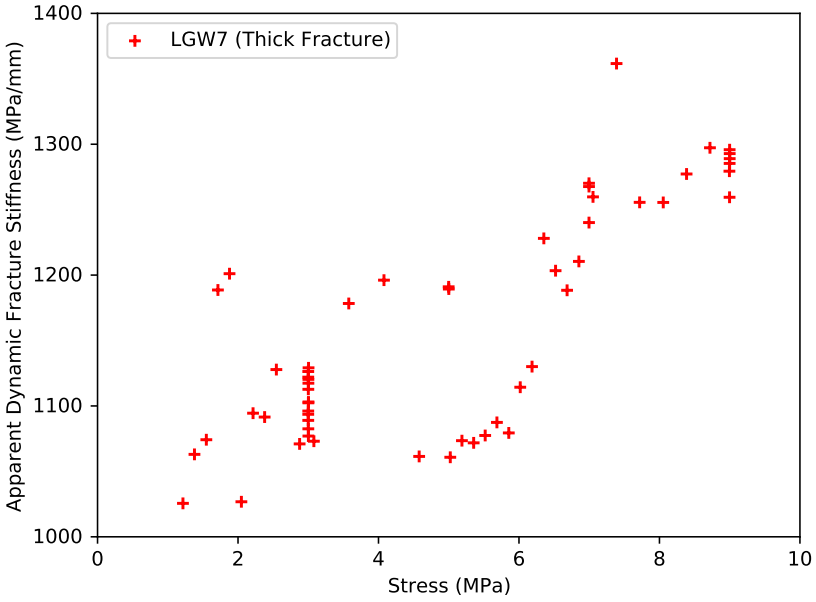

Figure 4.10: Apparent dynamic specific fracture stiffness of sample LGW7 calculated using equation. 2.5, between 1 and 9 MPa. These values are estimates since wave propagation was not normal to the fracture.

CHAPTER 5

Experimental Discussion

The aim of the experiments was to investigate how the fractures in samples LGW1 and LGW7 affect the ultrasonic wave propgation. Under this aim there are three questions to answer: 1) To what extent are the fractures detectable? 2) Can closure of the fractures under increasing stress be identified? and finally 3) Can the ultrasonic data be related to results of the flow tests?

5.1 Detecting Fractures

The fractures in samples LGW1 and LGW7 may be detected by comparing data from the fractured samples to their intact counterparts. Since both samples record the attenuation of the wave through the core sample, any difference in arrival time, amplitude or frequency can, in principle, be attributed to the fracture. In practice, discrepancies between the two datasets may arise due to differences in transducer-sample contact, heterogeneous distribution of dense minerals and porosity in the samples, or other unknown factors which affect fracture visibility.

The thick fracture in sample LGW7 is clearly visible in the ultrasonic data as the radial P-waves arrive later, with smaller amplitudes and lower central frequencies relative to the intact sample LGW8 (Fig. 4.3). On the other hand, the thin fracture in sample LGW1 is less visible in the radial data as the P-wave arrives with a similar amplitude and central frequency to the intact sample LGW2 (Fig. 4.3). The thin fracture can only be identified in the radial direction by the 0.1 μs delay relative to LGW2. That the P-radial wave in LGW1 arrives with a similar amplitude and frequency to its reference sample could be related to the thin aperture and relatively high contact ratio of the fracture (Fig. 1.3 and Table 1.2).

The thin fracture seems to affect wave propagation more in the axial direction, as the axial P-wave arrives later and with a smaller amplitude relative to LGW2 (Table 4.2 and Fig. 4.6). This could indicate attenuation by the fracture, or be due to differences in sample layering or porosity between LGW1 and LGW2. Unfortunately the exact position of the P-wave transducers in the axial direction is unknown and so it is difficult to distinguish between the effect of the fracture and other variables.

S-wave First Arrival Uncertainty

Previous experimental work has shown that fractures can largely affect the velocity and attenuation of S-waves (e.g. Nara et al., 2011; Kamali-Asl et al., 2019). One may have expected the S-waves to be more affected than P-waves in the experiments since they cannot travel through liquids and they were travelling near normal to the fracture plane (Fig. 3.1). Additionally, the wavelength of S-waves is shorter so the fracture would appear larger than for the P-waves. Thus, it was surprising that in this study, S-waves appear insensitive to the fractures. Or in other words, the fractures could not be detected using S-waves. This may be explained by the large uncertainties surrounding the S-wave arrival picks.

For both P- and S-waves, traces recorded at lower stresses typically showed less clear arrivals than traces at higher stresses (e.g. Fig. 5.1). This could be due, in part, to poorer contact between the piezoelectric transducers and the samples at lower stresses, a commonly reported issue (Pyrak-Nolte et al., 1990; Allen et al., 2017; Nooraiepour et al., 2017). S-wave arrivals at lower stresses are additionally difficult to pick since they can be obscured by the P-wave arrival. It is possible that the S-waves were attenuated by the fractures to such a large extent that the arrivals are invisible. In their study of fractured basalt samples, Nara et al. (2011) reported that for one sample they could not get sufficient signal amplitude for the S-wave below an effective pressure of 20 MPa, and for another sample a signal was not clear until 40 MPa. Rempe et al. (2018) also reported difficulties in identifying S wave arrivals for some samples, resulting in velocity uncertainties larger than 10%.

These factors affecting the clarity of S-wave arrivals introduce considerable doubt in the Time Picker autopick function to be able to accurately extrapolate S-wave picks (Fig. 5.1). For example, the S-radial arrival for LGW1 was picked manually for the 9 MPa trace, in which the arrival was most clear (Fig. 5.1a and c). However, the trough that was selected as the arrival does not exist in traces recorded under lower stresses, so the arrivals extrapolated using the autopick function are less clear.

For the reasons above, though the S-waves appear unaffected by the fractures in these experiments, the measurement uncertainty is too large to draw conclusions regarding the ability of S-waves to detect fractures.

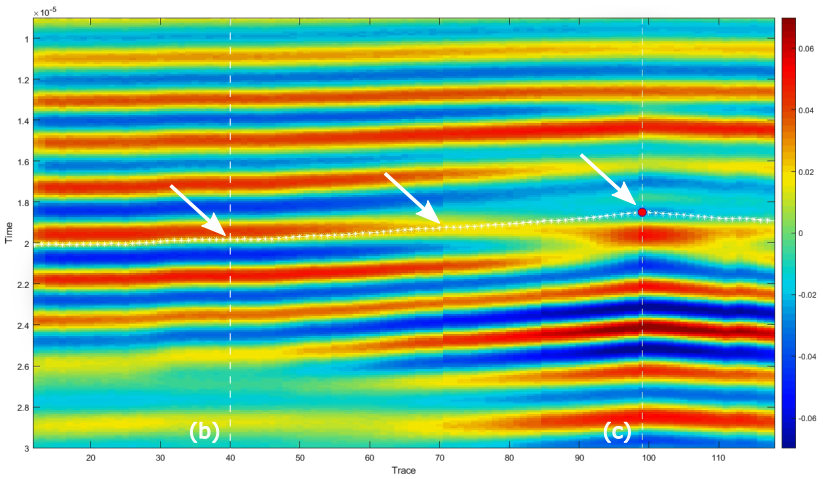

(a)

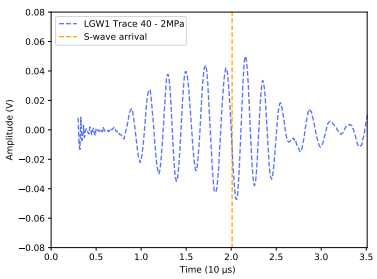

(b)

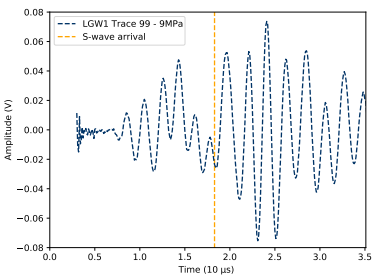

(c)

Figure 5.1: a) A screenshot from Time Picker indicating the challenge in extrapolating picks across different stresses. White arrows indicate the 'path' of picks. b) LGW1 at 2 MPa (Trace 40), where the selected trough has disappeared and the S-wave arrival is unclear. c) LGW1 at 9 MPa (Trace 99), where the S-wave arrival was picked.

5.2 Identifying Stress Dependent Fracture Closure

During the experiments, the fractures in samples LGW1 and LGW7 closed and deformed under increasing isotropic stress. Fracture closure can be identified in the ultrasonic data by faster arrival times, larger amplitudes and or higher central frequencies. A note of caution is due here since these trends can also be caused by improving contact between the piezoelectric transducers and the sample, as well as porosity reduction of the samples under increasing stress. Furthermore, variations in the loading cycle (Fig. 3.2) and changes in pore pressure within the fracture during flow tests (Fig. 1.5) also introduced significant noise to the ultrasonic data, particularly the peak-to-peak amplitudes. These factors make it challenging to identify fracture closure, and the results should be viewed with caution.

Nevertheless, the most convincing evidence of fracture closure is in the P-radial velocity estimates for the thick fracture sample LGW7 (Fig. 4.1a). From 1 to 5 MPa, the P-radial velocity of LGW7 increases faster than other samples and approaches the P-radial velocity of its intact counterpart, LGW8. This interpretation of fracture closure is supported by the fracture deformation data, which shows decreasing rates of deformation with stress as the fracture closes and increases in stiffness (Fig. 4.9).

While the thick fracture of LGW7 is visible in the amplitude and frequency data, *closure* of the fracture under stress in this data is not clear (Fig. 4.5aa). There is no clear trend in the amplitude data and the increase in frequency with stress is similar to that of the reference sample LGW8. Between 1 and 3 MPa, the amplitude and frequency data show a kind of sawtooth pattern, with increases during the loading steps and sharp decreases at the end of each step (Fig. 5.2a). One possible explanation for this is that the fracture was closing with increasing stress, then partially reopening during the flow tests at the end of each loading step. This would indicate that the amplitudes and frequencies are sensitive to the state of the fracture, but the data lacks a clear overall trend (Fig. 5.2a).

For the thin fracture sample LGW1, the P-radial velocity measurements also suggest fracture closure between 1 and 3 MPa, as the velocity of LGW1 increases and approaches the velocity of its reference sample, LGW2 (Fig. 4.1). The fracture deformation data is less clear, showing linear deformation with increasing stress (Fig. 4.9).

Interestingly, though the thin fracture is invisible in the amplitude data, closure of the fracture with increasing stress may be visible in the relative amplitude changes (Fig. 5.2b). The amplitude data again show a kind of sawtooth pattern across the loading steps, but from 1 to 3 MPa the minimum amplitude increases from 315 to 345 mV. Though, secondary consolidation is clearly visible at 1, 2 and 3 MPa and it is unclear how this affects the trends. It could be argued that secondary consolidation and or improved contact with the transducers and core sample causes the increase in minimum amplitude, rather than closure of the fracture.

From the limited results in this study, I conclude that reductions in fracture aperture with increasing stress are most reliably quantified by P-wave velocity

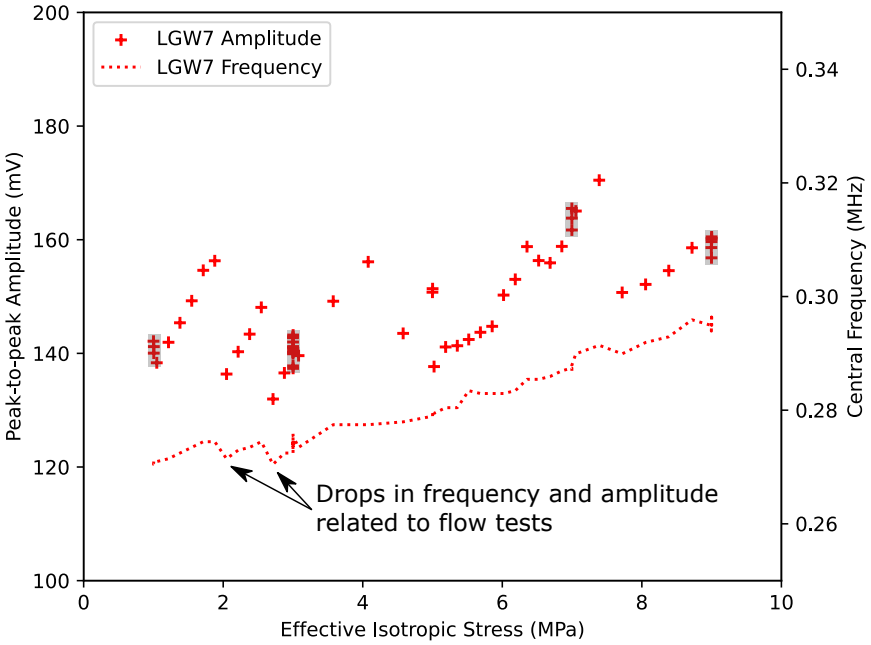

(a)

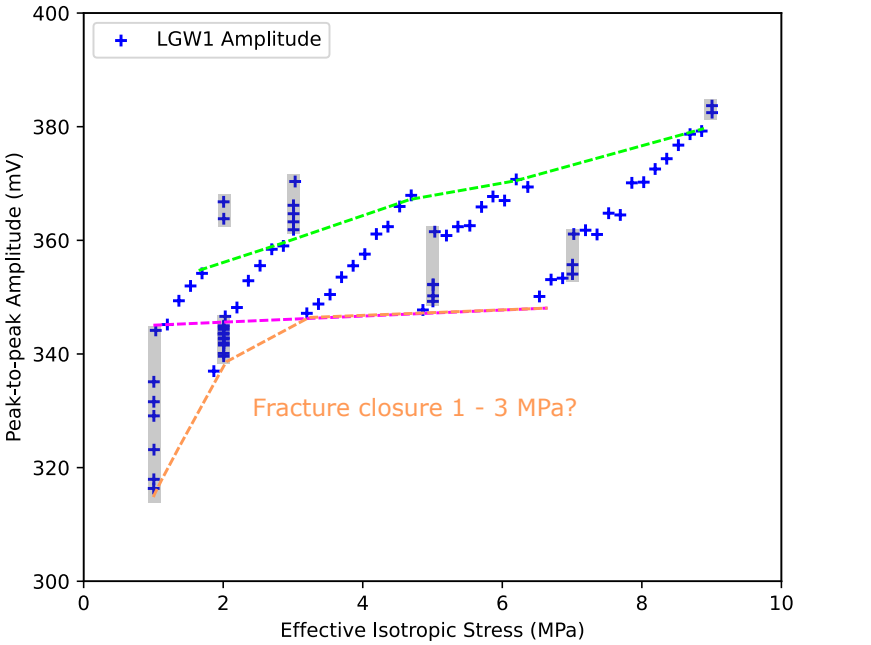

(b)

Figure 5.2: Possible interpretations of fracture closure in the amplitude and frequency data for a) Thick fracture sample LGW7 and b) Thin fracture sample LGW1. Grey areas highlight amplitude changes due to secondary consolidation.

measurements across the fracture. The results suggest that the amplitude and frequency of first arrivals are also sensitive to the state of the fracture, but noise introduced by different loading rates and the flow tests made it challenging to compare results and identify clear trends.

5.3 Relating Ultrasonic Data to Flow Test Results

The final objective of the experimental section was to see if changes in the ultrasonic data could be related to changes in fracture permeability measured during the flow tests (Fig. 1.5; Skurtveit et al., 2020).

The decreases in permeability measured for LGW7 correlate very well with the interpretation of fracture closure from velocity measurements (velocity of intact sample - velocity of fractured sample) (Fig. 5.3a). The sharp reduction in permeability between 1 and 3 MPa is accompanied by a sharp decrease in the difference in P-radial velocities between LGW7 and LGW8. The difference in P-radial velocities between the two samples further decreases and stabilises around 5 MPa, similar to the permeability.

Since the peak-to-peak amplitude and frequency data of LGW7 did not capture the fracture closure, it does not relate well to the permeability data either (Figs. 5.2a and 5.3a). The estimates of dynamic stiffness for LGW7 do show increasing stiffness with stress, but the gradient and magnitude of the curve do not match well with the flow test results (Fig. 4.10).

The decreases in permeability measured for LGW1 correlate fairly well with the interpretation of fracture closure from velocity measurements and, possibly, amplitude data (Fig. 5.3b). The permeability of the thin fracture seems to stabilise between 3 and 7 MPa, but a sudden decrease in flow was observed between 7 and 9 MPa. Skurtveit et al. (2020) suggested that this could be explained by either possible mating of the fracture surfaces or particle clogging of the small aperture at the top of the sample. The particle clogging hypothesis seems most plausible since the ultrasonic data does not show a similarly abrupt change between 7 and 9 MPa that would correspond to an increase in fracture contact area.

These experiments have shown that it is possible to relate seismic measurements of fractures to their permeability. In particular, faster P-wave velocities can be related to stiffer fractures with smaller apertures and lower permeabilities (Figs. 1.5, 4.1, 4.3 and 5.3). This finding supports the work of other studies in this area linking decreases in fracture aperture and permeability with increases in velocity (Pyrak-Nolte et al., 1987, Nara et al., 2011, Nara et al., 2012, Shokouhi et al., 2019, Kamali-Asl et al., 2019, Yu et al., 2019; Kewel, 2020).

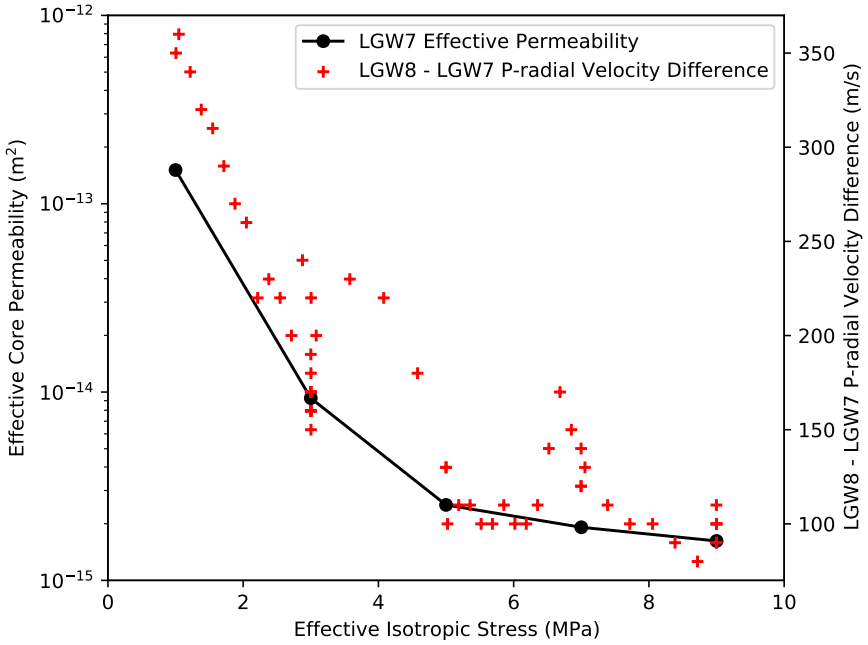

(a)

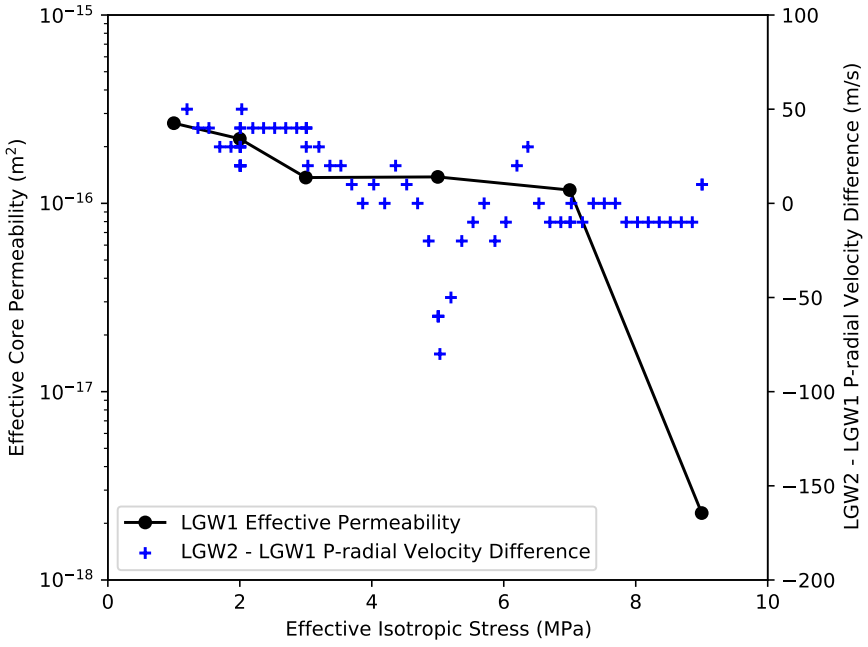

(b)

Figure 5.3: (Left axis) Effective core permeability measured during the flow tests (Skurtveit et al., 2020) and (right axis) P-radial velocity of **intact** sample - velocity of P-radial velocity of **fractured** sample for a) Thick fractured sample LGW7 and b) Thin fractured sample LGW1. Note the difference in y-axis limits.

PART II

Numerical Modelling

CHAPTER 6

Modelling Method

Based on the experimental work, I decided to run numerical models of ultrasonic wave propagation through a fractured sample to support and expand upon the laboratory results. With numerical models, it is possible to systematically investigate how different fracture parameters affect wave propagation in a way that would not be possible using only laboratory methods.

Early on, it was decided to run 2D models since they are less computationally expensive. I also decided to focus on wave propagation in the radial direction, since the experimental radial data quality was higher and the source and receiver locations were more well constrained than in the axial direction. Furthermore, in the models I only looked at P-wave first arrivals, since in the experimental section the S-wave data showed little variation.

The models presented here are simplified representations of the naturally complex core samples. Though, the results can still be useful in understanding wave propagation across single fractures. The known assumptions and limitations of the models in this study are considered in the discussion (section 8.2).

6.1 Modelling Workflow

To create and run the numerical models, I followed COMSOL's 8 steps of the modelling workflow (COMSOL, 2021). This method section follows this order:

1. Setting up the model environment.
2. Creating definitions (e.g. source signal function).
3. Building the geometry.
4. Specifying material properties.
5. Defining boundary conditions.
6. Creating the mesh.
7. Running the simulation.
8. Post-processing of results.

First, I aimed to setup a model that recreated measurements from the laboratory experiments (e.g. Fig. 4.3). The intact reference model was setup as depicted in Fig. 6.1a. The source and receiver were approximated as 3mm boundaries, matching the size of the piezoelectric transducers used in the lab. A P-wave is generated at the source edge, which then propagates through the core sample and is recorded at the receiver edge. The fracture model contained an additional domain to model the fracture, as depicted in Fig. 6.1b. The fracture was placed at a 20° to match the CT scan data of LGW7 (Fig. 6.2). Note also from Fig. 6.2 that the fracture is well centered and symmetrical, so either piezoelectric transducer could act as the source or receiver.

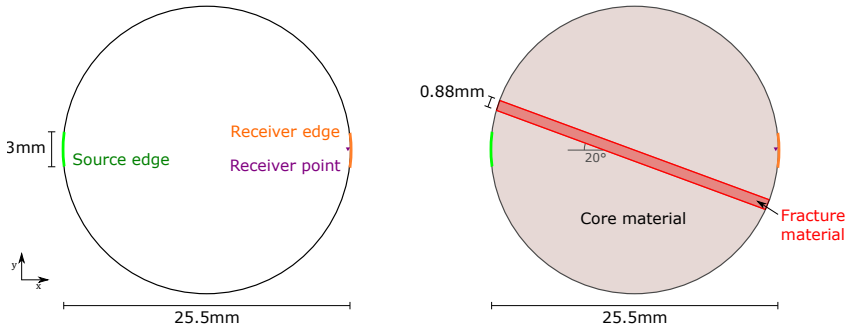

Figure 6.1: Schematics showing the model geometry for the (a) intact and (b) fractured models used for model calibration.

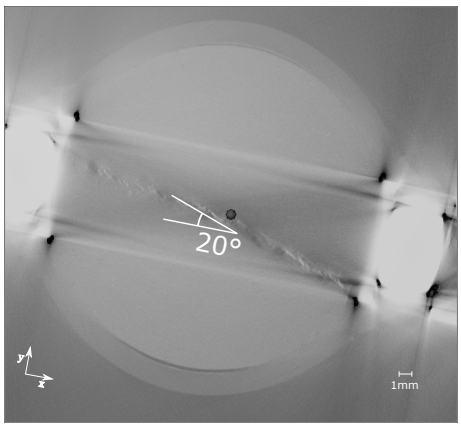

Figure 6.2: A CT image of LGW7 (Thick fracture) with the P-wave piezoelectric transducers on either side of the sample. Note that the fracture is at a 20° angle to the wave propagation.

The model parameters and material properties were selected to be as close to the experimental conditions as possible (Table 6.1). The core diameter (25.5mm), density and P- and S-wave velocities were chosen as average values of the lab data (Table 1.1, Figs. 4.1a and 4.2a). The Young's modulus was estimated from the drained bulk moduli of the intact samples, 1.5 – 3 GPa, as reported

by Skurtveit et al. (2020). The fracture infill density was calculated to be that of a 35 g/L NaCl brine, as was used in the laboratory experiments (Skurtveit et al., 2020). The Poisson's ratio was chosen as an average value for sandstones (Turcotte and Schubert, 2014, p.575). Finally, the simulations were run at room temperature and pressure.

Table 6.1: Summary of model parameters and material properties used in the numerical models. * These values, as well as the fracture roughness, were varied in the parameter study.

Core	Diameter (mm)	25.5
	Density (kg/m^3)	2500
	P-wave Velocity (m/s)	4000
	S-wave Velocity (m/s)	1800
	Poisson's Ratio	0.25
	Young's Modulus (GPa)	13.5
Fracture*	Angle from x-axis (°)	20
	Aperture (mm)	0.88
	Infill Material	Brine
	Infill Material Density (kg/m^3)	1024
	P-wave Velocity (m/s)	1470
Piezoelectric Transducers	Diameter (mm)	3

The models were setup using the domains and boundaries as represented in Fig. 6.3. The core domains were modelled using the **Elastic Waves, Time Explicit**[1] (elte) interface. The fracture domain, when modelled as a non-solid, was modelled using the **Pressure Acoustics, Time Explicit** (pate) interface. The boundaries between these two domains was modelled using the **Acoustic-Structure, Time Explicit Boundary**. The outer boundaries were modelled as **Fixed** for the elastic domain and **Sound Hard Boundary** for the acoustic domain, as the samples in the laboratory were held fixed in place. The source was generated using a **Boundary Load** boundary condition on the source edge, which exerted a total force against time as defined by the source function.

The last step before running the simulation is to generate a mesh (e.g. Fig. 6.4). For all models I used a **Free Triangular** mesh with a maximum element size, h_{max}, given by:

$$h_{max} = \frac{c_{min}}{3f_0} \tag{6.1}$$

where c_{min} is the minimum wave speed, and f_0 is the central frequency of the source function. Note in Fig. 6.4 how the mesh is refined close to the receiver point.

I then ran the models using a **Time Explicit** solver with the Runge-Kutta method of order 2. I ran the model twice: once at coarse time steps (1μs) that saved the solution for the entire model domain, to create snapshots of the wave propagating through the sample. Then again with a finer time

[1] Terminology here in bold relate to specific terms used in COMSOL Multiphysics.

resolution (0.1μs) that saved the solution only at the receiver edge, to record what would be measured by the receiving transducer. After running the models, I then integrated the **particle velocity (x direction)** measured at the receiver against time to obtain the displacement against time. I then converted the displacement into voltage by multiplying it by the piezoelectric constant of 375e-12 m/V (Boston Piezooptics, 2021). Finally, as with the lab data, I applied a 4μs half-cosine taper to the first arrival (e.g. Fig. 3.6).

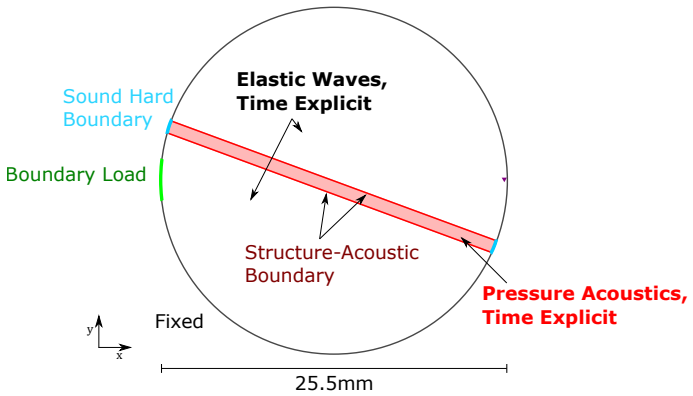

Figure 6.3: Schematic showing the model domains (bold) and boundaries in the fractured model when the fracture was filled with brine. For models in which the fracture was filled with a solid (e.g. calcite, pyrite), the fracture domain was modelled using the Elastic Waves, Time Explicit interface.

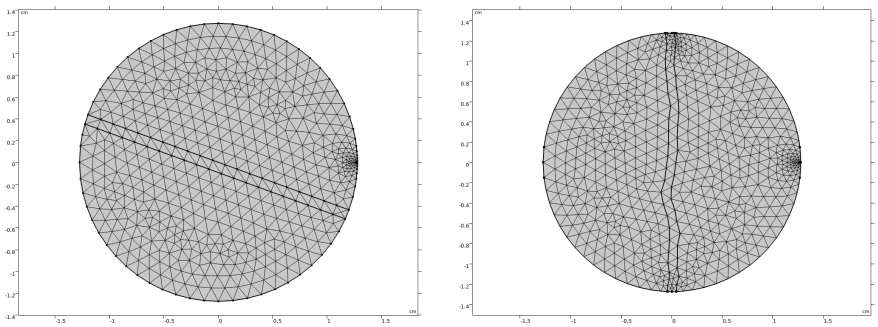

(a) (b)

Figure 6.4: Screenshots from COMSOL showing the mesh for a) the fractured model used in the calibration and b) a rough model (JRC = 9) used in the parameter study.

6.2 Model Calibration

The first part of the calibration was to find an appropriate source function that produced signals similar to those recorded in the experiments. This step is critical since how the wave interacts with the fracture is dependent upon its amplitude and frequency content (Theory section 2.3). In order for the model

results to be relatable to the laboratory data, the source function must have a comparable frequency content and amplitude.

In the laboratory, the source function depends upon the input signal used to excite the piezoelectric transducer as well as its resonant frequency. The input signal used in the laboratory experiments is unknown to the author, however Nooraiepour et al. (2017), who conducted similar experiments in the same laboratory, mentioned that the P- and S-wave transducers used had a resonant frequency of 500 kHz.

I considered three source functions: a Ricker wavelet, a Hanning [Hann] window and a sine function (Fig. 6.5). The Ricker wavelet and sine function are defined in terms of their central frequency and amplitude, and the Hanning window is defined in terms of its cut-off frequency and amplitude. I ran simulations of the intact sample while varying the frequencies and amplitudes of these three source functions. Of the three functions, the Hanning window fits the lab data the best in both the time and frequency domain (Fig. 6.6). From this, I decided to use a Hanning window with a cut-off frequency of 1 MHz as the source function in the models.

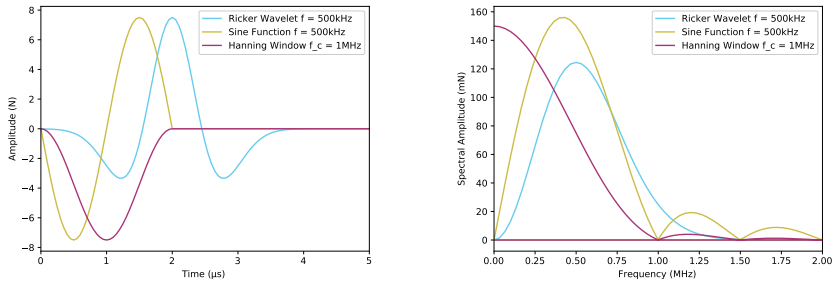

(a) (b)

Figure 6.5: Comparison of functions considered as source functions in the (a) time and (b) frequency domain.

After deciding on a source function, the next step was to calibrate a fractured model against the laboratory data. I did this by varying the fracture aperture and angle until a reasonable fit with the lab data was achieved. Specifically, I considered the arrival delay relative to the intact sample, the shape of the waveform and frequency content, and the decrease in amplitude as a result of the fracture. The fractured model was calibrated against laboratory data from the thick fracture sample LGW7 and its reference sample LGW8. I chose to focus on this dataset as, compared to LGW1, the LGW7 P-radial data has larger differences with its intact sample (e.g. Fig. 4.1). Additionally, models with larger aperture fractures are faster to run, since the average element size is larger.

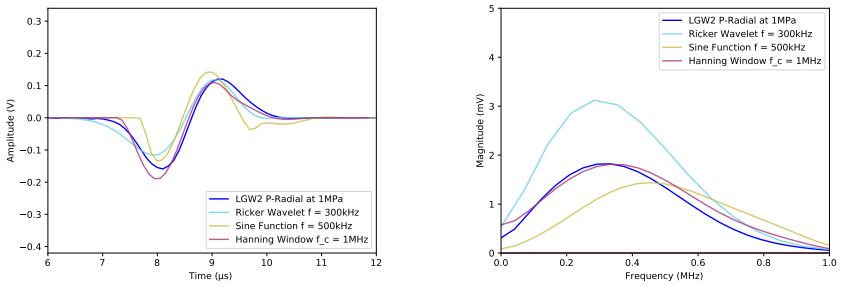

(a) (b)

Figure 6.6: Comparison of tapered traces recorded using the three functions in Fig. 6.5 as source functions, in the (a) time domain and (b) frequency domain. The Hanning window source model (purple) shows the best fit with the lab data (blue).

6.3 Parameter Study

Once a reasonable fit to the laboratory data was achieved, I conducted a parameter study to investigate the effect of fracture aperture, angle, roughness and material infill on the wave propagation across the sample. I varied one parameter at a time while keeping the others constant (Table 6.2). The fracture was oriented normal to the wave propagation, except for when the incidence angle was varied. For each model result where wave propagation was normal to the fracture I estimated the fracture stiffness using equation 2.5.

I placed additional focus on varying the fracture infill material and distribution, using the materials in Table 6.3 and the distributions shown in Fig. 6.7. The three different infill distributions each cover 50% of the fracture area with solid calcite and 50% of the area with liquid brine. I selected these infill distributions to reflect conditions similar to those observed in the samples (Fig. 1.3) and other natural fractures in the Little Grand Wash Fault area (section 1.2).

Table 6.2: Overview of fracture parameters varied for the parameter study. Fracture angles were measured from the x-axis.

Parameter	Modelled Runs						
Fracture Aperture (mm)	0.22	0.44	0.66	0.88	1.10		
Fracture Roughness, JRC	0	9	18				
Fracture Angle (°)	0	10	20	30	45	67.5	90

Table 6.3: Density and seismic velocities of different materials used for the fracture infill. Values for calcite and pyrite are from Sowers and Boyd (2019).

Material	Density (kg/m^3)	P-wave Velocity (m/s)	S-wave Velocity (m/s)
Brine	1024	1470	0
Liquid CO_2	700	500	0
Solid Calcite	2700	6500	3400
Solid Pyrite	5000	7500	4750

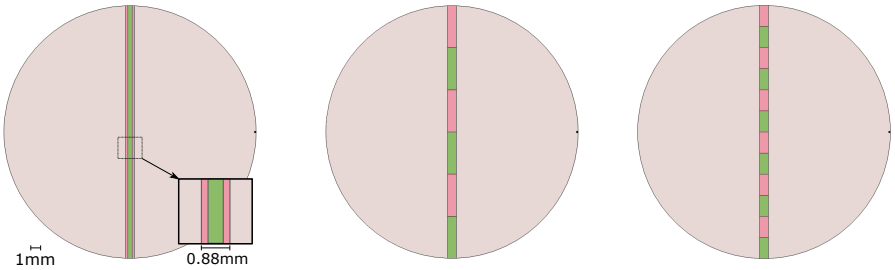

Figure 6.7: Different mineral distributions used in the parameter study. Pink indicates solid calcite and green indicates liquid brine with properties given in Table 6.3. (Left) Linings, (Center) Wide Bridges and (Right) Narrow Bridges.

Creating Rough Fractures

To investigate roughness, I wrote a script to generate random fracture profiles and estimate their Z_2 and JRC values using equations. 2.2 and 2.3 (Fig 6.8). For the parameter study I used JRC values of 0, 9 and 18 to cover the lower (0 - 2), middle (8 - 10) and higher (18 - 20) sections of the roughness profiles by Barton and Choubey (1977). Recall that the average JRC of fractures in the log of CO2W55 is 8 - 9 (section 1.2).

I added the fractures to the model geometry and scaled them down to the core sample diameter at a scale of 1:3.9 (e.g. Fig. 6.4b). The fractures are positioned such that the spatial correlation of the fracture walls is 1 with zero offset. The aperture normal to the fracture plane is constant (0.88 mm) and there are no contact points.

The area of the fracture domain is the same for all rough fracture models. The perimeter however, does change, and the total perimeter of each fracture domain is given in Table 6.4.

Table 6.4: Measured total perimeter of fracture domains for generated rough fractures, including the core sample wall boundaries.

Joint Roughness Coefficient	Perimeter (cm)
0	5.27
9	5.35
18	6.03

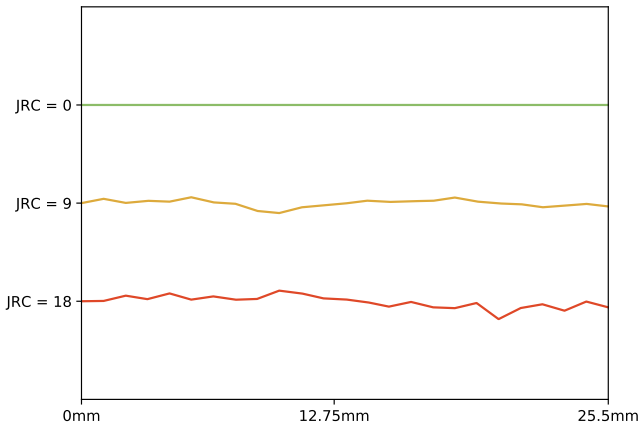

Figure 6.8: Generated fracture profiles used in the parameter study to investigate how fracture roughness affects wave propagation across the sample.

For any non-zero JRC value, there are many profiles that can have the same JRC. So, I decided to run extra models using different profiles that have the same JRC value (18) to see how the results varied (Fig. 6.9).

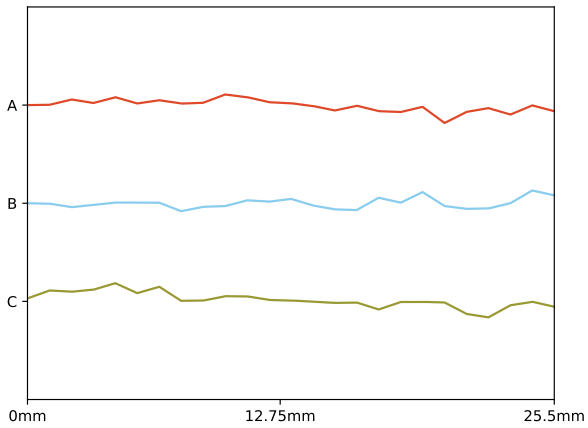

Figure 6.9: Three generated fracture profiles of JRC = 18 used to test how results vary for different fractures of the same roughness. Note fracture A is the same as JRC = 18 in Fig. 6.8.

CHAPTER 7

Modelling Results

7.1 Model Calibration

The best model-data fit was achieved with a parallel plate fracture model at an angle of 20° and with an aperture of 0.88 mm (Fig. 7.1). Note that the model results were shifted 0.4 μs to the right to better match the lab data. This was necessary as the model velocities (Table 6.1) are higher than those measured for LGW7 and LGW8 (Figs. 4.1 and 4.2). From Fig. 7.1b, the transmission coefficient of LGW7 at 1 MPa is 0.13, whereas the transmission coefficient of the modelled fracture is 0.26. The central frequencies of the model traces are also 0.02 MHz higher than the lab data.

7.2 Varying Fracture Parameters

Fracture Aperture, Roughness and Angle

Increasing the fracture aperture led to linear decreases in P-wave velocity and non-linear decreases in arrival amplitude/transmission coefficient (Table 7.1 and Fig. 7.2). The central frequency of the first arrival decreased between fracture apertures of 0.22 and 0.88 mm, but the model with an aperture of 1.10 mm does not fit this trend (Fig. 7.2b).

Increasing the JRC of the fracture from 0 to 9 decreased the first arrival amplitude by approximately 10%, but increasing the JRC further to 18 did not further decrease the arrival amplitude (Fig. 7.3). The results show no discernible effect of roughness on arrival time or frequency. Additional modelling revealed that, for different fractures with the same JRC of 18, the standard deviation of the transmission coefficient was 0.001, equivalent to variations in dynamic stiffness of 20 MPa/mm (Fig. A.8 in Appendix A).

The dynamic fracture stiffness for the different models vary between 4200 and 10800 MPa/mm (Table 7.1), which are 4-10x higher than estimated for the thick fracture sample LGW7 (Fig. 4.10).

For different fracture angles, the largest arrival amplitude was recorded when the fracture was parallel to wave propagation (fracture angle = 0°) (Figs. 7.4 and 7.5). Between 0° and 20° the arrival amplitudes decreased, then above 20° the arrival amplitudes increased again. Also, first arrivals for higher angle models (>45°) arrived slightly earlier (7.5a).

Note that a delay (T_0) of 0.68μs (Table 3.1) was added to all model traces to make the arrival times directly comparable with the laboratory test results.

Table 7.1: P-wave velocity and dynamic fracture stiffness for varying aperture models (smooth, 90° to wave propagation) and varying roughness (apertures of 0.88 mm, 90° to wave propagation). See also Figs. 7.2 and 7.3.

Aperture (mm)	P-wave velocity (m/s)	Dynamic fracture stiffness (MPa/mm)
0.22	3980	10800
0.44	3920	6900
0.66	3860	5400
0.88	3800	4800
1.10	3750	4600
Roughness, JRC		
0	3800	4800
9	3800	4200
18	3800	4200

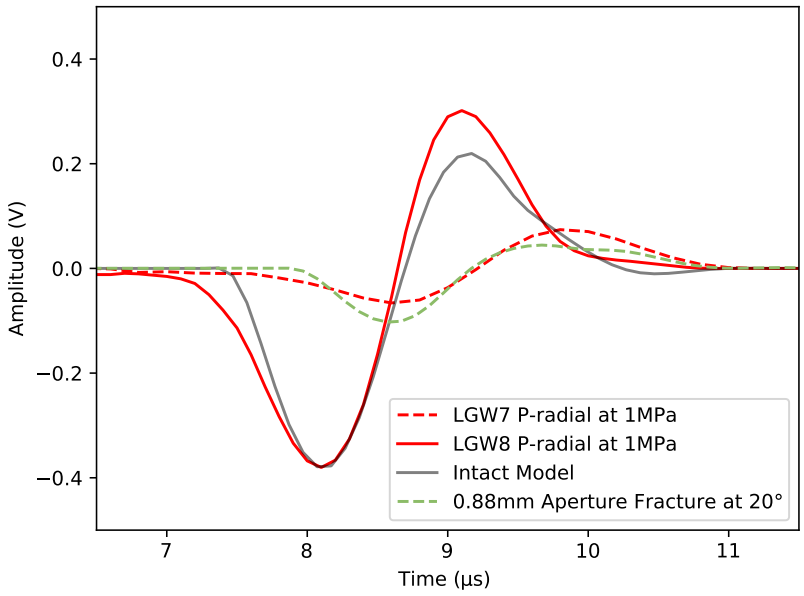

(a)

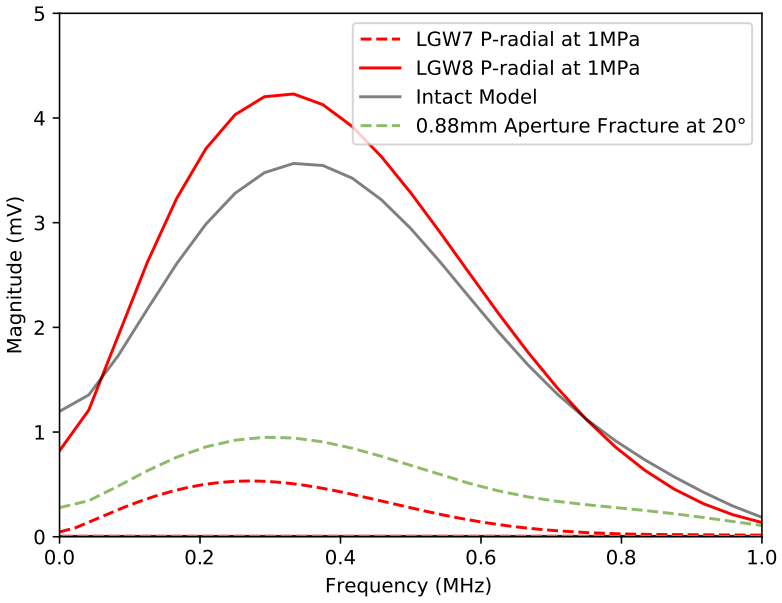

(b)

Figure 7.1: Calibration of the model against LGW7 and LGW8 P-radial data. The fracture in this model was filled with brine. (a) **Tapered** traces in the time domain. (b) FFT of the traces in (a). Note that the model results in (a) are shifted $0.4\mu s$ to the right.

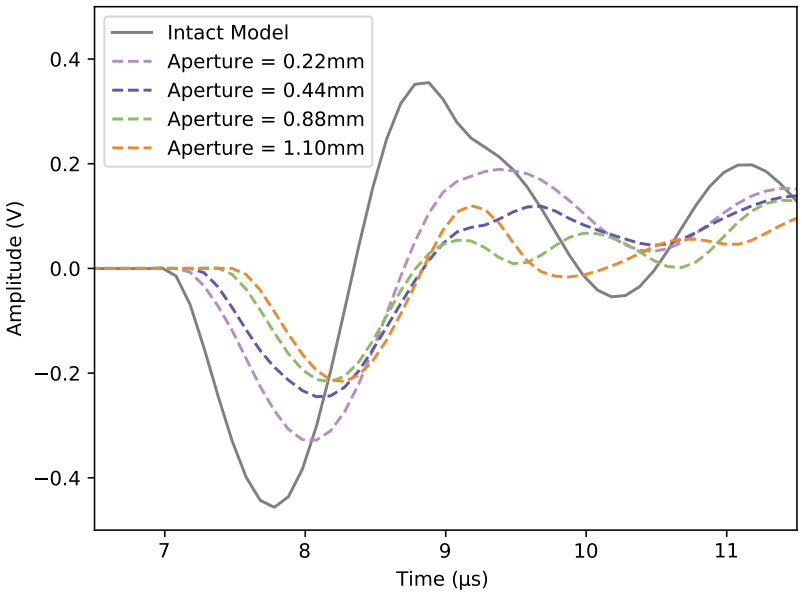

(a)

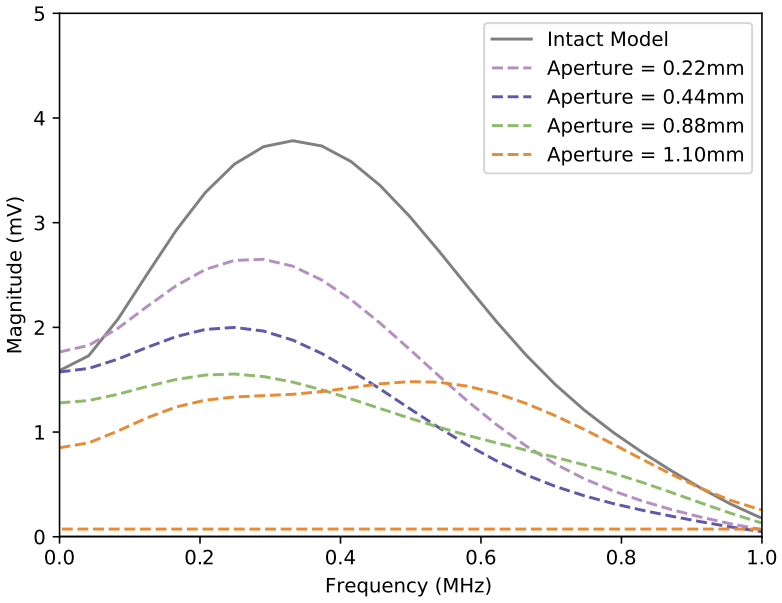

(b)

Figure 7.2: Summary of modelling results for different fracture apertures. (a) Untapered traces in the time domain. (b) FFT of the traces in (a) (**tapered**). Fractures were smooth, filled with brine and oriented normal to the wave propagation.

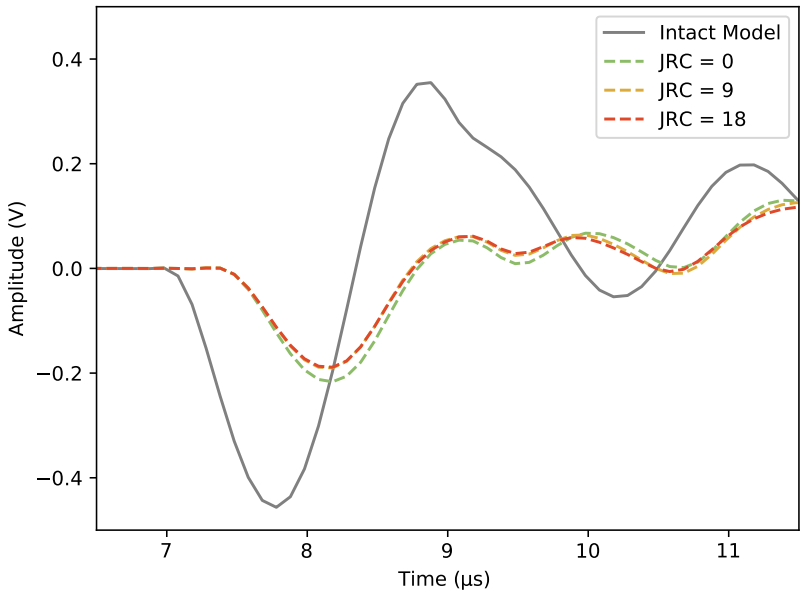

(a)

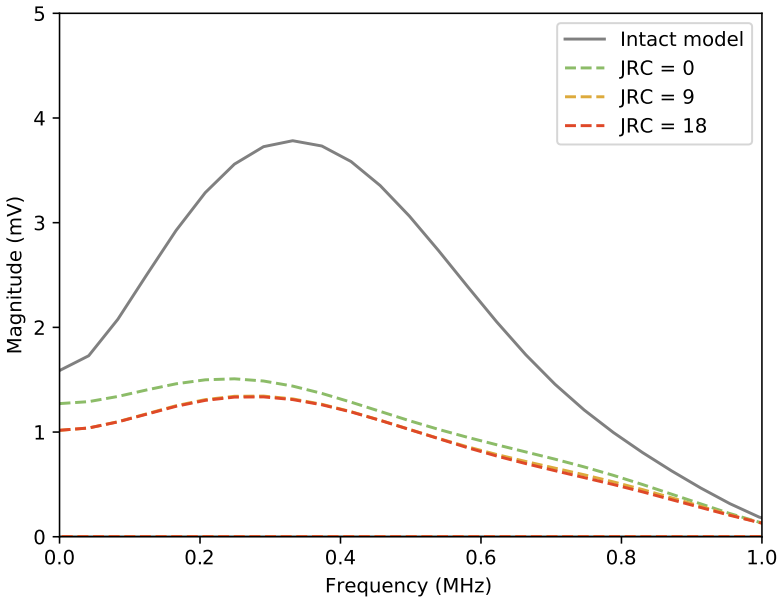

(b)

Figure 7.3: Summary of modelling results for different fracture roughnesses (See also Fig. 6.8). (a) Untapered traces in the time domain. (b) FFT of the traces in (a) (**tapered**). Fractures had apertures of 0.88 mm, were filled with brine and were oriented normal to the wave propagation.

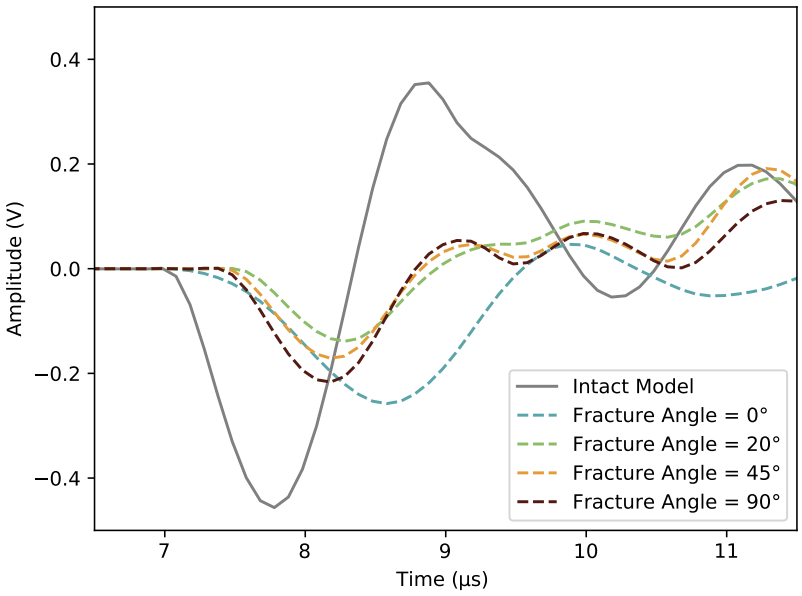

(a)

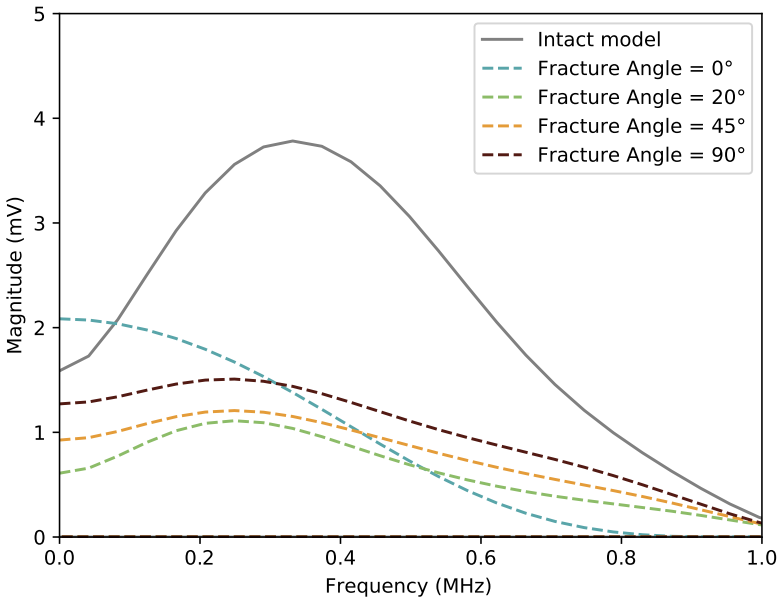

(b)

Figure 7.4: Summary of modelling results for different incidence angles. (a) Untapered traces in the time domain. (b) FFT of the traces in (a) (**tapered**). Fractures had apertures of 0.88 mm, were smooth and filled with brine.

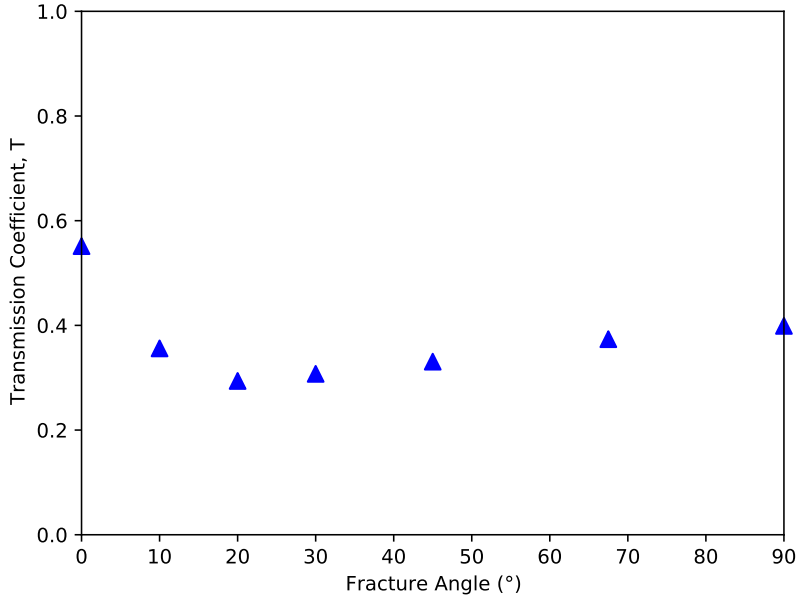

Figure 7.5: Transmission coefficient for models with different fracture angles. Transmission coefficient was calculated using equation 2.11.

Infill Material and Distribution

The results from modelling with different infill materials show a wide range of P-wave velocities and fracture stiffnesses (Fig. 7.6 and Table 7.2). The largest drop in P-wave velocity (-800 m/s) and the lowest fracture stiffness was observed when the fracture was filled with liquid CO_2. Conversely, fractures filled with solid, dense minerals (calcite and pyrite) caused the P-wave to arrive earlier than the intact model and with a comparable amplitude. The fracture with the highest dynamic specific stiffness estimate is the calcite filled fracture, at 44000 MPa/mm (Table 7.2).

P-wave velocities measured across fractures partially filled with calcite were both slower and faster than the intact reference, depending on how the calcite was distributed (Fig. 7.7 and Table 7.2). The models with mineral bridges have faster P-wave velocity measurements than the model with mineral lining. The results also show significant variations in dynamic fracture stiffness, with the narrow bridge model showing the highest stiffness at 11,000 MPa/mm (Table 7.2). The infill distribution also affects frequency distribution of the transmitted signal, with the trace of the wide mineral bridge model showing a higher central frequency (Fig. 7.7b).

Table 7.2: P-wave velocity and dynamic fracture stiffness for models including a fracture with different infill materials and distributions (Table 6.3 and Fig. 6.7). Recall that the P-wave velocity of the core material in the models is 4000 m/s.

Infill material	P-wave velocity (m/s)	Dynamic fracture stiffness (MPa/mm)
100% Brine	3800	4800
100% Liquid CO_2	3200	1600
100% Solid Calcite	4100	44000
100% Solid Pyrite	4100	21000
50% Brine, 50% Calcite (Lining)	3900	7000
50% Brine, 50% Calcite (Wide Bridges)	4100	8500
50% Brine, 50% Calcite (Narrow Bridges)	4100	11000

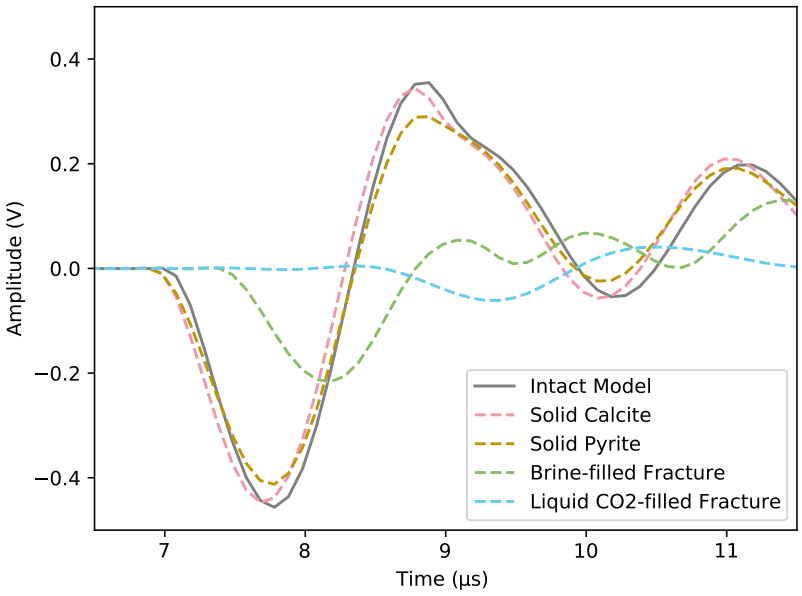

(a)

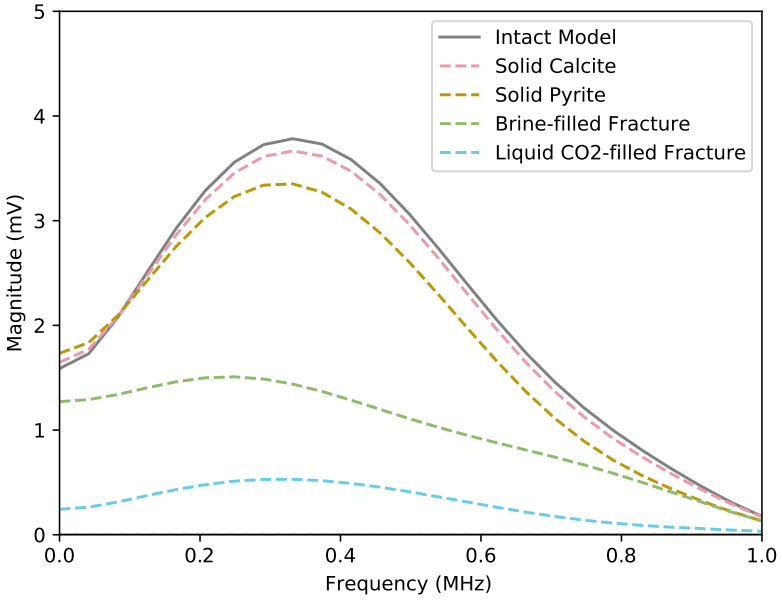

(b)

Figure 7.6: Summary of modelling results for different fracture infill materials (Table 6.3). (a) Untapered traces in the time domain. (b) FFT of the traces in (a) (**tapered**). Fractures were smooth with apertures of 0.88 mm and oriented normal to the wave propagation.

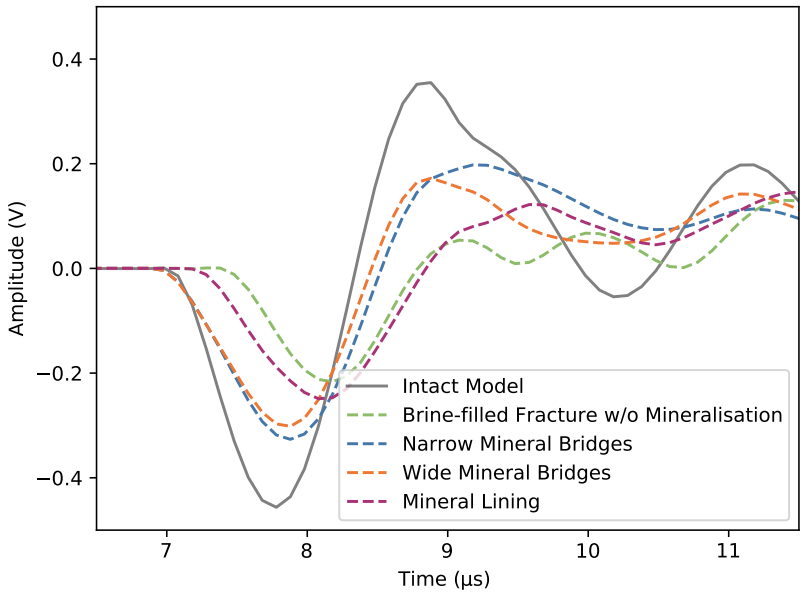

(a)

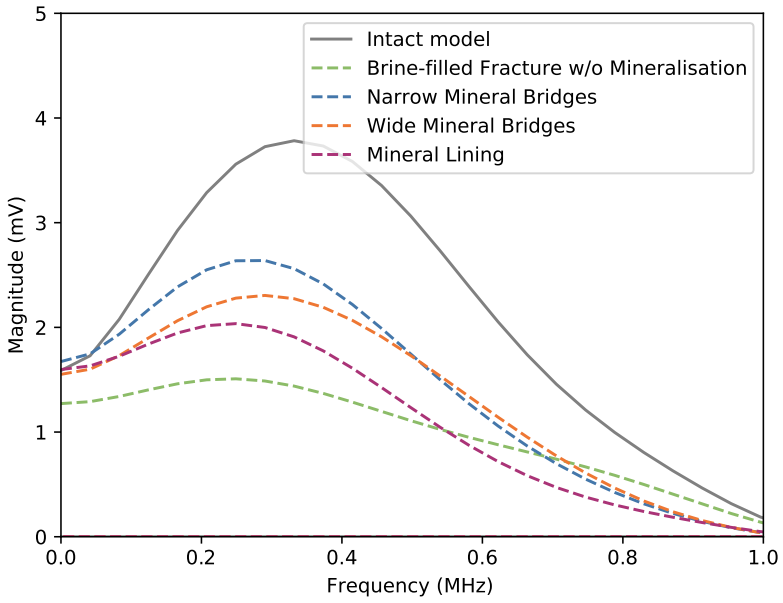

(b)

Figure 7.7: Summary of modelling results for different fracture infill distributions as shown in Fig. 6.7. (a) Untapered traces in the time domain. (b) FFT of the traces in (a) (**tapered**). Fractures were smooth with apertures of 0.88 mm and oriented normal to the wave propagation. The brine-filled fracture without mineralisation (green) is included for reference.

CHAPTER 8

Modelling Discussion

8.1 Interpretation/Discussion of Modelling Results

Aperture

The clearest result from the parameter study is that increasing the fracture aperture led to linear decreases in P-wave velocity (Fig. 7.2 and Table 7.1). Since in these models, the fracture is filled with a slower velocity material (brine), the larger the contribution of the fracture to the total raypath, the slower the average velocity will be. This result, that larger aperture fractures lead to slower velocities, matches those observed in the experimental section (Fig. 4.1a) as well as in other studies (Pan et al., 2017; Yang et al., 2019).

The results of the numerical models also indicate that increasing the fracture aperture led to a non-linear decrease in arrival amplitudes/transmission coefficients (Table 7.1, also Fig. 8.1). This finding is consistent with the theory of thin-layer interface models (Li et al., 2013), as well as experimental results (Wu et al., 2014; Pan et al., 2017; Yang et al., 2019).

The dynamic estimate of fracture stiffness of the 0.22 mm aperture model is in good agreement with equation 2.6 (Fig. 8.1; Wu et al., 2005). With increasing aperture, the dynamic estimates from the models diverge from estimates using equation 2.6 and are systematically larger.

In agreement with theory and experimental studies, the central frequency of the transmitted wave decreased between the models with apertures of 0.22 mm and 0.88 mm (Pyrak-Nolte et al., 1990; Li et al., 2013; Yang et al., 2019). The model with a fracture aperture of 1.10 mm shows an anomalously high central frequency, which could be due to the higher frequency components that were not removed by the taper (See Fig. 7.2a, 9 - 10 μs).

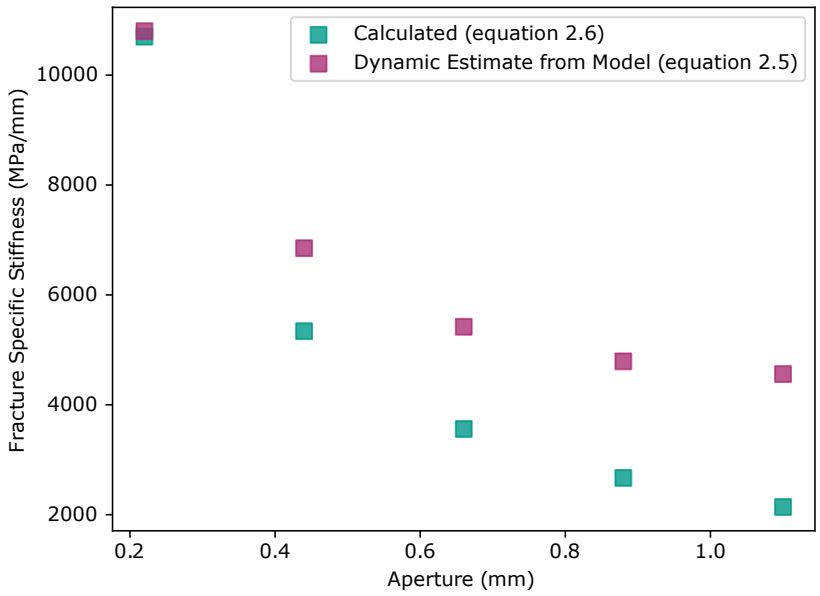

Figure 8.1: Comparison of fracture specific stiffness against aperture 1) calculated/predicted using equation 2.6 and 2) estimated from the model results using equation 2.5 (purple).

Roughness

The modelling results suggest that the roughness of the fracture boundaries has a minor effect on first arrival amplitudes (Fig. 7.3). This could be explained by scattering of the wave at the rougher fracture boundaries, causing less energy to arrive at the receiver edge.

Interestingly, increasing the JRC from 9 to 18 did not further decrease the arrival amplitude. This may be related to the limited view of the fracture by the propagating waves (Fig. 8.2). Acosta-Colon et al. (2009) showed experimentally that estimates of fracture stiffness are limited by the source-receiver configuration, and small-scale measurements may not capture scattering losses outside of the field of view. Looking at the models, the JRC = 18 model does include shorter wavelength, higher magnitude variations that make the fracture boundaries rougher, but these may not have been sampled by the first arriving wave (Fig. 8.2). The sections of the fractures in the centre of the sample (in the blue area), which affect the first arrival, look similarly rough for the JRC = 9 and JRC = 18 models.

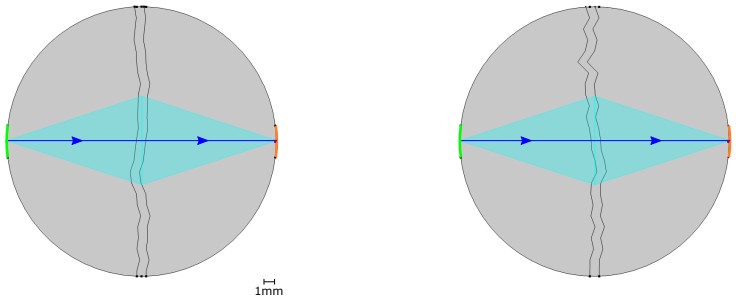

(a) (b)

Figure 8.2: Rough fracture models a) JRC = 9 and b) JRC = 18. The cyan diamond highlights the area to which the central raypath may be sensitive.

In their study of the hydromechanical behaviour of single fractures, Kewel (2020) tested three artificial fractures with different roughnesses created by hand grinding the fracture surfaces with abrasive powder of different ratings. They found that rougher fractures showed lower static stiffnesses, but any change in velocity or amplitude was too small to resolve from their ultrasonic data (Kewel, 2020). These experimental results seem to be consistent with the modelling results of this study, suggesting that fracture roughness does affect stiffness but differences may be difficult to identify in ultrasonic measurements.

Fracture Angle

Changing the fracture angle resulted in non-linear changes in transmission coefficient and minor changes in arrival time (Figs. 7.4 and 7.5). First, it is important to note that the model with a fracture angle of 0° (parallel to wave propagation) is a special case. Since the diameter of the source (3 mm) is larger than the fracture aperture (0.88 mm), some waves travelled purely through the core material and did not interact with the fracture. This resulted in a large

displacement recorded by the receiver with zero time delay relative to the intact sample. Thus for this for this data point, the term 'transmission coefficient' is misleading, since no energy was propagated across the fracture.

With increasing fracture angle, there are two competing effects that combine to create the non-linear changes in transmission coefficient (Fig. 7.5). First, increasing the fracture angle increases the projected length of the fracture along the y-axis, c, as:

$$c = d \sin \theta \tag{8.1}$$

where d is the sample diameter (25.5 mm) and θ is the fracture angle measured from the x axis.

The ratio of fracture length (c) to wavelength (λ) is critical for understanding how the fracture affects wave propagation (Fig. 8.3). When $c < \lambda$, the model appears homogeneous, whereas when $c > \lambda$, the fracture begins to act as a scattering front (Falcon-Suarez et al., 2020). The wavelength of P-waves in the model (λ) is approximately 11 mm (4000[m/s]/350[kHz]). From 0° to 20°, the transmission coefficient decreases as c approaches λ and more energy is reflected by the fracture. Above 20°, c is larger than λ and the wave may not be sensitive to increasing fracture length due to the limited field of vision mentioned in the previous section (Acosta-Colon et al., 2009).

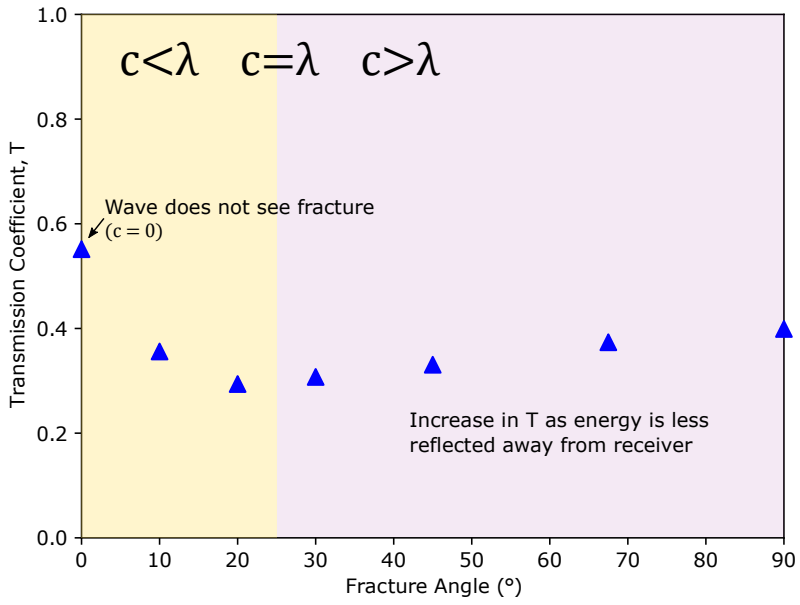

Figure 8.3: Interpretation of transmission coefficient for models with different fracture angles, highlighting how the ratio c/λ is important. Transmission coefficient was calculated using equation 2.11.

The second effect is to consider is that rays are reflected away from the receiver as they travel through the fracture domain (Figs. 8.4b and 8.5a, also Fig. 2.5 in section 2.3). As the fracture angle increases, rays spend less time in the fracture domain and are less reflected away from the receiver. This could explain the gradual increase in transmission coefficient between fracture angles of 20° and 90°, as well as why P-waves in higher fracture angle models arrive marginally earlier.

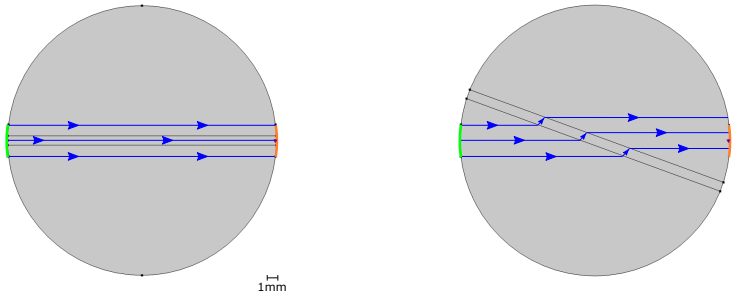

(a) (b)

Figure 8.4: Raypaths indicating P-wave propagation across fractures at angles of a) 0° and b) 20°. Rays were drawn from the edges and centre of the source edge using Snell's law (equation 2.8).

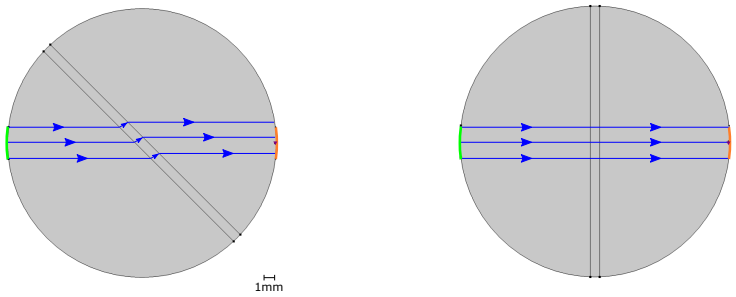

(a) (b)

Figure 8.5: Raypaths indicating P-wave propagation across fractures at angles of a) 45° and b) 90°. Rays were drawn from the edges and centre of the source edge using Snell's law (equation 2.8).

Infill Material and Distribution

Changing the infill material of the fracture was shown to increase or decrease the estimated P-wave velocity depending upon if the infill material has a higher or lower P-wave velocity than the core sample material (Fig. 7.6 and Table 7.2). This is an intuitive result, since velocity estimates are a kind of average of the material velocities covered by the raypath, and is consistent with observations of core samples with filled fractures (e.g. Allen et al., 2017; Rempe et al., 2018; Durán et al., 2019).

In the modelling results, the P-waves across the calcite and pyrite filled fractures arrive at the same time, even though P-waves in pyrite are 1000 m/s faster than calcite (Table 6.3). This is since the arrival time difference between the two traces is only 0.02 μs, which is less than the sampling rate of 0.1 μs. One could expect that on a larger scale with many filled fractures, the cumulative arrival time difference due to different fracture infill materials could be resolvable.

Another interesting finding is that the pyrite fracture model has a smaller arrival amplitude than the calcite fracture model (Fig. 7.6 and Table 7.2). This could be due to the larger seismic impedance contrast between pyrite and the core material, causing more energy to be reflected at the fracture boundary. The smaller transmission coefficient of the pyrite model leads to a smaller dynamic estimate of fracture stiffness, even though pyrite is a stiffer mineral than calcite (Sowers and Boyd, 2019). In general, therefore, it seems that dynamic estimates of fracture stiffness should be approached with caution and interpreted together with estimates of P-wave velocity.

The modelling results suggest that the distribution of mineralisation within partially filled fractures affects the arrival time, amplitude and frequency of transmitted P-waves (Fig. 7.7 and Table 7.2). From another point of view, these models are investigating how the amount and distribution of fracture contact area affects wave propagation. The P-waves in models with contact points (wide and narrow bridges) arrive faster and with larger amplitudes than the model without any contact points (lining). This is since rays travelling across the calcite bridges are unaffected by the brine, whereas in the lining model all rays must travel through the brine. Previous studies have identified the link between higher contact areas and stiffnesses (e.g. Goodman, 1976; Brown and Scholz, 1985; Cook, 1992), leading to higher transmission coefficients. Indeed, this behaviour is also seen in the experimental section of this study as the contact area, fracture stiffnesses and transmission coefficients increased under stress.

Furthermore, the modelling results indicate that, for the same contact area ratio, having narrow contact points distributed along the fracture leads to a higher fracture stiffness than having fewer, wide contact points. This finding is supported by analytical (Hopkins et al., 1987) and numerical models (Rubino et al., 2014).

The results discussed in this section have important implications for relating the seismic response of a fracture to its permeability. In general, the presence of dense minerals in the fracture and or contact points between the fracture surfaces led to higher P-wave velocities and stiffnesses.

8.2 Modelling Assumptions and Limitations

The main known assumptions and limitations of the numerical models in this study are as follows:

- The model is a 2D representation of a 3D system. As a result, the model does not capture the heterogeneous and anisotropic nature of the samples that affect the wave propagation. Additionally, the waveform is a 2D cylindrical wave rather than a 3D spherical wave.
- All fracture geometries are simplified representations of natural, complex fractures.
- The model does not consider the sample porosity or any related effects such as wave induced fluid flow (e.g. Müller et al., 2010). The core material is modelled as a purely elastic, rather than a poroelastic, material.
- The model domains do not include any internal damping (intrinsic attenuation).
- The piezoelectric transducers are reduced to 2D lines along the edge of the core sample wall. Any interactions of the wave with the transducers, such as reflections, are not considered.
- A general observation with using the Hanning window as a source function is that the modelled arrivals are sharper than the lab data (e.g. see Fig. 7.1a between 7 and 8 μs, also Fig. 6.6a). This could be related to attenuation within the samples.

Other, minor assumptions include:

- To simplify the source function equation, the source was approximated to act purely in the x direction. The effect of this is assumed to be small since the curvature of the source edge in the model (Fig. 6.1).
- The displacement recorded by the receiver edge was approximated by the displacement recorded at the receiver point to simplify post processing of results (Fig. 6.1a). Though later arrivals showed small variations, the first arrivals measured by the edge and the point were visually indistinguishable (Fig. A.9 in Appendix A).

PART III

Joint Discussion and Conclusions

CHAPTER 9

Joint Discussion

9.1 Joint Discussion

Overall, the results of the numerical modelling support the experimental results. In particular that LGW7, the sample with a rougher, wider fracture and less contact area had larger decreases in P-wave velocity and arrival amplitudes. Though, sample LGW7 also had a higher percentage of dense mineral precipitates (Table 1.2), which the parameter study linked to higher velocities and amplitudes. This highlights a core challenge in relating seismic measurements to fracture characteristics: natural fractures are complex and their characteristics are interrelated. For this reason, fracture specific stiffness remains an attractive parameter as it can combine these characteristics into a single quantitative value.

However, the parameter study also highlighted a nonuniqueness problem, in that a change in velocity, amplitude or frequency can be due to variations in several different fracture characteristics. This problem can be reduced if changes in velocity, amplitude and frequency are considered together. An example given by NRC (1996) discussed ultrasonic data from core samples taken in a hydraulically active shear zone. The matrix rock close to the shear zone had higher a velocity than the surrounding area, possibly due to mineralisation, but open fractures delayed the seismic waves and the net result was a weak velocity anomaly. Furthemore, the fractures attenuated the seismic signal so the overall seismic response of the hydraulically active shear zone was a weak velocity anomaly coupled with a high attenuation anomaly (NRC, 1996, p.506). If only velocity or attenuation had been considered individually, this zone may have been mischaracterised.

The results of this study have shown that seismic measurements can, at least qualitatively, be related to fracture permeability. In particular, smaller aperture, less permeable fractures show higher fracture stiffnesses and smaller velocity anomalies relative to intact samples. The amount of and distribution of contact areas, which affects fluid flow, was also shown to affect seismic measurements. The definition of a quantitative relationship between seismic measurements and fracture permeability was beyond the scope of this study, and I refer the interested reader to Pyrak-Nolte and Morris (2000) and Pyrak-Nolte and Nolte (2016). In brief, it may be challenging to quantitatively relate seismic measurements to fracture permeabilities since seismic velocities depend on

the mean aperture, whereas permeability is often controlled by the narrowest aperture (Rempe et al., 2018). Furthermore, since the relationship between the fracture geometry, infill properties and stiffness is nonunique, so is the relationship between (dynamic) stiffness and permeability (NRC, 1996, p.138). Nevertheless, even empirical relationships between these two parameters could be of great practical value.

The modelling results suggested that the transmission coefficient T varies with fracture angle, with a minimum around 20° (Fig. 7.5). Thus, the dynamic stiffness estimates of LGW7 could be viewed as minimum estimates since the fracture was at a 20° angle to wave propagation (Fig. 4.10). However, since natural fractures are more complex, it can be expected that variations in T with fracture angle may not be as clear as the trend from the modelling results.

Tapering First Arrivals

The aim of both the experimental and numerical experiments was to improve understanding of how waves propagate through the fractured samples. Since the signal wavelength is on the same scale as the sample dimensions (approx. 2 - 5λ), reflections from the sample boundaries need to be considered (Zou et al., 2016). According to Yoshimitsu et al. (2016), the later part of the first arrival may be superimposed with reflected and converted P- and S-waves propagating in both horizontal and vertical directions.

In order to isolate the first arrival, it is standard procedure to apply a taper to a selected window of the full trace (e.g. Fig. 3.6; Pyrak-Nolte et al., 1990; Yang et al., 2019; Lai et al., 2020). However, when a Fourier transform is then applied to the tapered window, the estimated spectrum can be contaminated by the Fourier transform of the window length (Mavko et al., 2009, p.5). In particular, Mavko et al. (2009) mention that this can have a large effect on ultrasonic waveforms, where only the first cycle is included in the window.

In this study, I tested out tapers of different shapes and window lengths before deciding to use a half-cosine taper of 4 μs (Fig. 3.6). For the results to be comparable, the same taper must be applied to all traces, even though there were cases where it looked like a different taper may have yielded better results (e.g. Fig. 7.2, aperture = 1.10 mm). A more detailed investigation on the effect of different tapers and possible use of information from later arrivals was beyond the scope of this study.

9.2 Applicability to Field Studies

The results of this study, namely a better understanding of the relationships between fracture geometry, infill material, seismic measurements and permeability, has several possible applications.

First, ultrasonic measurements of core samples can be integrated as part of a larger study to reveal large scale trends. For example, Allen et al. (2017) correlated lower permeability and velocity measurements in the damage zone of the Alpine Fault, New Zealand to gouge and calcite-filled fractures. As another example, Rempe et al. (2018) analysed samples across the Gole Larghe Fault

Zone in the Italian alps and found that velocity and permeability measurements correlated with microfracture intensity, except in the fluid-alteration zone, where high P-wave velocities were attributed to microfractures sealed with epidote. Similarly, the results of this study could be used to support interpretations of seismic data across the Little Grand Wash Fault. For example, high velocity anomalies may be due to sealing of fractures by mineral precipitates and low velocity anomalies may be attributed to open, hydraulically active fractures. Additional information on the first arrival amplitudes may help to distinguish between hydraulically active and inactive areas.

Second, since seismic measurements are sensitive to the state of fractures, active or passive time-lapse methods may be used to monitor changes in fracture networks. In particular, applications involving large volumes of fluids and changes in pressure conditions, such as the storage of CO_2, require continuous monitoring to ensure safe operation (Harbert et al., 2016). As a field scale example, Loriaux et al. (2021) conducted seismic refraction surveys on a wave-cut platform at low and high tide to investigate how the change in fracture infill conditions affect seismic measurements. They measured changes in seismic velocities and stiffness that could be attributed to the drainage of seawater from the main fracture set. Field studies such as this are useful for understanding how laboratory results may be upscaled, yet further work is required to go from the outcrop to reservoir scale (Loriaux et al., 2021).

Finally, the results of this study could possibly be related to characterisation of fractures in boreholes using sonic (acoustic) logs. The source-receiver configuration and signal frequencies may be different, but sonic logging measurements are also made on the scale at which fractures may be large compared to the wavelength (e.g. Paillet et al., 1980; Sun et al., 2000; Bakku et al., 2013). For example, Pan et al. (2017) derived an empirical relationship between fracture width and the amplitude attenuation ratio of P- and S-waves from ultrasonic data on core samples, then applied this to sonic logs to estimate fracture widths which were supported by electrical imaging logs. Furthermore, Barbosa et al. (2019) showed that it is possible to calculate the transmission coefficient, T, and thus estimate the stiffness, of individual fractures in sonic log data. Their results were supported by optical televiewer logs and numerical simulations to consider geometrical spreading and oblique incidence angles (Barbosa et al., 2019). Boreholes are valuable for obtaining in-situ observations of fractures at depth and calibrating/validating near-surface measurements. Furthermore, the identification and characterisation of fractures in sonic logs can be supported by other well logs (e.g. NRC, 1996, p.168-171), and could be related to permeability estimates from flow measurements (e.g. Paillet, 1983; Caspari et al., 2020).

CHAPTER 10

Conclusions

10.1 Conclusions

This study has presented unique experimental results relating ultrasonic measurements, stiffness and permeability data of naturally fractured samples, as well as a calibrated numerical study investigating how different fracture characterstics affect seismic measurements. I conclude that:

1. P-waves propagating across thicker fractures with fewer contact points arrive later, with smaller amplitudes and lower central frequencies. Thicker fractures have lower stiffnesses and cause larger velocity anomalies for transmitted waves.

2. Closure of fractures under increasing stress can be most reliably identified by faster P-wave velocities. Amplitude and frequency data also showed a sensitivity to the fracture aperture, but overall trends are ambiguous.

3. Seismic measurements can be related to fracture permeability. In the experiments, faster P-wave velocities and higher stiffnesses were associated with lower permeabilities.

4. Seismic measurements are sensitive to both the fracture infill material and its distribution. Velocity anomalies can be fast or slow depending upon if the fracture infill material is stiffer than the rock matrix. Characterisation of fractures from seismic measurements should consider both velocity and stiffness estimates.

5. Rougher fracture boundaries in the models decreased the first arrival amplitude by approximately 10%, but increasing the JRC from 9 to 18 did not further decrease the amplitude.

10.2 Suggestions for Further Work

The aim of this thesis was to better understand how fracture characteristics (aperture, roughness, contact area, infill material) affect seismic wave propagation at the core sample scale. Further research into this area could involve:

1. Integration of the results with other datasets from the Little Grand Wash Fault. Results could be used directly to qualitatively support interpretations of seismic data. With further work, the results could be scaled to improve understanding of wave propagation across fracture sets, for example by field-scale simulations. Furthermore, there is great potential for seismic data to be combined with datasets from other fields such as structural geology, sedimentology and hydrogeology.

2. Experimental and or numerical work could aim to quantify changes in arrival amplitudes due to secondary consolidation and improving piezoelectric transducer-sample contact, so that changes in arrival amplitudes due to fracture closure could be more reliably interpreted. Standardization of experimental procedures with respect to loading rates and flow tests could also reduce noise in the data, particularly the amplitude data.

Appendices

APPENDIX A

Additional Figures

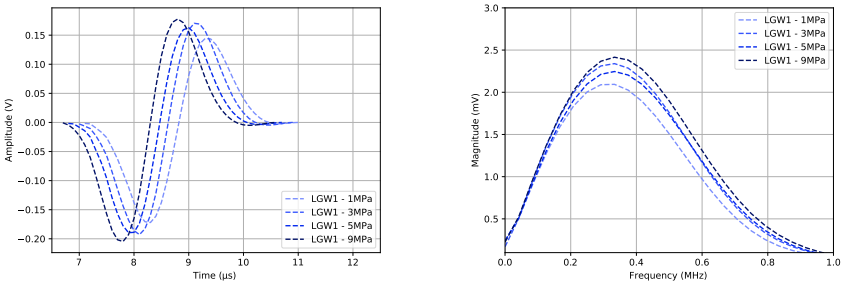

(a) (b)

Figure A.1: a) Selected P-wave arrivals (tapered) in the **radial** direction for sample LGW1 (Thin Fracture), under 1 - 9MPa isotropic stress, and b) the spectral content of a).

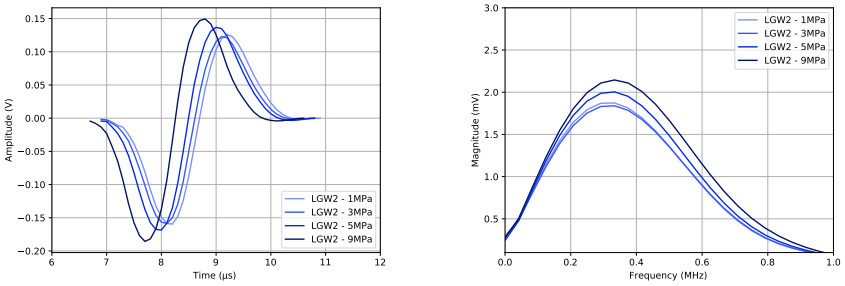

(a) (b)

Figure A.2: a) Selected P-wave arrivals (tapered) in the **radial** direction for sample LGW2 (Reference 1), under 1 - 9MPa isotropic stress, and b) the spectral content of a).

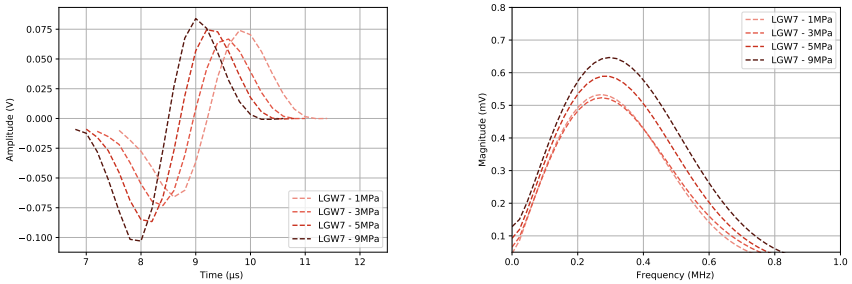

(a) (b)

Figure A.3: a) Selected P-wave arrivals (tapered) in the **radial** direction for sample LGW7 (Thick Fracture), under 1 - 9MPa isotropic stress, and b) the spectral content of a).

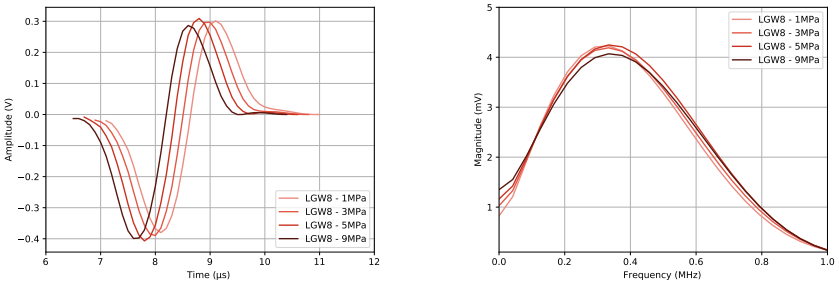

(a) (b)

Figure A.4: a) Selected P-wave arrivals (tapered) in the **radial** direction for sample LGW8 (Reference 2), under 1 - 9MPa isotropic stress, and b) the spectral content of a).

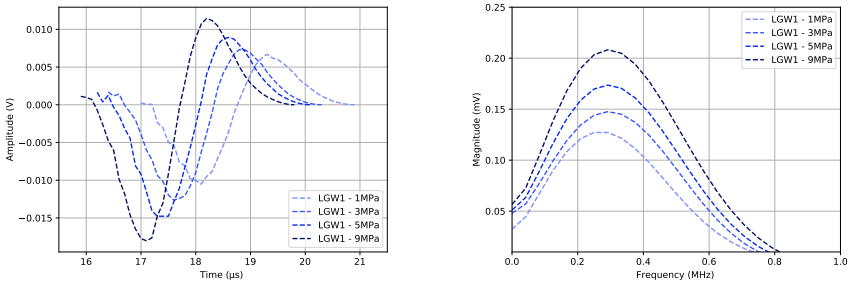

(a) (b)

Figure A.5: a) Selected P-wave arrivals (tapered) in the **axial** direction for sample LGW1 (Thin Fracture), under 1 - 9MPa isotropic stress, and b) the spectral content of a).

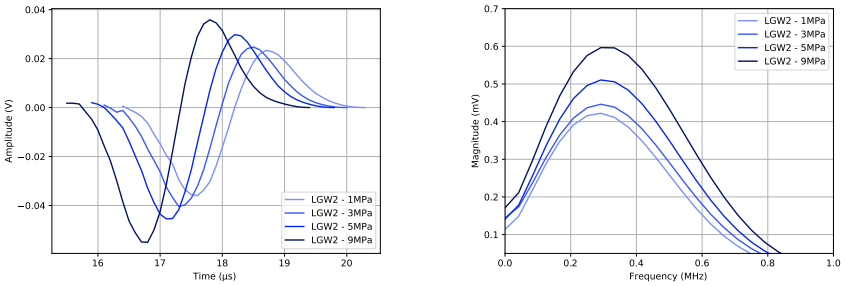

(a) (b)

Figure A.6: a) Selected P-wave arrivals (tapered) in the **axial** direction for sample LGW2 (Reference 1), under 1 - 9MPa isotropic stress, and b) the spectral content of a).

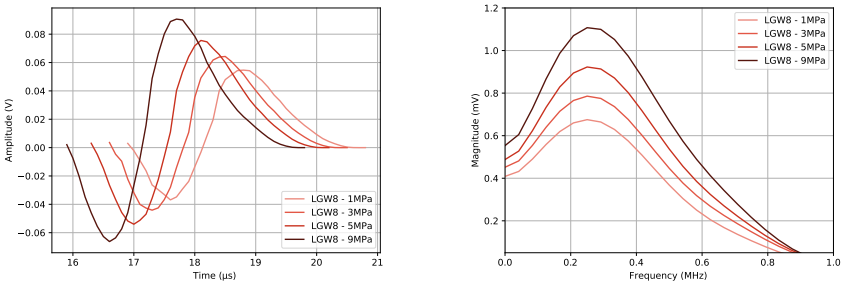

(a) (b)

Figure A.7: a) Selected P-wave arrivals (tapered) in the **axial** direction for sample LGW8 (Reference 2), under 1 - 9MPa isotropic stress, and b) the spectral content of a).

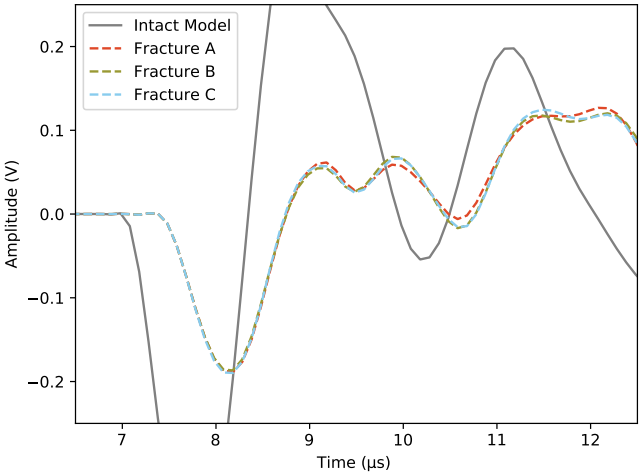

(a)

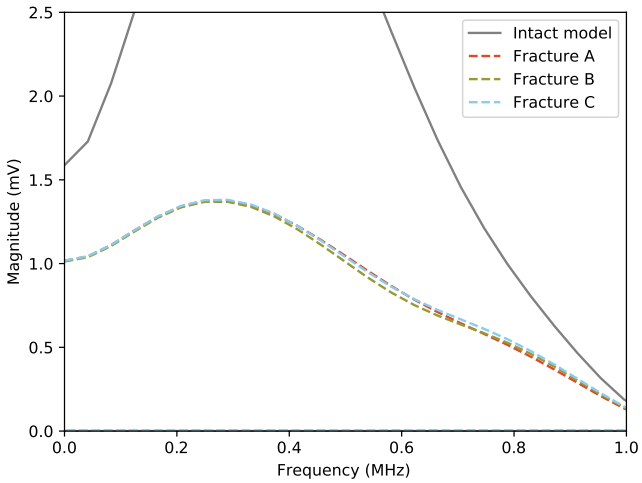

(b)

Figure A.8: Model results using three separate fractures of JRC = 18 (See Fig. 6.9) in the (a) time and (b) frequency domain. Note that the y-axes are zoomed in 2x relative to other figures to make the difference between traces more visible.

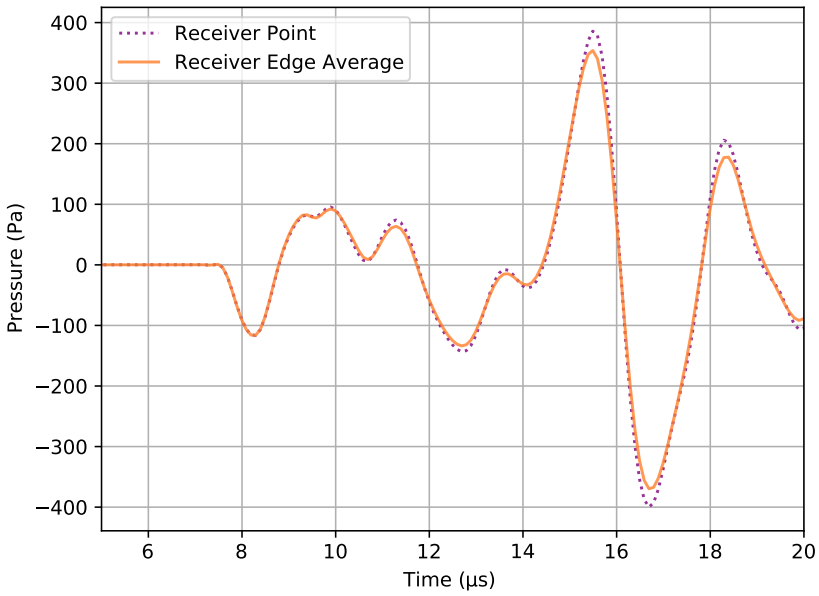

Figure A.9: A comparison of the pressure recorded at the receiver point and the receiver edge for the intact model (Fig. 6.1). I decided to use the receiver point to simplify post processing since the first arrivals are indistinguishable.

Bibliography

Abbas, M. (2015). 'Geomechanical characterization of shale caprock of the Longyearbyen CO2 storage pilot'. Master thesis. University of Oslo.

Acosta-Colon, A., Pyrak-Nolte, L. J. and Nolte, D. D. (2009). 'Laboratory-scale study of field of view and the seismic interpretation of fracture specific stiffness'. In: *Geophysical Prospecting* vol. 57, no. 2, pp. 209–224.

Allen, M., Tatham, D., Faulkner, D., Mariani, E. and Boulton, C. (2017). 'Permeability and seismic velocity and their anisotropy across the Alpine Fault, New Zealand: An insight from laboratory measurements on core from the Deep Fault Drilling Project phase 1 (DFDP-1)'. In: *Journal of Geophysical Research: Solid Earth* vol. 122, no. 8, pp. 6160–6179.

Arulnathan, R., Boulanger, R. W. and Riemer, M. F. (1998). 'Analysis of bender element tests'. In: *Geotechnical Testing Journal* vol. 21, no. 2, pp. 120–131.

Bakku, S. K., Fehler, M. and Burns, D. (2013). 'Fracture compliance estimation using borehole tube waves'. In: *Geophysics* vol. 78, no. 4, pp. D249–D260.

Banks, D., Odling, N. E., Skarphagen, H. and Rohr-Torp, E. (1996). 'Permeability and stress in crystalline rocks'. In: *Terra Nova* vol. 8, no. 3, pp. 223–235.

Barbosa, N. D., Caspari, E., Rubino, J. G., Greenwood, A., Baron, L. and Holliger, K. (2019). 'Estimation of fracture compliance from attenuation and velocity analysis of full-waveform sonic log data'. In: *Journal of Geophysical Research: Solid Earth* vol. 124, no. 3, pp. 2738–2761.

Barton, N. and Choubey, V. (1977). 'The shear strength of rock joints in theory and practice'. In: *Rock mechanics* vol. 10, no. 1, pp. 1–54.

Bense, V., Gleeson, T., Loveless, S., Bour, O. and Scibek, J. (2013). 'Fault zone hydrogeology'. In: *Earth-Science Reviews* vol. 127, pp. 171–192.

Berre, T. (2011). 'Triaxial testing of soft rocks'. In: *Geotechnical Testing Journal* vol. 34, no. 1, pp. 61–75.

Binley, A., Hubbard, S. S., Huisman, J. A., Revil, A., Robinson, D. A., Singha, K. and Slater, L. D. (2015). 'The emergence of hydrogeophysics for improved understanding of subsurface processes over multiple scales'. In: *Water resources research* vol. 51, no. 6, pp. 3837–3866.

Birch, F. (1960). 'The velocity of compressional waves in rocks to 10 kilobars: 1.' In: *Journal of Geophysical Research* vol. 65, no. 4, pp. 1083–1102.

Blewett, J., Blewett, I. and Woodward, P. (1999). 'Measurement of shear-wave velocity using phase-sensitive detection techniques'. In: *Canadian Geotechnical Journal* vol. 36, no. 5, pp. 934–939.

Boston Piezooptics (2021). *Ceramic Materials*. URL: https://www.bostonpiezooptics.com/ceramic-materials-pzt (visited on 15/03/2021).

Brown, S. R. and Scholz, C. H. (1985). 'Closure of random elastic surfaces in contact'. In: *Journal of Geophysical Research: Solid Earth* vol. 90, no. B7, pp. 5531–5545.

Caspari, E., Greenwood, A., Baron, L., Egli, D., Toschini, E., Hu, K. and Holliger, K. (2020). 'Characteristics of a fracture network surrounding a hydrothermally altered shear zone from geophysical borehole logs'. In: *Solid Earth* vol. 11, no. 3, pp. 829–854.

Choi, M.-K., Bobet, A. and Pyrak-Nolte, L. J. (2014). 'The effect of surface roughness and mixed-mode loading on the stiffness ratio κ x/κ z for fractures'. In: *Geophysics* vol. 79, no. 5, pp. D319–D331.

COMSOL (2021). *The Modeling Workflow*. URL: https://www.comsol.no/learning-center/setting-up-and-running-a-simulation-with-comsol-multiphysics (visited on 15/03/2021).

Cook, N. G. (1992). 'Natural joints in rock: mechanical, hydraulic and seismic behaviour and properties under normal stress'. In: *International Journal of Rock Mechanics and Mining Sciences & Geomechanics Abstracts*. Vol. 29. 3. Elsevier, pp. 198–223.

Day-Lewis, F. D., Slater, L. D., Robinson, J., Johnson, C. D., Terry, N. and Werkema, D. (2017). 'An overview of geophysical technologies appropriate for characterization and monitoring at fractured-rock sites'. In: *Journal of environmental management* vol. 204, pp. 709–720.

De Basabe, J. D., Sen, M. K. and Wheeler, M. F. (2016). 'Elastic wave propagation in fractured media using the discontinuous Galerkin method'. In: *Geophysics* vol. 81, no. 4, T163–T174.

Dockrill, B. and Shipton, Z. K. (2010). 'Structural controls on leakage from a natural CO2 geologic storage site: Central Utah, USA'. In: *Journal of Structural Geology* vol. 32, no. 11, pp. 1768–1782.

Doelling, H. H. (2001). *Geologic map of the Moab and eastern part of the San Rafael Desert 30'x 60' quadrangles, Grand and Emery Counties, Utah, and Mesa County, Colorado*. Utah Geological Survey.

Doelling, H. H., Kuehne, P. A., Willis, G. C. and Ehler, J. B. (2015). *Geologic map of the San Rafael Desert 30'x 60' quadrangle, Emery and Grand Counties, Utah*. Utah Geological Survey.

Durán, E. L., Adam, L., Wallis, I. C. and Barnhoorn, A. (2019). 'Mineral alteration and fracture influence on the elastic properties of volcaniclastic rocks'. In: *Journal of Geophysical Research: Solid Earth* vol. 124, no. 5, pp. 4576–4600.

Eichhubl, P., Davatz, N. C. and Becker, S. P. (2009). 'Structural and diagenetic control of fluid migration and cementation along the Moab fault, Utah'. In: *AAPG bulletin* vol. 93, no. 5, pp. 653–681.

Falcon-Suarez, I. H., Papageorgiou, G., Jin, Z., Muñoz-Ibáñez, A., Chapman, M. and Best, A. I. (2020). 'CO2-brine substitution effects on ultrasonic wave propagation through sandstone with oblique fractures'. In: *Geophysical Research Letters* vol. 47, no. 16. Article e2020GL088439.

Frery, E., Gratier, J.-P., Ellouz-Zimmerman, N., Deschamps, P., Blamart, D., Hamelin, B. and Swennen, R. (2017). 'Geochemical transect through a travertine mount: A detailed record of CO2-enriched fluid leakage from

Late Pleistocene to present-day–Little Grand Wash fault (Utah, USA)'. In: *Quaternary International* vol. 437, pp. 98–106.

Garden, I. R., Guscott, S., Burley, S., Foxford, K., Walsh, J. and Marshall, J. (2001). 'An exhumed palaeo-hydrocarbon migration fairway in a faulted carrier system, Entrada Sandstone of SE Utah, USA'. In: *Geofluids* vol. 1, no. 3, pp. 195–213.

Goodman, R. E. (1976). *Methods of geological engineering in discontinuous rocks*. West Publishing Company.

Goodman, R. E., Taylor, R. L. and Brekke, T. L. (1968). 'A model for the mechanics of jointed rock'. In: *Journal of the soil mechanics and foundations division* vol. 94, no. 3, pp. 637–659.

Google (2021). *Google Maps: Utah, USA*. URL: https://www.google.com/maps/place/Utah,+USA (visited on 24/05/2021).

Gudmundsson, A. (2011). *Rock fractures in geological processes*. Cambridge University Press.

Hakami, E. (1995). 'Aperture distribution of rock fractures'. PhD thesis. Royal Institute of Technology, Stockholm.

Han, W. S., Lu, M., McPherson, B., Keating, E., Moore, J., Park, E., Watson, Z. and Jung, N.-H. (2013). 'Characteristics of CO 2-driven cold-water geyser, C rystal G eyser in U tah: experimental observation and mechanism analyses'. In: *Geofluids* vol. 13, no. 3, pp. 283–297.

Harbert, W., Daley, T. M., Bromhal, G., Sullivan, C. and Huang, L. (2016). 'Progress in monitoring strategies for risk reduction in geologic CO2 storage'. In: *International Journal of Greenhouse Gas Control* vol. 51, pp. 260–275.

Hopkins, D. L., Cook, N. G. and Myer, L. R. (1987). 'Fracture stiffness and aperture as a function of applied stress and contact geometry'. In:

Hornby, B. E. (1998). 'Experimental laboratory determination of the dynamic elastic properties of wet, drained shales'. In: *Journal of Geophysical Research: Solid Earth* vol. 103, no. B12, pp. 29945–29964.

Hsieh, P. A. (2018). 'Fractured Rock Environments'. In: *Groundwater: State of the science and practice*. Ed. by Association, N. G. W. National Ground Water Association Press. Chap. 5, pp. 21–23.

Jung, N.-H., Han, W. S., Watson, Z., Graham, J. P. and Kim, K.-Y. (2014). 'Fault-controlled CO2 leakage from natural reservoirs in the Colorado Plateau, East-Central Utah'. In: *Earth and Planetary Science Letters* vol. 403, pp. 358–367.

Kamali-Asl, A., KC, B., Ghazanfari, E. and Hedayat, A. (2019). 'Flow-induced alterations of ultrasonic signatures and fracture aperture under constant state of stress in a single-fractured rock'. In: *Geophysics* vol. 84, no. 4, WA115–WA125.

Kampman, N., Maskell, A., Bickle, M., Evans, J., Schaller, M., Purser, G., Zhou, Z., Gattacceca, J., Peitre, E., Rochelle, C. et al. (2013). 'Scientific drilling and downhole fluid sampling of a natural CO 2 reservoir, Green River, Utah'. In: *Scientific Drilling* vol. 16, pp. 33–43.

Kewel, M. (2020). 'Experimental investigations into the hydro-mechanical properties of rocks containing fractures'. PhD thesis. Ruhr University Bochum.

Lai, S.-T., Nobuaki, F., Katayama, I., Bonilla, L. F. and Capdeville, Y. (2020). 'Time-lapse waveform analysis for elastic and anelastic structural changes of transducer-transducer active seismic experiments' data during triaxial

deformation of granitic rock'. In: *Earth and Space Science Open Archive ESSOAr*.

Lang, P. S., Paluszny, A. and Zimmerman, R. W. (2016). 'Evolution of fracture normal stiffness due to pressure dissolution and precipitation'. In: *International Journal of Rock Mechanics and Mining Sciences* vol. 88, pp. 12–22.

Laubach, S. E., Olson, J. E. and Gale, J. F. (2004). 'Are open fractures necessarily aligned with maximum horizontal stress?' In: *Earth and Planetary Science Letters* vol. 222, no. 1, pp. 191–195.

Laubach, S. E., Lander, R., Criscenti, L. J., Anovitz, L. M., Urai, J., Pollyea, R., Hooker, J. N., Narr, W., Evans, M. A., Kerisit, S. N. et al. (2019). 'The role of chemistry in fracture pattern development and opportunities to advance interpretations of geological materials'. In: *Reviews of Geophysics* vol. 57, no. 3, pp. 1065–1111.

Li, J., Li, H., Jiao, Y., Liu, Y., Xia, X. and Yu, C. (2014). 'Analysis for oblique wave propagation across filled joints based on thin-layer interface model'. In: *Journal of Applied Geophysics* vol. 102, pp. 39–46.

Li, J. C., Wu, W., Li, H., Zhu, J. and Zhao, J. (2013). 'A thin-layer interface model for wave propagation through filled rock joints'. In: *Journal of Applied Geophysics* vol. 91, pp. 31–38.

Lissa, S., Barbosa, N. D., Rubino, J. and Quintal, B. (2019). 'Seismic attenuation and dispersion in poroelastic media with fractures of variable aperture distributions'. In: *Solid Earth* vol. 10, no. 4, pp. 1321–1336.

Liu, E., Hudson, J. A. and Pointer, T. (2000). 'Equivalent medium representation of fractured rock'. In: *Journal of Geophysical Research: Solid Earth* vol. 105, no. B2, pp. 2981–3000.

Loriaux, T., Verdon, J., Kendall, J.-M., Baird, A. and Wookey, J. (2021). 'Field measurements of fracture characteristics on a wave-cut platform'. In: *Interpretation* vol. 9, no. 2, T453–T462.

Mavko, G., Mukerji, T. and Dvorkin, J. (2009). *The rock physics handbook*. 2nd ed. Cambridge University Press.

Midtkandal, I., Sundal, A., Braathen, A., Petrie, E., Evans, J., Zuchuat, V., Skurtveit, E., Tveranger, J., Torabi, A. and Gutierrez, M. (2018). 'CO2 Seal Bypass–A Multidisciplinary Approach to CO2 Migration and Storage'. In: *14th Greenhouse Gas Control Technologies Conference Melbourne*, pp. 21–26.

Myers, N. (1962). 'Characterization of surface roughness'. In: *Wear* vol. 5, no. 3, pp. 182–189.

Müller, T. M., Gurevich, B. and Lebedev, M. (2010). 'Seismic wave attenuation and dispersion resulting from wave-induced flow in porous rocks—A review'. In: *Geophysics* vol. 75, no. 5, 75A147–75A164.

Möllhoff, M., Bean, C. and Meredith, P. (2010). 'Rock fracture compliance derived from time delays of elastic waves'. In: *Geophysical Prospecting* vol. 58, no. 6, pp. 1111–1122.

Nagata, K., Kilgore, B., Beeler, N. and Nakatani, M. (2014). 'High-frequency imaging of elastic contrast and contact area with implications for naturally observed changes in fault properties'. In: *Journal of Geophysical Research: Solid Earth* vol. 119, no. 7, pp. 5855–5875.

Nara, Y., Meredith, P. G., Yoneda, T. and Kaneko, K. (2011). 'Influence of macro-fractures and micro-fractures on permeability and elastic wave

velocities in basalt at elevated pressure'. In: *Tectonophysics* vol. 503, no. 1-2, pp. 52–59.

Nara, Y., Nakabayashi, R., Yoneda, T., Kaneko, K. and Meredith, P. G. (2012). 'Permeability and elastic wave velocities in sandstone under hydrostatic pressure'. In: *Zairyo/Journal of the Society of Materials Science, Japan* vol. 61, no. 3. [Full Article in Japanese], pp. 214–221.

National Academies of Sciences, Engineering, and Medicine (2020). *Characterization, modeling, monitoring, and remediation of fractured rock*. National Academies Press.

National Research Council (1996). *Rock fractures and fluid flow: contemporary understanding and applications*. National Academies Press.

Neuman, S. P. (2005). 'Trends, prospects and challenges in quantifying flow and transport through fractured rocks'. In: *Hydrogeology Journal* vol. 13, no. 1, pp. 124–147.

Nooraiepour, M., Mondol, N. H., Hellevang, H. and Bjørlykke, K. (2017). 'Experimental mechanical compaction of reconstituted shale and mudstone aggregates: Investigation of petrophysical and acoustic properties of SW Barents Sea cap rock sequences'. In: *Marine and Petroleum Geology* vol. 80, pp. 265–292.

Ogata, K., Senger, K., Braathen, A. and Tveranger, J. (2014). 'Fracture corridors as seal-bypass systems in siliciclastic reservoir-cap rock successions: Field-based insights from the Jurassic Entrada Formation (SE Utah, USA)'. In: *Journal of Structural Geology* vol. 66, pp. 162–187.

Oye, V. et al. (2021). 'Monitoring and imaging of active and passive CO2 seepage patterns'. In: *15th Greenhouse Gas Control Technologies Conference Abu Dhabi*.

Paillet, F. L. et al. (1980). 'Acoustic propagation in the vicinity of fractures which intersect a fluid-filled borehole'. In: *SPWLA 21st Annual Logging Symposium*. Society of Petrophysicists and Well-Log Analysts.

Paillet, F. L. (1983). 'Acoustic characterization of fracture permeability at Chalk River, Ontario'. In: *Canadian Geotechnical Journal* vol. 20, no. 3, pp. 468–476.

Pan, B.-Z., Yuan, M.-X., Fang, C.-H., Liu, W.-B., Guo, Y.-H. and Zhang, L.-H. (2017). 'Experiments on acoustic measurement of fractured rocks and application of acoustic logging data to evaluation of fractures'. In: *Petroleum Science* vol. 14, no. 3, pp. 520–528.

Pyrak-Nolte, L. J. (2019). 'Fracture Specific Stiffness: The critical link between the scaling behavior of hydro-mechanical coupling in fractures and seismic monitoring'. In: *Science of Carbon Storage in Deep Saline Formations*. Elsevier, pp. 311–335.

Pyrak-Nolte, L. J., Myer, L. R. and Cook, N. G. (1990). 'Transmission of seismic waves across single natural fractures'. In: *Journal of Geophysical Research: Solid Earth* vol. 95, no. B6, pp. 8617–8638.

Pyrak-Nolte, L. J., Myer, L. R., Cook, N. G., Witherspoon, P. A. et al. (1987). 'Hydraulic and mechanical properties of natural fractures in low permeability rock'. In: *6th ISRM Congress*. International Society for Rock Mechanics and Rock Engineering.

Pyrak-Nolte, L. J. and Nolte, D. D. (2016). 'Approaching a universal scaling relationship between fracture stiffness and fluid flow'. In: *Nature communications* vol. 7, no. 1, pp. 1–6.

Pyrak-Nolte, L. J., Shao, S. and Abell, B. C. (2017). 'Elastic waves in fractured isotropic and anisotropic media'. In: *Rock Mechanics and Engineering Volume 1: Principles*, p. 323.

Pyrak-Nolte and Morris (2000). 'Single fractures under normal stress: The relation between fracture specific stiffness and fluid flow'. In: *International Journal of Rock Mechanics and Mining Sciences* vol. 37, no. 1-2, pp. 245–262.

RDP Electronics (2021). *How accurate is an LVDT*. URL: https://www.rdpe.com/ex/men-disp.html (visited on 12/02/2021).

Rempe, M., Mitchell, T. M., Renner, J., Smith, S. A. F., Bistacchi, A. and Di Toro, G. (2018). 'The relationship between microfracture damage and the physical properties of fault-related rocks: The Gole Larghe Fault Zone, Italian Southern Alps'. In: *Journal of Geophysical Research: Solid Earth* vol. 123, no. 9, pp. 7661–7687.

Rubino, J. G., Müller, T. M., Milani, M. and Holliger, K. (2014). 'Seismic attenuation and velocity dispersion in fractured rocks: The role played by fracture contact areas'. In: *Geophysical Prospecting* vol. 62, no. 6, pp. 1278–1296.

Sayers, C. M., Taleghani, A. D. and Adachi, J. (2009). 'The effect of mineralization on the ratio of normal to tangential compliance of fractures'. In: *Geophysical Prospecting* vol. 57, no. 3, pp. 439–446.

Schoenberg, M. (1980). 'Elastic wave behavior across linear slip interfaces'. In: *The Journal of the Acoustical Society of America* vol. 68, no. 5, pp. 1516–1521.

Shearer, P. M. (2019). *Introduction to seismology*. Cambridge university press.

Shipton, Z. K., Evans, J. P., Kirschner, D., Kolesar, P. T., Williams, A. P. and Heath, J. (2004). 'Analysis of CO2 leakage through 'low-permeability'faults from natural reservoirs in the Colorado Plateau, east-central Utah'. In: *Geological Society, London, Special Publications* vol. 233, no. 1, pp. 43–58.

Shokouhi, P., Jin, J., Wood, C., Rivière, J., Madara, B., Elsworth, D. and Marone, C. (2019). 'Dynamic stressing of naturally fractured rocks: on the relation between transient changes in permeability and elastic wave velocity'. In: *Geophysical Research Letters* vol. 47, no. 1, e2019GL083557.

Skurtveit, E., Sundal, A., Soldal, M., Sauvin, G. and Bjørnarå, T. (2018). 'CO2 Flow, Alteration And Geomechanical Response In Confining Units–An Experimental Approach'. In: *Fifth CO2 Geological Storage Workshop*. Vol. 2018. 1. European Association of Geoscientists & Engineers, pp. 1–5.

Skurtveit, E., Braathen, A., Larsen, E. B., Sauvin, G., Sundal, A. and Zuchuat, V. (2017). 'Pressure induced deformation and flow using CO2 field analogues, Utah'. In: *Energy Procedia* vol. 114, pp. 3257–3266.

Skurtveit, E., Sundal, A., Bjørnarå, T. I., Soldal, M., Sauvin, G., Zuchuat, V., Midtkandal, I. and Braathen, A. (2020). 'Experimental investigation of natural fracture stiffness and flow properties in a faulted CO2 bypass system (Utah, USA)'. In: *Journal of Geophysical Research: Solid Earth* vol. 125, no. 7, e2019JB018917.

Snow, D. T. (1969). 'Anisotropic permeability of fractured media'. In: *Water resources research* vol. 5, no. 6, pp. 1273–1289.

Sowers, T. and Boyd, O. S. (2019). *Petrologic and mineral physics database for use with the US Geological Survey National Crustal Model*. Tech. rep. US Geological Survey.

Stein, S. and Wysession, M. (2009). *An introduction to seismology, earthquakes, and earth structure*. John Wiley & Sons.

Sun, X., Tang, X., Cheng, C.-H. and Frazer, L. N. (2000). 'P-and S-wave attenuation logs from monopole sonic data'. In: *Geophysics* vol. 65, no. 3, pp. 755–765.

Thomas, T. R. (1998). *Rough surfaces*. World Scientific.

Tran, T. X. (2015). 'Monitoring CO2 behaviour during injection into reservoir sandstone'. Master thesis. University of Oslo.

Tse, R. and Cruden, D. (1979). 'Estimating joint roughness coefficients'. In: *International journal of rock mechanics and mining sciences & geomechanics abstracts*. Vol. 16. 5. Elsevier, pp. 303–307.

Turcotte, D. and Schubert, G. (2014). *Geodynamics*. Cambridge University Press.

Vinciguerra, S., Trovato, C., Meredith, P. G. and Benson, P. M. (2005). 'Relating seismic velocities, thermal cracking and permeability in Mt. Etna and Iceland basalts'. In: *International Journal of Rock Mechanics and Mining Sciences* vol. 42, no. 7-8, pp. 900–910.

Witherspoon, P. A., Wang, J. S., Iwai, K. and Gale, J. E. (1980). 'Validity of cubic law for fluid flow in a deformable rock fracture'. In: *Water resources research* vol. 16, no. 6, pp. 1016–1024.

Wu, C., Harris, J. M., Nihei, K. T. and Nakagawa, S. (2005). 'Two-dimensional finite-difference seismic modeling of an open fluid-filled fracture: Comparison of thin-layer and linear-slip models'. In: *Geophysics* vol. 70, no. 4, T57–T62.

Wu, W., Li, J. and Zhao, J. (2014). 'Role of filling materials in a P-wave interaction with a rock fracture'. In: *Engineering geology* vol. 172, pp. 77–84.

Yang, H., Duan, H. and Zhu, J. (2019). 'Ultrasonic P-wave propagation through water-filled rock joint: an experimental investigation'. In: *Journal of Applied Geophysics* vol. 169, pp. 1–14.

Yang, H., Duan, H.-f. and Zhu, J. (2020). 'Effects of filling fluid type and composition and joint orientation on acoustic wave propagation across individual fluid-filled rock joints'. In: *International Journal of Rock Mechanics and Mining Sciences* vol. 128, p. 104248.

Yin, H. (1993). 'Acoustic velocity and attenuation of rocks: Isotropy, intrinsic anisotropy, and stress-induced anisotropy'. PhD thesis. Stanford University.

Yoshimitsu, N., Furumura, T. and Maeda, T. (2016). 'Geometric effect on a laboratory-scale wavefield inferred from a three-dimensional numerical simulation'. In: *Journal of Applied Geophysics* vol. 132, pp. 184–192.

Yu, H., Zhang, Y., Lebedev, M., Wang, Z., Li, X., Squelch, A., Verrall, M. and Iglauer, S. (2019). 'X-ray micro-computed tomography and ultrasonic velocity analysis of fractured shale as a function of effective stress'. In: *Marine and Petroleum Geology* vol. 110, pp. 472–482.

Zhou, J., Zhang, L., Qi, S. and Yang, D. (2020). 'Empirical ratio of dynamic to static stiffness for propped artificial fractures under variable normal stress'. In: *Engineering Geology* vol. 273, p. 105683.

Zou, Y., Li, J., He, L., Zhao, J. et al. (2016). 'Wave propagation in the vicinities of rock fractures under obliquely incident wave'. In: *Rock Mechanics and Rock Engineering* vol. 49, no. 5, pp. 1789–1802.